

1-1-2017

Herschel Observations Of The Galactic H Ii Region Rcw 79

Hong-Li Liu

Miguel Figueira

Annie Zavagno

L. D. Anderson

Follow this and additional works at: https://researchrepository.wvu.edu/faculty_publications

Digital Commons Citation

Liu, Hong-Li; Figueira, Miguel; Zavagno, Annie; and Anderson, L. D., "Herschel Observations Of The Galactic H Ii Region Rcw 79" (2017). *Faculty Scholarship*. 944.

https://researchrepository.wvu.edu/faculty_publications/944

This Article is brought to you for free and open access by The Research Repository @ WVU. It has been accepted for inclusion in Faculty Scholarship by an authorized administrator of The Research Repository @ WVU. For more information, please contact ian.harmon@mail.wvu.edu.

Herschel^{*} observations of the Galactic H II region RCW 79

Hong-Li Liu^{1,2,3}, Miguel Figueira¹, Annie Zavagno¹, Tracey Hill⁴, Nicola Schneider^{5,6,7}, Alexander Men'shchikov⁸, Delphine Russeil¹, Frédérique Motte^{9,10}, Jérémy Tigé¹, Lise Deharveng¹, L. D. Anderson^{11,12}, Jin-Zeng Li², Yuefang Wu¹³, Jing-Hua Yuan², and Maohai Huang²

¹ Aix Marseille Univ, CNRS, LAM, Laboratoire d'Astrophysique de Marseille, Marseille, France
e-mail: hong-li.liu@lam.fr

² National Astronomical Observatories, Chinese Academy of Sciences, 20A Datun Road, Chaoyang District, 100012, Beijing, China

³ University of Chinese Academy of Sciences, 100049, Beijing, China

⁴ Joint ALMA Observatory, 3107 Alonso de Cordova, Vitacura, Santiago, Chile

⁵ Univ. Bordeaux, LAB, CNRS, UMR 5804, 33270, Floirac, France

⁶ CNRS, LAB, UMR 5804, 33270, Floirac, France

⁷ I. Physik. Institut, University of Cologne, 50937 Cologne, Germany

⁸ Laboratoire AIM ParisSaclay, CEA/DSMCNRS Université Paris Diderot, IRFU, Service d'Astrophysique, Centre d'Etudes de Saclay, Orme des Merisiers, 91191 Gif-sur-Yvette, France

⁹ Institut de Plantologie et d'Astrophysique de Grenoble (IPAG), Univ. Grenoble Alpes/CNRS-INSU, BP 53, 38041 Grenoble Cedex 9, France

¹⁰ Laboratoire AIM ParisSaclay, CEA/IRFU - CNRS/INSU - Université Paris Diderot, Service d'Astrophysique, Bât. 709, CEA-Saclay, 91191, Gif-sur-Yvette Cedex, France

¹¹ Department of Physics and Astronomy, West Virginia University, Morgantown, WV 26506, USA ; Also Adjunct Astronomer at the National Radio Astronomy Observatory, P.O. Box 2, Green Bank, WV 24944, USA

¹² Adjunct Astronomer at the Green Bank Observatory

¹³ Department of Astronomy, Peking University, 100871 Beijing, China

Preprint online version: September 9, 2018

ABSTRACT

Context. Triggered star formation around H II regions could be an important process. The Galactic H II region RCW 79 is a prototypical object for triggered high-mass star formation.

Aims. We aim to obtain a census of the young stellar population observed at the edges of the H II region and to determine the properties of the young sources in order to characterize the star formation processes that take place at the edges of this ionized region.

Methods. We take advantage of *Herschel* data from the surveys HOBYS, “Evolution of Interstellar Dust”, and Hi-Gal to extract compact sources. We use the algorithm *getsources*. We complement the *Herschel* data with archival 2MASS, *Spitzer*, and WISE data to determine the physical parameters of the sources (e.g., envelope mass, dust temperature, and luminosity) by fitting the spectral energy distribution.

Results. We created the dust temperature and column density maps along with the column density probability distribution function (PDF) for the entire RCW 79 region. We obtained a sample of 50 compact sources in this region, 96% of which are situated in the ionization-compressed layer of cold and dense gas that is characterized by the column density PDF with a double-peaked lognormal distribution. The 50 sources have sizes of $\sim 0.1 - 0.4$ pc with a typical value of ~ 0.2 pc, temperatures of $\sim 11 - 26$ K, envelope masses of $\sim 6 - 760 M_{\odot}$, densities of $\sim 0.1 - 44 \times 10^5 \text{ cm}^{-3}$, and luminosities of $\sim 19 - 12712 L_{\odot}$. The sources are classified into 16 class 0, 19 intermediate, and 15 class I objects. Their distribution follows the evolutionary tracks in the diagram of bolometric luminosity versus envelope mass ($L_{\text{bol}} - M_{\text{env}}$) well. A mass threshold of $140 M_{\odot}$, determined from the $L_{\text{bol}} - M_{\text{env}}$ diagram, yields 12 candidate massive dense cores that may form high-mass stars. The core formation efficiency (CFE) for the 8 massive condensations shows an increasing trend of the CFE with density. This suggests that the denser the condensation, the higher the fraction of its mass transformation into dense cores, as previously observed in other high-mass star-forming regions.

Key words. ISM: H II region-stars: formation-stars: massive-ISM: individual objects: RCW 79

1. Introduction

H II regions or bubbles are ubiquitous in the Milky Way. Taking advantage of the *Spitzer*-GLIMPSE (Benjamin

et al. 2003) and MIPS GAL (Carey et al. 2005) surveys, Churchwell et al. (2006, 2007) cataloged the first largest sample of about 600 infrared (IR) dust bubbles in longitudes $|l| \leq 65^{\circ}$. The comparison of these bubbles with the H II region catalog of Paladini et al. (2003) indicates that about 12 – 25% of the bubbles are overlapping with H II regions (Churchwell et al. 2006, 2007). This fraction

* *Herschel* is an ESA space observatory with science instruments provided by European-led Principal Investigator consortia and with important participation from NASA.

is probably a lower limit because the H II region catalog is incomplete, especially for the H II regions with small diameters (Churchwell et al. 2007). Indeed, the fraction can reach $\sim 86\%$ (Deharveng et al. 2010) and even more (Bania et al. 2010; Anderson et al. 2011). These results imply a significant correlation between bubbles and Galactic H II regions. Based on the same surveys, a larger sample of more than 5000 IR bubbles has been visually identified by citizen scientists recruited online (Simpson et al. 2012). Moreover, using data from the all-sky Wide-Field Infrared Survey Explorer (WISE) satellite, Anderson et al. (2014) have made a catalog of over 8000 Galactic H II regions and H II region candidates by searching for their characteristic mid-infrared (MIR) bubble morphology.

It is suggested that triggered star formation might occur around H II regions or bubbles. For instance, Deharveng et al. (2010) studied the association of 102 Churchwell’s bubbles with the dense condensations revealed by the ATLASGAL 870 μm continuum survey data (Schuller et al. 2009). Their study suggested that more than 25% of bubbles may have triggered the formation of high-mass stars. In addition, analyzing the association of Red Mid-course Space Experiment (MSX, Price et al. 2001) massive young stellar objects¹ (MYSOs) with 322 Churchwell’s bubbles, Thompson et al. (2012) suggested that about 14 – 30% of high-mass star formation in the Milky Way might have been triggered by the expanding H II regions or bubbles. Similarly, the study of the association of MYSOs with 1018 bubbles from the Simpson et al. (2012) catalog indicated that around $22 \pm 2\%$ of MYSO formation might have been induced by the expansion of the H II regions or bubbles (Kendrew et al. 2012). These results suggest that triggered star formation around H II regions or bubbles may be an important process, especially for high-mass star formation (e.g., Deharveng et al. 2010; Kendrew et al. 2016).

Triggered star formation may cause the increase of the clump and/or core formation efficiency (CFE), which is analogous to the star formation efficiency (SFE, e.g., Motte et al. 2007; Bontemps et al. 2010b; Eden et al. 2012). For example, in the W3 giant molecular cloud, which is a Galactic high-mass star-forming region, Moore et al. (2007) found that the CFE is around 5 – 13% in the undisturbed cloud, but about 25 – 37% in the feedback-affected region, which is indicative of an increase in CFE. Furthermore, Eden et al. (2012) reported a local increase in CFE in the W43 H II region, which may be associated with the triggering of star formation in its vicinity (Bally et al. 2010). In addition, the increases in CFE have been predicted by the simulation of Dale et al. (2007). Their simulation with feedback from an H II region results in an SFE approximately one-third higher than in the control run without feedback.

In spite of its importance, triggered star formation remains difficult to be clearly identified (e.g., Elmegreen 2011; Dale et al. 2013; Liu et al. 2015; Dale et al. 2015). It is difficult to distinguish stars formed by triggering from those forming spontaneously (Elmegreen 2011; Dale et al. 2015). The high surface density of YSOs observed at the edge of H II regions or bubbles is often assumed to be a result of triggered star formation (Zavagno et al. 2006; Deharveng

et al. 2009; Thompson et al. 2012; Kendrew et al. 2012; Liu et al. 2015, 2016; Yadav et al. 2016; Nandakumar et al. 2016). However, these YSOs might either be redistributed by the expansion of H II regions or bubbles, or they might form in situ (Elmegreen 2011; Liu et al. 2015; Dale et al. 2015). Moreover, the incompleteness of YSOs, especially for the youngest protostars that are deeply embedded in dense clouds, prevents us from restoring their true spatial distribution (Liu et al. 2015). These facts make it difficult to draw a convincing conclusion on triggered star formation around ionized regions.

Herschel observations (Pilbratt et al. 2010), with their unprecedented angular resolutions and sensitivities in the far-IR regime, allow us to study the young stellar population in detail and to assess the importance of triggered star formation. The large wavelength coverage of *Herschel* (70–500 μm) and the high sensitivity allow the detection of highly embedded YSOs (e.g., class 0 objects) that cannot be detected at shorter wavelengths because of their low luminosity and high extinction (Zavagno et al. 2010). Therefore, *Herschel* observations allow us to obtain a census of the YSO population in all evolutionary stages around ionized region for a better study of the impact of high-mass stars on their surrounding. Indeed, more class 0 candidates have been detected with *Herschel* observations in different star-forming regions (e.g., Motte et al. 2010; Zavagno et al. 2010; Hennemann et al. 2010; Deharveng et al. 2012; Giannini et al. 2012; Samal et al. 2014; Deharveng et al. 2015). Furthermore, the spectral energy distribution (SED) of YSOs can be better constrained by the large FIR wavelength coverage, leading to more accurate estimates of their physical parameters such as the envelope mass, dust temperature, and bolometric luminosity. The luminosity-mass diagram is a useful tool to infer the evolutionary properties of the YSOs (Molinari et al. 2008, 2016). Moreover, *Herschel* images allow us to obtain reliable catalogs of compact sources (core/clumps, Figueira et al. (2016), and Tigé et al. 2016, submitted). This allows us to estimate the CFEs on smaller scales toward H II regions. This is crucial for studying the influence of ionized regions on local star formation.

RCW 79 is a textbook example of an H II region where triggered star formation might have taken place (Zavagno et al. 2006, hereafter ZA06). In this paper, we analyze the star formation observed around this region, using *Herschel* data from the surveys HOBYS² (Motte et al. 2010) and “Evolution of Interstellar Dust” (Abergel et al. 2010), complemented with 2MASS, *Spitzer*, and WISE data. Our purposes are to search for clumps that may form high-mass stars, to explore the star formation evolutionary scenarios, and to investigate the CFEs in RCW 79. This paper is organized as follows: we present RCW 79 in Sect. 2, the *Herschel* observations together with other archival data sets are described in Sect. 3, the results are presented in Sect. 4, and the discussion is given in Sect. 5, followed by our conclusions in Sect. 6.

¹ A massive young stellar object (MYSO) is an embedded infrared source that is luminous enough to be a young O- or B-type star, but has not yet formed an H II region (e.g., Urquhart et al. 2007; Mottram et al. 2007)

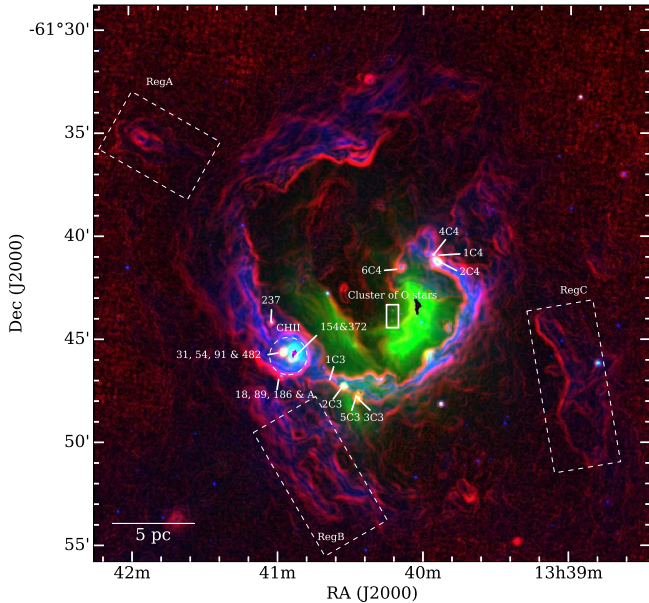


Fig. 1: Three-color image of RCW 79: *Spitzer* GLIMPSE 8 μm image (blue), *Spitzer* MIPS GAL 24 μm image (green), and *Herschel* 70 μm image (red). The black knot seen at 24 μm in the direction of the H II region is a result of saturation. The 70 μm image is unsharped to better emphasize the YSOs associated with the region. Nineteen YSOs are pinpointed with the identity number given by ZA06. The compact H II region (CH II) is delineated with the dashed circle. The full box locates the exciting stars composed of a cluster of O stars (Martins et al. 2010). The dashed boxes mark the other three regions (RegA, RegB, and RegC) associated with RCW 79. North is up and east is left.

2. Presentation of RCW 79

RCW 79 (Rodgers et al. 1960) is a bright optical H II region ionized by a cluster of a dozen O stars, the two most massive of which have a spectral type O4-6V/III (Martins et al. 2010). The ionizing luminosity of the ionizing stars was estimated to be 10^3 times higher than the mechanical luminosity of their stellar winds (Martins et al. 2010), indicating a radiation-driven H II region. This region is spatially encompassed by an almost complete dust ring (see Fig. 1), with a diameter of $\sim 12'$, which corresponds to 12.8 pc at a distance of 4.3 kpc (ZA06). The ring structure was revealed with a velocity range of -50 to -44 km s^{-1} in the observations of ^{12}CO , ^{13}CO , and C^{18}O ($J=1-0$) (Saito et al. 2001). It is in good agreement with the velocity range of -51 to -40 km s^{-1} measured for ionized gas (ZA06), indicative of a good association of the dust ring with the H II region.

Figure 1 shows the composite three-color image of RCW 79 where blue, green, and red code the *Spitzer* 8.0 and 24 μm and the *Herschel* 70 μm , respectively. An unsharp masking³ was applied to the 70 μm image to filter out diffuse emission and enhance the contrast of intense emis-

sion in the images. As shown in Fig. 1, the dust ring is seen at both 8.0 and 70 μm . Emission at 8.0 μm mainly comes from polycyclic aromatic hydrocarbons (PAHs) at 7.7 and 8.6 μm , indicative of photoionization regions (PDRs, e.g., Pavlyuchenkov et al. 2013) which indicate the interplay between ionized gas and the adjacent neutral cloud. The 70 μm emission mainly traces hot components such as very small grains (VSGs) or warm material heated by protostars. Therefore, the appearance of the dust ring at both 8.0 and 70 μm demonstrates that the enclosed H II region is interacting with and heating its vicinity. The 24 μm emission is predominantly distributed in the direction of the H II region. This spatial distribution is in good agreement with the fact that 24 μm emission mainly arises from hot dust, which can reach rather high temperatures after absorbing high-energy photons (e.g. Deharveng et al. 2010; Liu et al. 2016).

SEST-SIMBA 1.2 mm continuum observations with an angular resolution of $24''$ revealed three highest mass fragments in the dust ring (see ZA06). For this, ESO-NTT SOFI near-IR and *Spitzer* GLIMPSE mid-IR data were combined to study the young stellar population observed toward this region. Nineteen class I YSO candidates (see Fig. 1) were found to be associated with the three fragments. In addition, one compact H II region (CH II) is embedded in the most massive fragment in the southeast region of the ring. Martins et al. (2010) furthermore observed 8 out of the 19 YSOs with the near-IR integral field spectrograph SINFONI mounted on the VLT telescope. All present spectral features typical of YSOs. All lines have velocities similar to that of the ionized gas, confirming the association of these YSOs with the region. The dust ring is opened in the northwest. The $\text{H}\alpha$ velocity field of ionized gas shows a flow through the hole with a few km s^{-1} (see Fig. 12 of ZA06). This flow was interpreted as a champagne phenomenon, indicating a strong interaction of RCW 79 with its surrounding material (ZA06). Moreover, combining the model of Whitworth et al. (1994), ZA06 found that the ring of collected gas had enough time to fragment during the lifetime of RCW 79, and that the radius and mass of the fragments basically agree with the values predicted by the model. Therefore, ZA06 concluded that the YSOs at the edge of RCW 79 might have been triggered by the expanding H II region.

An elongated clump (i.e., RegA) is located about 6 pc away from the northeast edge of RCW 79 (see Fig. 1). This clump is associated with 8 μm emission, suggesting influences from ionized gas. The northeastern ring orthogonal to the clump appears diffuse relative to its neighbors. This diffuse characteristic implies that the clump could be photoionization-shaped by the leaking photons from the H II region through the diffuse ring, as shown in Fig. 2(c). Additionally, there are two other extended filamentary features (e.g., RegB and RegC) situated to the south and southwest of RCW 79, respectively. Based on the observations of ^{12}CO , and ^{13}CO ($J=1-0$) (Saito et al. 2001), these two features have the same velocity as RCW 79, which means that they may be associated. As shown in Fig. 1, these two features are associated with PDRs, as seen in 8 μm emission. Likewise, the two features could be a consequence of photoionization by the leaking photons from RCW 79, as discussed in Sect. 4.1.

² The *Herschel* imaging survey of OB Young Stellar objects (HOBYS) is a *Herschel* key programme. See <http://hobys-herschel.cea.fr>

³ The module *scipy.ndimage* for multidimensional gradient magnitude using Gaussian derivatives is available at <http://docs.scipy.org/doc/scipy/reference/py-modindex.html>.

Table 1: *Herschel* observational parameters

Instrument	Size arcmin	Time s	ObsIDs	Date yyyy-mm-dd
PACS	30 × 30	2768	1342188880, 1342188881	2010-01-03
SPIRE	30 × 30	837	1342192054	2010-03-10

3. Observations and data reduction

3.1. *Herschel* observations

RCW 79 was observed as part of the HOBYS (Motte et al. 2010) and “Evolution of Interstellar Dust” (Abergel et al. 2010) guaranteed time key programs. The Photodetector Array Camera & Spectrometer (PACS, Poglitsch et al. 2010) at 100 and 160 μm and the Spectral and Photometric Imaging Receiver (SPIRE, Griffin et al. 2010) at 250, 350, and 500 μm were equipped to carry out both surveys with scan speeds of 20'' per second for PACS and 30'' per second for SPIRE. The angular resolutions of these five bands in order of increasing wavelength are 6''7, 11''4, 18''2, 25'', and 36''. Table 1 lists the observation parameters including the mapping size, the total integration time, the observation identification number, and the observation date.

The *Herschel* data were processed using slightly modified versions of the default PACS and SPIRE pipelines built into the *Herschel* interactive processing environment (HIPE) software v. 10. The pipelines produced level 2 data, which to some extent suffer from striping artifacts in the in-scan directions and flux decrements around bright zones of emission resulting from the median-filtering baseline removal. To remove both artifacts, the *Scanamorphos* software (Roussel 2012), version 9, was used to create the final level 2 maps without the “Galactic” option. Additionally, the astrometry of all the maps was adjusted to be consistent with each other and with higher resolution *Spitzer* data.

The 70 μm image from the Hi-Gal survey (Molinari et al. 2010) was also retrieved to complement our observations. Its measured angular resolution is 10''7 (Traficante et al. 2011). The detailed descriptions of the preprocessing of the data up to usable high-quality image can be found in Traficante et al. (2011).

The absolute calibration uncertainty for PACS is estimated to be 10% at 70 and 100 μm and 20% at 160 μm (see PACS observers’ manual⁴), while for SPIRE it is within 10% for all bands (see SPIRE observers’ manual⁵).

3.2. Archival data

To carry out a multiwavelength analysis of this region, ancillary infrared data were taken from the IRSA Archive.⁶ The *J*, *H*, *Ks* images at 1.25, 1.65, and 2.17 μm with a resolution of 4'' were retrieved from the Two Micron All Sky Survey (2MASS, Skrutskie et al. 2006). In addition, the images of the *Spitzer* Infrared Array Camera (IRAC) at 3.6, 4.5, 5.8, and 8.0 μm , together with the Multiband imaging photometer for *Spitzer* (MIPS) at 24 μm , were obtained from the GLIMPSE (Benjamin et al. 2003) and MIPS GAL

(Carey et al. 2005) surveys, respectively. The resolutions in the IRAC bands are better than 2'', and the resolution is 6'' in the MIPS 24 μm band. Moreover, the 12 μm image with a resolution of 6''5 was used from the WISE survey (Wright et al. 2010). This survey provides the images in four wavelength bands, but the 3.4 and 4.6 μm bands were not taken into account because their resolutions are lower than those of the IRAC 3.6 and 4.5 μm bands. We did not make use of the 22 μm data either because negative values appear in the majority of pixels of the image covering RCW 79.

4. Results

4.1. Dust temperature and column density maps

The dust temperature (T_{dust}) and column density (N_{H_2}) maps of RCW 79 were created using a modified blackbody model to fit the SEDs pixel by pixel, as described by Hill et al. (2012a,b). Before the SED fitting, all *Herschel* images except for the 70 μm image were convolved to the resolution of the 500 μm band and then regridded to the same pixel size as that of the 500 μm image. Emission at 70 μm was excluded in the SED fitting because it can be contaminated by emission from small grains in hot PDRs. In the SED fitting, a dust opacity law of $\kappa_{\nu} = 0.1 \times (\nu/1\text{THz})^{\beta}$ was adopted with a gas-to-dust mass ratio of 100 (Beckwith et al. 1990). $\beta = 2$ was fixed to be consistent with other papers of the HOBYS consortium. Additionally, to reveal more small structures, a high-resolution (18''2) column density map was made based on the method of Hill et al. (2012a). The 36'' resolution T_{dust} and 18''2 resolution N_{H_2} maps are presented in Fig. 2.

In Fig. 2 (a) the dust temperature distribution on the large scale almost agrees with the 24 μm emission. As mentioned in Sect. 2, this 24 μm emission traces hot dust heated by high-energy ionizing photons, which can be demonstrated by the good spatial coincidence of 24 μm emission with ionized gas seen by the H α emission (see Fig. 2 (c)). On the small scale, we see the four main hottest regions (HRs 1-4) with a range of 23.5 to 27 K (see Fig. 2 a-b). The first two (HR1 and HR2) are located in the direction of the H II region, spatially overlapping with dense ionized gas (see Fig. 2 (c)). The other two (HR3 and HR4) are located on the southwestern and southeastern edges of RCW 79, respectively, where they are exposed to ionized gas. These four hottest regions could in large part be a consequence of their exposure to the heating of ionized gas. Additionally, the hottest of the four regions (HR3) is situated on the southeastern edge (see Fig. 2 a-b), but it is the farthest from the cluster of ionizing stars of RCW 79. Given the association of this region with the CH II region, the highest temperature can be attributed to an additional heating from the CH II region. In contrast, there are five cold regions (CRs 1-5) with lower temperatures ($\sim 17.5 - 20$ K, see Fig. 2 (a-b)). These five coldest regions are all spatially coincident with the column density peaks. The first two regions (CR1 and CR2) lie on the southern edge, the third region (CR3) lies on the western edge, and the remaining two regions (CR4 and CR5) lie in the northern area of RCW 79. For these regions, the anticorrelation between their temperatures and column densities suggests that their low temperatures could arise, in part, from a lower penetration of the external heating from the H II region into dense regions (Liu et al. 2016).

⁴ http://herschel.esac.esa.int/Docs/PACS/pdf/pacs_om.pdf

⁵ http://herschel.esac.esa.int/Docs/SPIRE/spire_handbook.pdf

⁶ <http://irsa.ipac.caltech.edu/frontpage/>

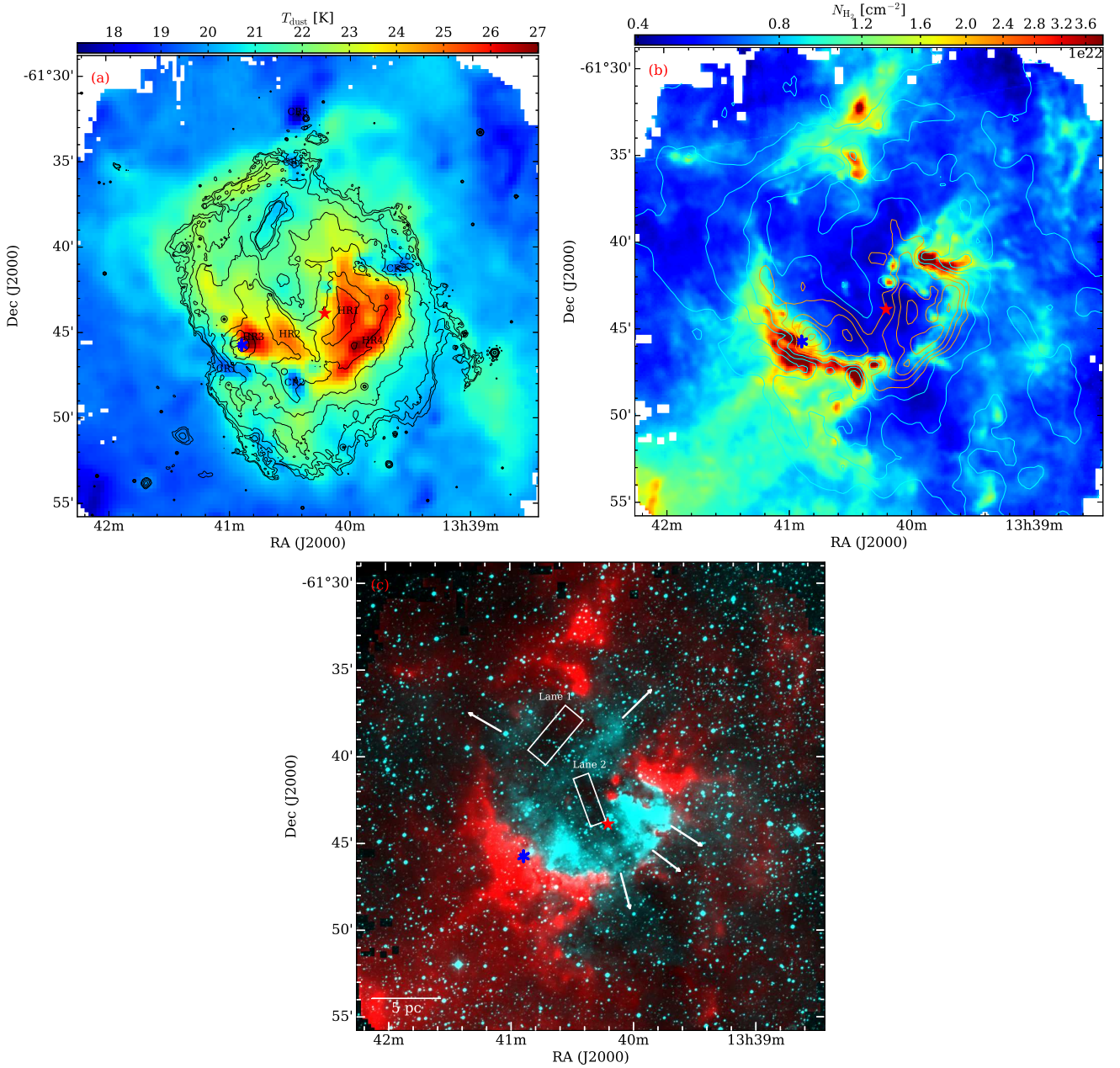


Fig. 2: (a) $36''$ resolution dust temperature map (color scale) overlaid with *Spitzer*-MIPSGAL $24\mu\text{m}$ emission (black contours). The contour levels are 40, 44, 55, 84, 163, 374, 940, and 2459 MJy sr^{-1} . HRs 1-4 show the four hottest regions and CRs 1-5 the five coldest regions in RCW 79. (b) $18.2''$ resolution column density map with dust temperature contours. The cyan and orange temperature contours start from 20, and 23 K, respectively, with a step of 1 K. (c): two-color composite image consisting of the $18.2''$ resolution column density map (in red) and the SuperCOSMOS $\text{H}\alpha$ image (in turquoise). Arrows denote directions of leaking ionizing photons and rectangles outline dark $\text{H}\alpha$ emission. A scale bar of 5 pc is shown on the bottom left. In all panels, the star and asterisk symbolize the center position of a cluster of exciting stars for the classical and compact H II regions, respectively.

Figure 2(c) shows the column density map (red) superimposed on $\text{H}\alpha$ emission (turquoise) from the SuperCOSMOS survey (Parker & Phillipps 1998). The shell seen in the column density distribution encompasses ionized gas traced by $\text{H}\alpha$ emission, suggesting the strong impact that the enclosed H II region has on its surroundings. The influence on the column density structure is discussed in more detail in Sect. 4.2. Of interest are two dark lanes of $\text{H}\alpha$ emission in the direction of the H II region. Such characteristics have also been observed in RCW 120 (Anderson et al.

2015). The dark lanes of $\text{H}\alpha$ emission have been attributed to optical absorption by foreground material. As shown in Fig. 2(c), lane 1 is indeed associated with column density enhancement with respect to its surrounding. Therefore, the dark lane 1 of ionized gas could be a result of optical absorption by foreground material. In contrast, lane 2 is not clearly related with enhanced column densities, indicating that lane 2 of ionized gas may not be caused predominantly by optical absorption of foreground clouds. In fact, lane 2 of the ionized gas is spatially well coincident with the central

cavity, as inscribed at $24\ \mu\text{m}$ in Fig. 2 (a). On the basis of hydrodynamical simulations, it is suggested that a young H II region should not be strongly affected by stellar winds at the beginning of its evolution, but the winds eventually become stronger, giving rise to a very hot dust cavity (Capriotti & Kozminski 2001; Freyer et al. 2003, 2006). Such a cavity is probably shown in the $24\ \mu\text{m}$ emission tracing hot dust (Watson et al. 2008; Liu et al. 2015). However, the dust cavity could also be caused by either the radiation pressure of ionizing stars or dust destruction by their intense radiation (Inoue 2002; Krumholz & Matzner 2009; Martins et al. 2010). In lane 2, ionized gas dark emission indicates no intense radiation in this cavity. Additionally, Martins et al. (2010) concluded that the effect of the stellar winds on the dynamics of RCW 79 is rather limited. Therefore, we suggest that lane 2 may arise from the dispersion of ionized gas by the strong radiation pressure from the cluster of ionizing stars. Diffuse ionized gas emission is observed outside the ionized region, indicated by arrows in Fig. 2 (c). These emissions can be due to the leaking of ionizing photons through density holes in the PDR, as has been suggested in Zavagno et al. (2007) (see their Fig. 2).

4.2. Probability distribution function

The impact of different physical processes (e.g., turbulence, gravity, or pressure) on the column density structure of a whole molecular cloud or parts of it can be studied using probability distribution functions (PDFs) of the column density. PDFs are frequently used in observations and theory (e.g., Kainulainen et al. 2009; Schneider et al. 2015b; Federrath & Klessen 2012, for an overview). Using *Herschel* dust maps, various studies showed that a lognormal shape of the PDF is consistent with low-density gas, dominated by turbulence (Schneider et al. 2013), and a single or double power-law tail appears for dense star-forming clouds (e.g., Hill et al. 2011; Russeil et al. 2013; Schneider et al. 2015a; Könyves et al. 2015), which is attributed to the effects of gravity (e.g., Girichidis et al. 2014, for an overview). Molecular clouds surrounding H II regions (Schneider et al. 2012; Tremblin et al. 2014b) showed PDFs with two lognormal distributions (“double-peak” PDFs) or PDFs with a larger width, followed by a power-law tail. These observations were interpreted as an expansion of the ionized gas into the turbulent molecular cloud (representing the first lognormal form of the PDF), leading to a compression zone with higher densities that in turn cause the second peak, but are still dominated by turbulence. The widths of the two lognormal distributions of the PDFs and the distance between the peaks depend on the relative importance of ionization pressure and turbulent ram pressure (Tremblin et al. 2014b).

For this paper, we constructed a PDF⁷ of RCW 79 from the whole area observed with *Herschel*, using the high- and low-angular resolution maps ($18''.2$ and $36''$, respectively). The PDFs do not differ much (see Schneider et al. 2015b; Ossenkopf-Okada et al. 2016, for resolution effects on PDFs), therefore we only present the PDF of the high-resolution map here. We did not perform a background sub-

traction, as recommended by Schneider et al. (2015b), because the map of RCW 79 is too small to clearly define a background level. The column density at the map borders is on the order of a few A_v , but may still contain parts of the associated molecular cloud.

Figure 3 (left) shows the column density map and the corresponding PDF (right). The PDF has a complex structure, and the best results (we performed KS-tests for which we fit different distributions) were obtained with two lognormal distributions in the lower column density range and one power-law tail for higher column densities. The widths of the lognormal forms are $\sigma=0.18$ for both, and the peaks are around $A_v = 7$ and $A_v = 11$. Starting at $A_v = 20$, the distribution is better described by a power-law tail with a slope of $s=-2.46$, which corresponds to $\alpha=1.8$ for a spherical density distribution with $\rho \propto r^{-\alpha}$. Our interpretation of these results is that the first lognormal form shows the turbulent gas of the associated molecular cloud (in dark blue scale in the column density map), followed by the compressed shell component (indicated by the gas component between the light blue and black contours in Fig. 3). This turbulent gas layer starts to fragment, and gravity takes over in the densest parts of the compressed shell, forming clumps and finally cores. The gravitational collapse of the embedded cores then leads to the power-law tail. The exponent $\alpha=1.8$ assuming a spherical density distribution is consistent with the exponent $\alpha=1.5-2$ predicted from theory (Shu 1977; Whitworth & Summers 1985). These results are fully consistent with what is found in Tremblin et al. (2014b) for RCW 120, which is also an H II region bubble. The only difference is that the peaks of the two lognormal distributions of the unperturbed lower density gas and the compressed shell are closer together, implying that the density contrast in RCW 79 is lower. The second lognormal form indicates the compression from ionized gas that might have created the necessary condition for triggered star formation in RCW 79.

4.3. Compact sources

4.3.1. Source extraction

The algorithm *getsources* (Men’shchikov et al. 2010, 2012; Men’shchikov 2013) was used to extract compact sources from the images at all *Herschel* wavelengths from 70 to $500\ \mu\text{m}$. Full details on the source extraction can be found in Appendix A.1. The resulting catalog returned by *getsources* contains the identity number of sources, unique coordinates, peak and integrated fluxes with respective errors, and FWHM major and minor sizes with a position angle at each wavelength, as presented in Table B.1. In our work, 317 sources were initially extracted as candidate compact sources ($\text{Sig}_{\text{mono}} \geq 7$)⁸ within a region of $25' \times 25'$ centered at $\alpha_{2000} = 13^{\text{h}}40^{\text{m}}20^{\text{s}}.928$, $\delta_{2000} = -61^{\circ}42'20''.16$.

To pick out the most reliable compact sources, two selection criteria were applied to the 317 sources:

1. A minimum of three measured integrated fluxes with good qualities for a better constraint on the SED fitting in Sect. 4.3.2. They must include the flux at a reference wavelength (160 or $250\ \mu\text{m}$, see Sect. A.2). The signal-to-

⁷ To be consistent with other *Herschel* studies, we used the visual extinction A_v instead of the hydrogen column density, linked by $N_{\text{H}_2} = A_v \times 0.94 \times 10^{21}\ \text{cm}^{-2}\ \text{mag}^{-1}$ (Bohlin et al. 1978).

⁸ Sig_{mono} is the detection significance given by *getsources*. A source with $\text{Sig}_{\text{mono}} \geq 7$ is regarded as reliable (Men’shchikov et al. 2012).

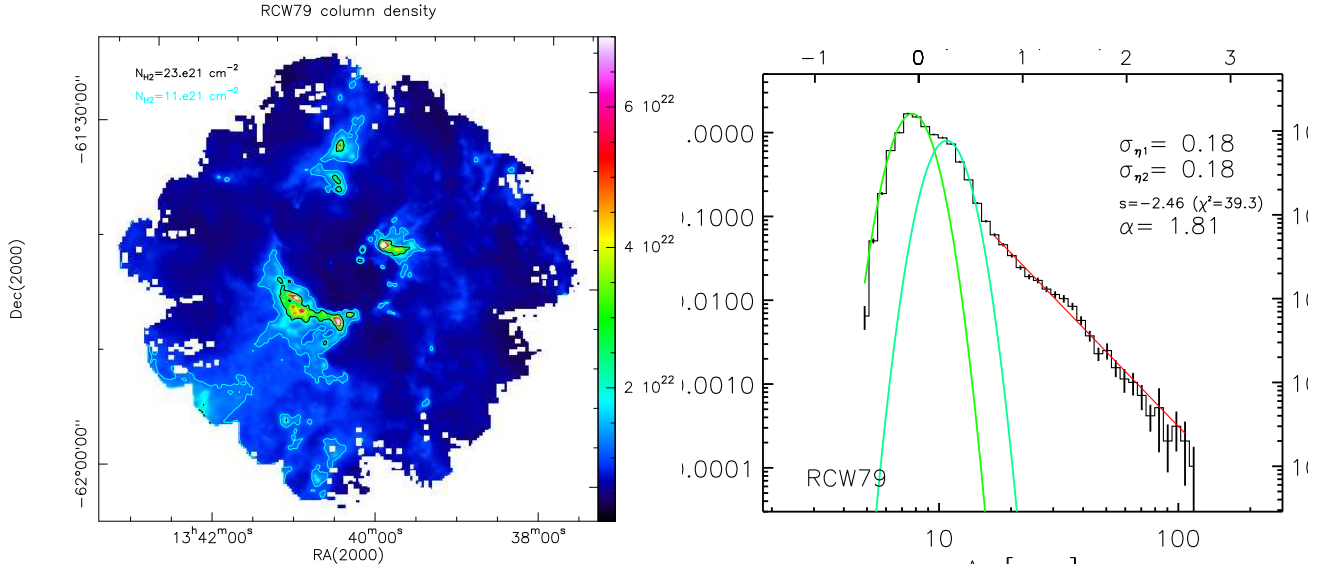


Fig. 3: **Left:** High-angular ($18''$) resolution column density of RCW 79. The contour levels characterize the gas in the compressed layer (above $A_V \sim 10$) and the gravitationally dominated gas (above $A_V \sim 20$). **Right:** PDF of the column density map. The distribution is characterized by two lognormals (dark and light green) with similar widths of $\sigma=0.18$, and a power-law tail with a least-squares fit in red. The slope s of the power-law tail is -2.46 .

noise (S/N) ratios of the integrated and corresponding peak fluxes at each wavelength have to be greater than 2 to guarantee the good qualities of the flux measurements.

2. An axis ratio of < 2 and a deconvolved size (see Eq. A.3) of < 0.4 pc for preliminarily selected compact sources. The latter is arbitrarily determined and is based on the fact that most of sources in the catalog have sizes of < 0.4 pc. Objects that do not fulfill the above criteria may be cloud fragments or filament pieces.

Applying these criteria, we end up with a sample of 100 candidate compact sources.

4.3.2. Graybody SED fitting

Assuming optically thin dust emission, we adopted a single-temperature graybody function to fit the SED of sources between 100 and $500 \mu\text{m}$ (see Appendix A.2). The SED fitting was performed for the 100 candidate compact sources to derive their physical parameters including the dust temperature T_d and envelope mass M_{env} . As mentioned in Sect 4.1, $70 \mu\text{m}$ emission was not included in the SED fitting. Before the SED fitting, we scaled fluxes to the same aperture at the reference wavelength (see Sect. A.2) and made the corresponding color corrections. Detailed descriptions of the flux scaling and color correction methods can be found in Appendix A.2. In the SED fitting, the dust emissivity spectral index, β , was set at 2 and was not left as a free parameter. This is the value adopted for the analysis of the HOBYS survey. Moreover, Men'shchikov (2016) suggested that variable β during the SED fitting for mass derivation leads to huge biases and should never be used (Men'shchikov 2016). We must keep in mind that absolute values in masses are at least a factor of 2–3 (Men'shchikov 2016). After the SED fitting, we kept 89 sources selected by the goodness of their fit ($\chi^2/N_{\text{data}} < 10$).

4.3.3. Infrared counterparts

We searched for the possible IR features of the 89 sources in the 1.25 to $70 \mu\text{m}$ range, including point-like objects, absorption against local bright background emission, and filament- or extended-structure emission. A point-like object, with a size of $< 10''$ depending on the resolution of the IR data (see Sect. 3), may be an indicator of ongoing star formation, absorption is indicative of cold gas lying in front of the hot dust, and the IR filament or extended-structure implies an accumulation of either hot dust or PDRs in which there may be embedded point-like objects that are not easily separated from bright background emission.

Taking advantage of *Herschel* images complemented with the $18''$ resolution column density map and other IR data, we made a plot consisting of $16 \times 1.5 \times 1.5$ images for each source (see Fig. B.1) to pinpoint the IR counterparts. The IR sources were searched for within $5''$, which corresponds to 0.1 pc at the distance of RCW 79.

Following the appearance of their infrared emission, we classified the sources into three groups:

1. *Group 0* compact sources with IR absorption or without any detectable IR counterparts,
2. *Group IM* (i.e., intermediate) compact sources with filament or extended-structure IR emission,
3. *Group I* compact sources with point-like IR counterparts.

By visually inspecting the plots in Fig. B.1, we identified 14 *Group 0* and 11 *Group I* sources. The remaining 64 out of 89 sources are found to be only spatially coincident with filament (or extended) emission. These sources can be either compact sources or pieces of clouds. To distinguish the compact sources from the pieces of clouds, we requested that the compact sources have at least three good flux measurements at wavelengths $\geq 100 \mu\text{m}$. The good photometry at each wavelength is defined by the photometry ellipse centered on the corresponding density peak. For example, the photometry ellipses of source 1 at wavelengths 100 to $500 \mu\text{m}$

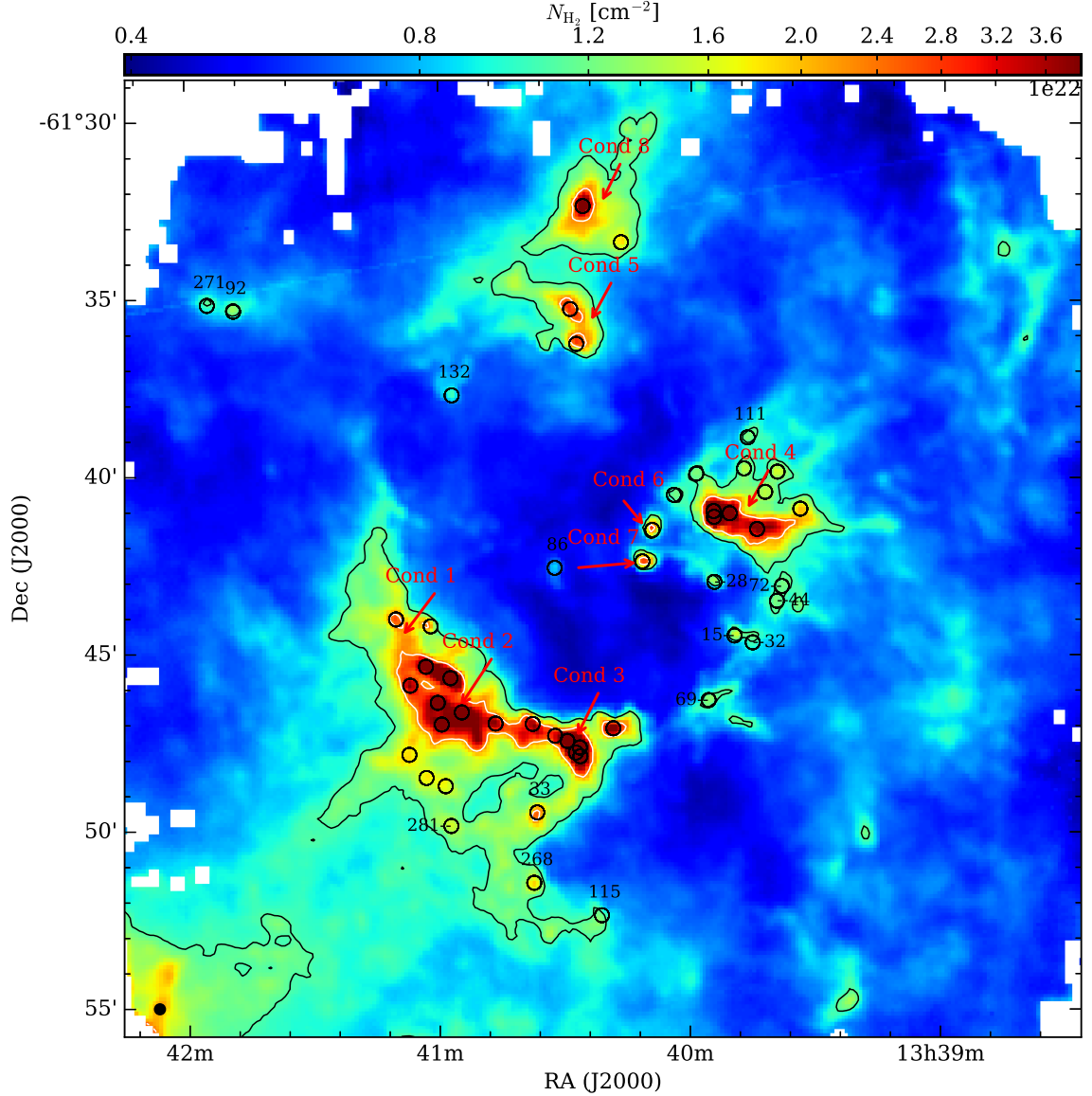


Fig. 4: Distribution of 50 compact sources overlaid on the high-resolution ($18''.2$) column density map. The black and white contours delineate the gas in the compressed layer (above $N_{\text{H}_2} = 11 \times 10^{21} \text{ cm}^{-2}$ marked with the black contour) and the gravitationally dominated gas (above $N_{\text{H}_2} = 23 \times 10^{21} \text{ cm}^{-2}$ marked with the white contour, see Sect. 4.2), respectively. The arrows pinpoint the eight condensations as named by ZA06. A beam size of $18''.2$ is shown with the black full circle on the bottom left.

are centered on the respective density peaks (see Fig. B.1). As a result, we picked out 25 *Group IM* sources. In all, we obtained 14 *Group 0*, 25 *Group IM*, and 11 *Group I* compact sources. The physical parameters of these 50 compact sources are summarized in Cols. 1-6 of Table 2, including the ID, the coordinates (*R.A.* and *Dec.*), the deconvolved size (D_{dec}), the dust temperature (T_{d}), the envelope mass (M_{env}), and the number density (n_{H_2}). The errors of T_{d} and M_{env} , given by the MPFITFUN⁹ procedure, mainly arise from the photometric flux error at each wavelength (see Table B.2). The 50 compact sources have sizes ranging from 0.1 to 0.4 pc with an average value of 0.2 pc, temperatures ranging from 11 to 26 K, envelope masses ranging

from 6 to $760 M_{\odot}$, and number density ranging from 0.1 to $44 \times 10^5 \text{ cm}^{-3}$. In the following, we should keep in mind that due to their large typical size of 0.2 pc, these compact sources may be made of different sources in different evolutionary stages.

Figure 4 displays the spatial distribution of the 50 compact sources overlaid on the high-resolution column density map. They are predominantly concentrated on the local density peaks, which has also been observed in other star-forming regions like the Rosette molecular cloud (Schneider et al. 2012). Interestingly, 96% of the sources are observed toward the compressed layer (within the black contour in Fig. 4, see Sect. 4.2). This distribution not only indicates that these compact sources are exposed to the influence of the H II region, but it is also suggestive of more efficient formation of compact sources in the layer of compressed gas

⁹ <http://cow.physics.wisc.edu/~craigm/idl/mpfittut.html>

than in other regions away from the H II region. Moreover, 26 out of 50 compact sources are found to be associated with the gravitationally bound gas (within the white contour). Coupled with their associated IR counterparts, the 26 compact sources have a high probability of forming stars through gravitational collapse.

4.3.4. Luminosity

The bolometric luminosities L_{bol} for the 50 compact sources are calculated as

$$L_{\text{bol}} = 4\pi D^2 \int F_\nu d\nu. \quad (1)$$

The bolometric luminosity of the 39 *Group 0* and *Group IM* sources that have no IR point-like objects was obtained by integrating the graybody SED fits over frequencies. For the 11 *Group I* sources, IR fluxes were added to the calculation. To obtain the IR fluxes, we cross matched these 11 sources with those in the archival GLIMPSE I (Benjamin et al. 2003), MIPS GAL (Gutermuth & Heyer 2015), and ALLWISE (Wright et al. 2010) catalogs within a search radius of $5''$. These catalogs all have been cross matched with the 2MASS survey. Therefore, if there is any, the near IR fluxes can be simultaneously retrieved. All *Group I* sources except for source 28 can be well matched in the catalogs. For source 28 we used the software DS9 to perform aperture photometries at the wavelengths where the IR counterpart exists. Table B.4 gives a summary of the resulting IR fluxes for the 11 compact sources. In addition, the submillimeter luminosities ($L_{\text{submm}}^{\lambda > 350}$) for all 50 compact sources were derived from the integrated luminosity of the resulting SED fit over wavelengths $\geq 350 \mu\text{m}$. The derived L_{bol} and $L_{\text{submm}}^{\lambda > 350}$ are given in Table 2. An uncertainty of 10% for both L_{bol} and $L_{\text{submm}}^{\lambda > 350}$ is estimated from the flux errors. The bolometric luminosities of the 50 compact sources range from 19 to $12712 L_\odot$.

4.4. Condensations in RCW 79

Figure 4 shows several cold, dense, and gravitationally bound regions marked in the white contour that were detected in the SEST 1.2 mm observations (see Fig. 3 of ZA06) and called condensations. They are also revealed in the APEX 870 μm and APEX+Planck¹⁰ maps (see Fig. 5 (a)–(b)). To better define these condensations in our data, we take advantage of the APEX+Planck map because of its recovery of diffuse gas emission on large angular scales (Csengeri et al. 2016). This recovery is rather obvious in RCW 79 (see Fig. 5 (a)–(b)). In the map, eight condensations are separated with the ellipses that roughly contain the majority of the fluxes within a contour level of 0.4 Jy beam^{-1} ($\sigma = 0.05 - 0.07 \text{ Jy beam}^{-1}$).

Four groups of mass estimates were calculated for each of the eight condensations, using the APEX 870 μm , APEX+Planck, SEST 1.2 mm fluxes, and the high-resolution column density map. First of all, the total fluxes

$F_{870\mu\text{m}}$ and $F_{870\mu\text{m}}^{\text{Planck}}$ were integrated over the ellipse of each condensation from the APEX 870 μm and APEX+Planck maps, respectively. The integrated 1.2 mm flux $F_{1.2\text{mm}}$ was retrieved from Table 2 of ZA06. With the measured fluxes, the respective mass $M_{870\mu\text{m}}$, $M_{870\mu\text{m}}^{\text{Planck}}$, and $M_{1.2\text{mm}}$ can be calculated according to Eq. A.1 with the same dust opacity law as the one adopted in Sect. 4.1. In the calculations, the average temperature ($\overline{T_d}$) over each condensation from the dust temperature map was taken into account. It is noteworthy that we recalculated the mass $M_{1.2\text{mm}}$ even though it had previously been calculated in ZA06. The reason is that ZA06 adopted a different dust opacity law and the dust temperature for each condensation was kept in the range of 20 – 30 K due to the lack of the dust temperature map. Additionally, we made use of the high-resolution column density map with resolution similar to the 870 μm data. After measuring the mean column density ($\overline{N_{\text{H}_2}}$) and background column density ($\overline{N_{\text{H}_2}^{\text{bg}}}$) over the ellipse of each condensation, we approximated the mass M_{HOBYS} by $(\overline{N_{\text{H}_2}} - \overline{N_{\text{H}_2}^{\text{bg}}}) \times A$, where A equals $\pi R_{\text{maj}} \times R_{\text{min}}$, the area of each condensation. The background emission ($\overline{N_{\text{H}_2}^{\text{bg}}}$) for each condensation was considered by subtracting its nearby diffuse emission, with the aim of minimizing the contribution of contamination from the line of sight to the mass estimates. All measured parameters for the condensations are listed in Table 3. The derived parameters are summarized in Table 4.

The four mass groups are compared to illustrate the contribution of the flux recovery of ground-based observations to the mass estimate. As indicated in Table 4, the mass $M_{870\mu\text{m}}^{\text{Planck}}$ is on average 2.6 ± 0.5 times higher than $M_{870\mu\text{m}}$. This demonstrates the loss of large-scale emission in the APEX 870 μm map that is due to the drawback of ground-based continuum observations. This drawback can be caused in the data processing in which emission at angular scales larger than a fraction of the field of view of the telescope is filtered out in the subtraction of the sky noise (Csengeri et al. 2016). Particularly, the mass $M_{870\mu\text{m}}$ of the condensation 1 (cond.1) is most severely affected by the loss of large-scale diffuse gas emission, by 3.8 times less than $M_{870\mu\text{m}}^{\text{Planck}}$. This may be related to the least compact property of cond.1 of the eight condensations, as indicated by the contrast of the peak to mean intensities (see Fig. 5 a). The comparison of the mass $M_{870\mu\text{m}}^{\text{Planck}}$ with $M_{1.2\text{mm}}$ shows that $M_{1.2\text{mm}}$ is on average a factor 1.9 ± 0.5 lower than $M_{870\mu\text{m}}^{\text{Planck}}$, indicating that the 1.2 mm ground-based observations might have suffered from the loss of large-scale emission as well. Furthermore, space-based *Herschel* observations could be regarded as almost no loss of large-scale emission with respect to the ground-based observations. In comparison, M_{HOBYS} is found to be on average a factor 1.6 ± 0.1 as massive as $M_{870\mu\text{m}}^{\text{Planck}}$, suggesting that the mass $M_{870\mu\text{m}}^{\text{Planck}}$ is not yet completely recovered. This incomplete recovery may be attributed to the poor resolution of the Planck/HFI instrument, which cannot be demonstrated in this work because of the lack of higher resolution space observations at 870 μm or the wavelengths close to it. However, we can try to confirm the result of this incomplete recovery. Taking advantage of the high-resolution column density map, we modeled 870 μm emission according to Eq. 1 of Liu et al. (2016). The resulting map is displayed in Fig. 5 (c). Compared with the APEX+Planck

¹⁰ APEX+Planck map is a combination of the 870 μm map from the ATLASTAL survey (Schuller et al. 2009) with the 850 μm map with large angular scale ($8'$) detection from the Planck/HFI instrument. The combined map can, to some extent, recover the lost information on the distribution of diffuse gas emission resulting from the data reduction used for ground-based observations.

Table 2: Derived parameters for the 50 compact sources

ID	<i>R.A.</i>	<i>Dec.</i>	$D_{\text{dec}}^{\text{eff}}$	T_{d}	M_{env}	$n_{\text{H}_2}^a$	L_{bol}	$L_{\text{smm}}/L_{\text{bol}}$
	J2000	J2000	pc	K	M_{\odot}	10^5 cm^{-3}	L_{\odot}	
1	13:40:57.312	-61:45:42.12	0.12	25.2 ± 0.5	173 ± 16	28.5 ± 2.6	7513 ± 1503	0.005
2	13:40:26.328	-61:47:54.6	0.12	20.5 ± 0.5	92 ± 11	15.1 ± 1.7	1411 ± 282	0.010
3	13:39:54.456	-61:41:09.24	0.16	24.4 ± 0.2	204 ± 9	13.1 ± 0.6	12712 ± 2542	0.003
4	13:40:26.448	-61:47:39.84	0.13	17.4 ± 0.6	162 ± 31	18.9 ± 3.6	781 ± 156	0.022
5	13:40:32.352	-61:47:20.04	0.16	21.8 ± 1.5	42 ± 15	3.0 ± 1.1	1411 ± 282	0.005
8	13:39:54.576	-61:40:59.52	0.12	18.1 ± 1.4	270 ± 106	44.4 ± 17.4	1607 ± 321	0.019
10	13:41:01.992	-61:44:14.28	0.12	23.1 ± 0.8	12 ± 2	2.0 ± 0.4	399 ± 80	0.006
11	13:40:09.168	-61:41:31.56	0.19	25.1 ± 0.3	39 ± 2	1.6 ± 0.1	3938 ± 788	0.002
15	13:39:49.560	-61:44:30.12	0.12	25.3 ± 1.0	10 ± 2	1.6 ± 0.3	240 ± 48	0.009
16	13:40:18.456	-61:47:07.44	0.19	17.6 ± 1.0	183 ± 53	7.4 ± 2.2	616 ± 123	0.032
19	13:40:37.704	-61:46:59.88	0.19	18.6 ± 1.7	87 ± 34	3.5 ± 1.4	456 ± 91	0.023
28	13:39:54.360	-61:42:59.4	0.19	20.8 ± 0.5	25 ± 3	1.0 ± 0.1	1215 ± 243	0.003
32	13:39:45.216	-61:44:41.64	0.16	25.5 ± 0.7	9 ± 1	0.6 ± 0.1	225 ± 45	0.009
33	13:40:36.648	-61:49:29.64	0.25	19.7 ± 0.2	55 ± 3	1.0 ± 0.1	340 ± 68	0.022
37	13:41:06.912	-61:45:54.72	0.18	17.1 ± 0.8	49 ± 13	2.2 ± 0.6	347 ± 69	0.014
42	13:40:27.240	-61:36:16.56	0.24	20.3 ± 0.8	54 ± 10	1.1 ± 0.2	392 ± 78	0.020
44	13:39:39.456	-61:43:31.08	0.19	23.4 ± 1.7	23 ± 8	0.9 ± 0.3	360 ± 72	0.012
45	13:40:29.424	-61:47:28.68	0.18	14.0 ± 0.6	360 ± 80	17.3 ± 3.8	290 ± 58	0.076
47	13:40:54.624	-61:46:40.08	0.20	17.0 ± 0.2	158 ± 10	5.3 ± 0.3	429 ± 86	0.036
49	13:40:46.584	-61:46:59.16	0.29	18.3 ± 6.4	31 ± 47	0.3 ± 0.5	128 ± 26	0.028
51	13:40:27.384	-61:47:48.48	0.12	15.8 ± 0.3	121 ± 12	19.8 ± 2.0	290 ± 58	0.035
58	13:39:58.704	-61:39:56.16	0.19	22.3 ± 0.6	14 ± 2	0.6 ± 0.1	167 ± 33	0.014
61	13:40:25.704	-61:32:23.28	0.21	10.9 ± 1.1	759 ± 384	22.4 ± 11.3	100 ± 20	0.234
69	13:39:55.704	-61:46:19.56	0.20	19.9 ± 0.7	32 ± 5	1.1 ± 0.2	206 ± 41	0.021
72	13:39:38.280	-61:43:06.24	0.19	24.1 ± 0.7	17 ± 2	0.7 ± 0.1	310 ± 62	0.011
85	13:41:03.144	-61:45:22.68	0.12	14.9 ± 0.9	150 ± 47	24.7 ± 7.7	188 ± 38	0.058
86	13:40:32.424	-61:42:35.64	0.17	22.4 ± 0.6	7 ± 1	0.4 ± 0.1	85 ± 17	0.014
89	13:40:04.032	-61:40:32.16	0.25	22.9 ± 0.7	14 ± 2	0.3 ± 0.1	201 ± 40	0.013
90	13:40:11.520	-61:42:24.84	0.19	17.6 ± 0.2	75 ± 4	3.0 ± 0.2	253 ± 51	0.032
92	13:41:48.648	-61:35:20.04	0.19	16.3 ± 0.8	37 ± 9	1.5 ± 0.4	80 ± 16	0.042
111	13:39:46.512	-61:38:54.6	0.13	19.0 ± 1.0	11 ± 3	1.3 ± 0.3	57 ± 11	0.025
115	13:40:21.192	-61:52:23.88	0.18	19.7 ± 0.7	6 ± 1	0.3 ± 0.1	40 ± 8	0.022
132	13:40:56.856	-61:37:43.32	0.12	18.2 ± 2.5	10 ± 6	1.5 ± 0.9	40 ± 8	0.029
141	13:40:59.328	-61:47:01.68	0.37	19.8 ± 0.7	28 ± 5	0.1 ± 0.1	178 ± 36	0.022
154	13:40:58.512	-61:48:45	0.25	21.1 ± 0.4	19 ± 2	0.3 ± 0.1	177 ± 35	0.017
161	13:41:07.176	-61:47:51.72	0.29	20.0 ± 0.2	23 ± 1	0.3 ± 0.1	157 ± 31	0.021
263	13:39:44.208	-61:41:29.76	0.26	15.5 ± 2.0	210 ± 96	3.4 ± 1.5	339 ± 68	0.050
265	13:41:10.248	-61:44:02.4	0.24	16.3 ± 0.6	54 ± 9	1.0 ± 0.2	117 ± 23	0.042
268	13:40:37.392	-61:51:28.8	0.19	15.2 ± 0.5	63 ± 10	2.6 ± 0.4	88 ± 18	0.055
270	13:40:28.680	-61:35:17.52	0.40	14.8 ± 1.2	225 ± 67	0.9 ± 0.3	263 ± 53	0.061
271	13:41:54.888	-61:35:09.96	0.36	20.4 ± 0.2	30 ± 2	0.2 ± 0.1	231 ± 46	0.019
272	13:39:50.760	-61:41:03.12	0.19	13.6 ± 2.4	353 ± 243	14.3 ± 9.8	238 ± 48	0.085
273	13:39:47.352	-61:39:47.16	0.19	23.1 ± 0.5	11 ± 1	0.5 ± 0.1	164 ± 33	0.013
274	13:39:39.384	-61:39:52.56	0.19	14.0 ± 1.0	42 ± 15	1.7 ± 0.6	34 ± 7	0.075
278	13:39:33.936	-61:40:55.2	0.12	14.2 ± 0.8	22 ± 6	3.6 ± 1.1	19 ± 4	0.072
280	13:40:16.608	-61:33:24.48	0.29	15.8 ± 1.8	75 ± 30	0.8 ± 0.3	131 ± 26	0.047
281	13:40:57.192	-61:49:52.32	0.20	21.2 ± 0.1	8 ± 0	0.3 ± 0.1	178 ± 36	0.007
291	13:41:03.096	-61:48:30.96	0.26	12.2 ± 0.1	103 ± 6	1.5 ± 0.1	32 ± 6	0.139
298	13:39:42.312	-61:40:26.76	0.19	19.5 ± 1.7	14 ± 6	0.6 ± 0.3	83 ± 17	0.023
316	13:41:00.360	-61:46:23.88	0.35	26.2 ± 0.1	34 ± 1	0.2 ± 0.1	1024 ± 205	0.008

Notes.

^a The number density is approximated as $n_{\text{H}_2} = M_{\text{env}}/(4\pi/3 \times (D_{\text{dec}}^{\text{eff}}/2)^3 \times \mu \times m_{\text{H}})$ by assuming a sphere entity for compact sources, where the mean molecular weight μ is assumed to be 2.8 and m_{H} is the mass of a hydrogen atom.

combined map, the modeled 870 μm emission can recover more extended diffuse emission, as shown in Fig. 5 (b)–(c), which is in support of the incomplete recovery result in the APEX+Planck map.

The comparisons of the four groups of masses led to a relation of $M_{\text{HOBYS}} > M_{870\mu\text{m}}^{\text{Planck}} > M_{1.2\text{mm}} > M_{870\mu\text{m}}$. $M_{870\mu\text{m}}^{\text{Planck}} > M_{1.2\text{mm}} > M_{870\mu\text{m}}$ indicates that there are mass losses in ground-based observations due to the drawback in the data reduction. $M_{\text{HOBYS}} > M_{870\mu\text{m}}^{\text{Planck}}$ shows that the APEX+Planck combined map has not fully recovered the mass losses. It is worth noting that M_{HOBYS} may be uncertain since the background subtraction may not be estimated accurately due to the uncertain background emission

level. Therefore, $M_{870\mu\text{m}}^{\text{Planck}}$ and M_{HOBYS} are conservatively treated as lower and upper limits for the eight condensations.

5. Discussion**5.1. Evolutionary state of compact sources****5.1.1. Luminosity-mass diagram**

A promising evolutionary tool for young protostellar cores is the diagram that shows luminosity versus envelope mass ($L_{\text{bol}} - M_{\text{env}}$) (e.g., Saraceno et al. 1996; Molinari et al. 2008, 2016). It has first been used for low-mass objects

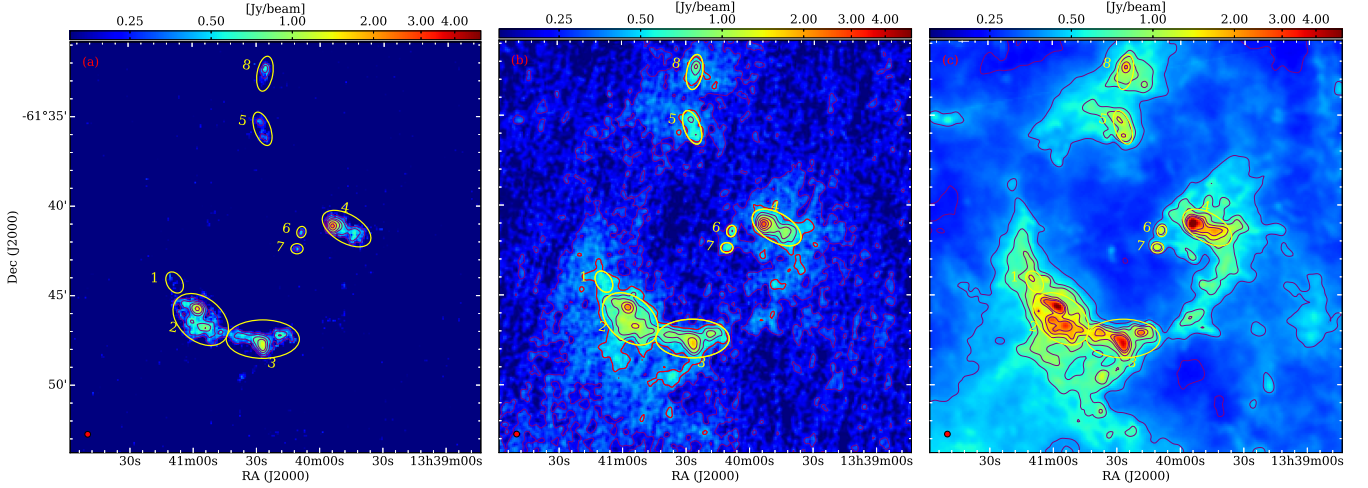


Fig. 5: (a) Observed APEX $870\ \mu\text{m}$ map, (b) APEX+Planck combined map, (c) modeled $870\ \mu\text{m}$ map by inverting from the high-resolution column density map. In all panels, the color bars are identical, going from 0.15 to $5.0\ \text{Jy beam}^{-1}$ in logarithmic scale. The purple contours show levels of 0.25, 0.40, 0.60, 0.80, 1.20, 1.60, and $2.0\ \text{Jy beam}^{-1}$. It is noteworthy that the sensitivity of the observed $870\ \mu\text{m}$ map is $0.05 - 0.07\ \text{Jy beam}^{-1}$. A beam size of $19''$ is shown on the bottom left (full red circle). Eight condensations are roughly depicted in ellipses and labeled as given in ZA06.

Table 3: Observed condensation parameters

Name	<i>R.A.</i> J2000	<i>Dec.</i> J2000	R_{maj} "	R_{min} "	$F_{870\mu\text{m}}$ mJy	$F_{870\mu\text{m}}^{\text{Planck}}$ mJy	$F_{1.2\text{mm}}^{\text{a}}$ mJy	$\overline{T_{\text{d}}}$ K	$\overline{N_{\text{H}_2}}$ $10^{22}\ \text{cm}^{-2}$	$N_{\text{H}_2}^{\text{bg}}$ $10^{22}\ \text{cm}^{-2}$
cond1	13:41:08.560	-61:44:17.43	25.9	38.2	514	1974	224	22	2.0	0.6
cond2	13:40:56.013	-61:46:21.92	105.2	72.1	8828	23240	4200	22	2.9	0.6
cond3	13:40:26.940	-61:47:27.88	122.6	64.5	7567	17833	2350	21	2.3	0.5
cond4	13:39:47.435	-61:41:17.14	90.2	47.6	6198	12585	3000	22	2.9	0.5
cond5	13:40:27.041	-61:35:42.84	26.8	58.8	1179	3088	795	20	2.1	0.7
cond6	13:40:08.717	-61:41:29.01	15.4	19.1	272	574	81	23	1.7	0.6
cond7	13:40:10.802	-61:42:24.84	20.5	17.1	281	665	144	21	2.0	0.5
cond8	13:40:25.868	-61:32:38.16	26.3	59.3	1088	3062	483	18	2.8	0.7

Notes.

^a $F_{1.2\text{mm}}$ is the 1.2 mm flux retrieved from Table 2 of ZA06.

Table 4: Derived condensation parameters

Name	$R_{\text{maj}} \times R_{\text{min}}$ pc \times pc	$M_{870\mu\text{m}}$ M_{\odot}	$M_{870\mu\text{m}}^{\text{Planck}}$ M_{\odot}	$M_{1.2\text{mm}}$ M_{\odot}	M_{HOBYS} M_{\odot}	<i>CFE</i>	n_{Cond} $10^3\ \text{cm}^3$
cond1	0.8×0.8	71	272	100	424	0.13 ± 0.02	6.3
cond2	2.2×2.2	1219	3208	1874	5337	0.11 ± 0.02	3.7
cond3	2.6×2.6	1094	2578	1094	4355	0.24 ± 0.06	3.2
cond4	1.9×1.9	872	1772	1363	3153	0.33 ± 0.07	5.9
cond5	1.2×1.2	181	475	392	675	0.39 ± 0.12	6.1
cond6	0.4×0.4	35	74	34	99	0.39 ± 0.02	8.3
cond7	0.4×0.4	41	97	67	161	0.47 ± 0.03	10.2
cond8	1.2×1.2	199	559	277	1002	0.76 ± 0.38	9.3

(Saraceno et al. 1996) and was then extended to high-mass objects (Molinari et al. 2008). The diagram of Molinari et al. (2008) is a result of simulations based on the assumption of a scaled-up version of classical inside-out collapse scenario (Shu 1977). The simulations can be summarized as two phases of accelerating accretion and envelope clean-up. During the accelerating accretion, its rate increases with time since the inside-out collapse wave propagates outward, reaching out to material dominated by supersonic speeds and where higher accretion rates are possible (McKee & Tan 2003). Despite the fast accretion onto a central proto-

star, its envelope mass decreases slowly with time due to the main mass loss by powerful molecular outflows. In contrast, the bolometric luminosity of the protostellar core increases drastically due to the contributions from accretion, deuterium burning, and core contraction. In the $L_{\text{bol}} - M_{\text{env}}$ diagram (see Fig. 6) the tracks (the dot-marked full thick lines) all start at very low luminosity and proceed almost vertically toward the zero-age main sequence (ZAMS), which marks the end of the accelerating accretion phase. In the early ZAMS phase, the bolometric luminosity of the core remains constant, while its envelope mass continues

to be expelled through radiation and molecular outflows. The evolution of the protostellar core then enters the second envelope clean-up phase in which a large amount of material is expelled predominantly by energetic radiation and powerful outflows, and then the luminosity mainly arises from the protostar and the persisting residual accretion. The envelope clean-up phase shown in the $L_{\text{bol}} - M_{\text{env}}$ diagram is that the protostellar core evolves along an almost horizontal path (the dashed diamond-marked lines), which ends when the envelope is all almost expelled and the protostar becomes optically visible. Although this diagram has been widely adopted for the investigation of young massive and dense cluster-progenitor clumps, it should be treated with caution due to several intrinsic caveats (Molinari et al. 2008; Traficante et al. 2015). For instance, the evolutionary tracks were initially modeled for single cores, not for clumps, while our compact sources with a typical size of 0.2 pc can consist of multiple sources in different evolutionary stages. Therefore, the evolutionary stages of the 50 compact sources derived from this diagram have to be taken with caution in the following analysis.

5.1.2. Evolutionary trend

Figure 6 shows the distribution of the 50 compact sources in the $L_{\text{bol}} - M_{\text{env}}$ diagram. *Group 0* sources are coded in red, *Group IM* in green, and *Group I* in blue. In Fig. 6 the *Group 0* compact sources are distributed above the starting points from the bottom of all the evolutionary tracks, which could be regarded as the beginning of the accretion phase. Their distribution suggests that they may be protostellar sources although they are associated with $8 \mu\text{m}$ absorption, which is indicative of no active ongoing star formation. This may be attributed to the fact that the low-luminosity protostars deeply embedded in the dense clumps are not observable in the near- and mid-IR continuum observations. Given the above consideration, *Group 0* will be treated as protostellar sources in the following analysis. However, it is worthwhile to determine the nature of these *Group 0* sources using millimeter interferometric observations of molecular tracers of ongoing star-forming activities (e.g., outflows and infall). Furthermore, the majority of *Group 0* sources can be distinguished from the *Group IM* and *Group I* sources. Most of *Group 0* sources are located in the lower part of the $L_{\text{bol}} - M_{\text{env}}$ diagram than the other two groups. This fact suggests an evolutionary trend of *Group 0* sources being the least evolved of the three groups.

The $L_{\text{submm}}^{\lambda > 350} / L_{\text{bol}}$ ratio between the submillimeter ($\lambda > 350 \mu\text{m}$) and bolometric luminosities is thought to be useful for exploring the nature of protostellar cores and their evolutionary trend (e.g., André et al. 2000; Bontemps et al. 2010a). According to Bontemps et al. (2010a), sources with $L_{\text{submm}}^{\lambda > 350} / L_{\text{bol}} \geq 0.03$ are classified as class 0 objects, sources with $0.01 < L_{\text{submm}}^{\lambda > 350} / L_{\text{bol}} < 0.03$ as intermediate (IM) objects, and sources with $L_{\text{submm}}^{\lambda > 350} / L_{\text{bol}} \leq 0.01$ as class I objects. The so-called IM objects are regarded as those in the transition regime where Class 0 and I objects are not readily distinguishable. This classification scheme sorts the 50 compact sources into 17 class 0, 23 IM, and 10 class I protostellar cores. We observed that 1 out of 17 class 0 (number 51), and 5 out of 23 IM (numbers 2, 4, 7, 8, and 19) protostellar cores are associated with point-like IR counterparts. These sources, except for source 4, were identified as class I ob-

jects by the mid-IR color-color diagrams in ZA06. However, source 4 was not mentioned in ZA06. Likewise, we make use of the color-color scheme of Allen et al. (2004), adopted in ZA06, to investigate the nature of this source. As a result, the colors of $[3.6] - [4.5] \approx 1.5$ and $[5.8] - [8.0] \approx 1.2$ for source 4 suggest that it is a class I object. Finally, we obtain 16 class 0, 19 IM, and 15 class I protostellar cores, which are marked in small, medium, and large circles in Fig. 6, respectively. Table 5 summarizes the association of the three classes of objects with the three groups of sources as defined in Sect. 4.3.3. By comparison, 81% of class 0 objects are found to be associated with *Group 0* sources with $8 \mu\text{m}$ absorption, 95% of IM objects associated with *Group IM* sources with extended IR features, and 100% of class I objects associated with *Group IM/I* sources. These results demonstrate that the *Group 0* sources are indeed in the earliest evolutionary stages of the three groups since the majority of the *Group 0* sources can be categorized into class 0 objects. Hereafter, the definition of *Group* will be replaced with that of class since the latter is more unbiased and physically meaningful.

As shown in Fig. 6, all the class 0, IM, class I protostellar cores follow the evolutionary tracks well. The class I protostellar cores are the most luminous, approaching the ZAMS phase as indicated by the solid line given by Molinari et al. (2008). The IM and class 0 objects are less luminous, situated below the class I objects in the $L_{\text{bol}} - M_{\text{env}}$ diagram. These results are well consistent with the known evolutionary trend that class 0 objects are less evolved and have lower luminosities than class I objects (e.g., André et al. 1993, 2000; Dunham et al. 2008; Evans et al. 2009; Enoch et al. 2009).

5.1.3. Properties of compact sources in different phases

Figure 7 shows the distributions of three physical parameters (T_{d} , M_{env} , and L_{bol}) for the three classes of objects. In Fig. 7(a), the source temperature increases as a function of evolutionary stage, with average values of 15.0 ± 1.7 , 20.2 ± 2.0 , and 23.4 ± 1.9 K for the class 0, IM, and class I protostellar cores, respectively. This trend with increasing temperature can be understood as the central protostar(s) being the dominant heating engine of a core. The envelope mass distributions of the sources are shown in Fig. 7(b). The mean masses are 118 ± 2 , 26 ± 3 , and $30 \pm 3 M_{\odot}$ for the class 0, IM, and class I protostellar cores, respectively. We note that the lower mean mass of the IM protostellar cores than that of the class I protostellar cores may not be true. This may arise from the exclusion of the $70 \mu\text{m}$ flux in the graybody SED fitting. Such exclusion underestimates the dust temperature, especially for the class I protostellar cores, leading to a corresponding overestimated envelope mass (see more discussions in Traficante et al. 2015). Despite this possible overestimation of class I envelope mass, a decreasing mass trend from class 0 to IM and class I protostellar cores is present. This suggests that class 0 protostellar cores should have more mass for entering the accelerating accretion phase and class I protostellar cores have to decrease in mass due to the envelope clean-up process (see Sect. 5.1.1, and Fig. 6). The luminosity distributions of the sources are shown in Fig. 7(c), with mean values of 144 ± 3 , 197 ± 2 , and $1097 \pm 4 L_{\odot}$ for the class 0, IM, and class I protostellar cores, respectively. The increasing luminosity trend with evolu-

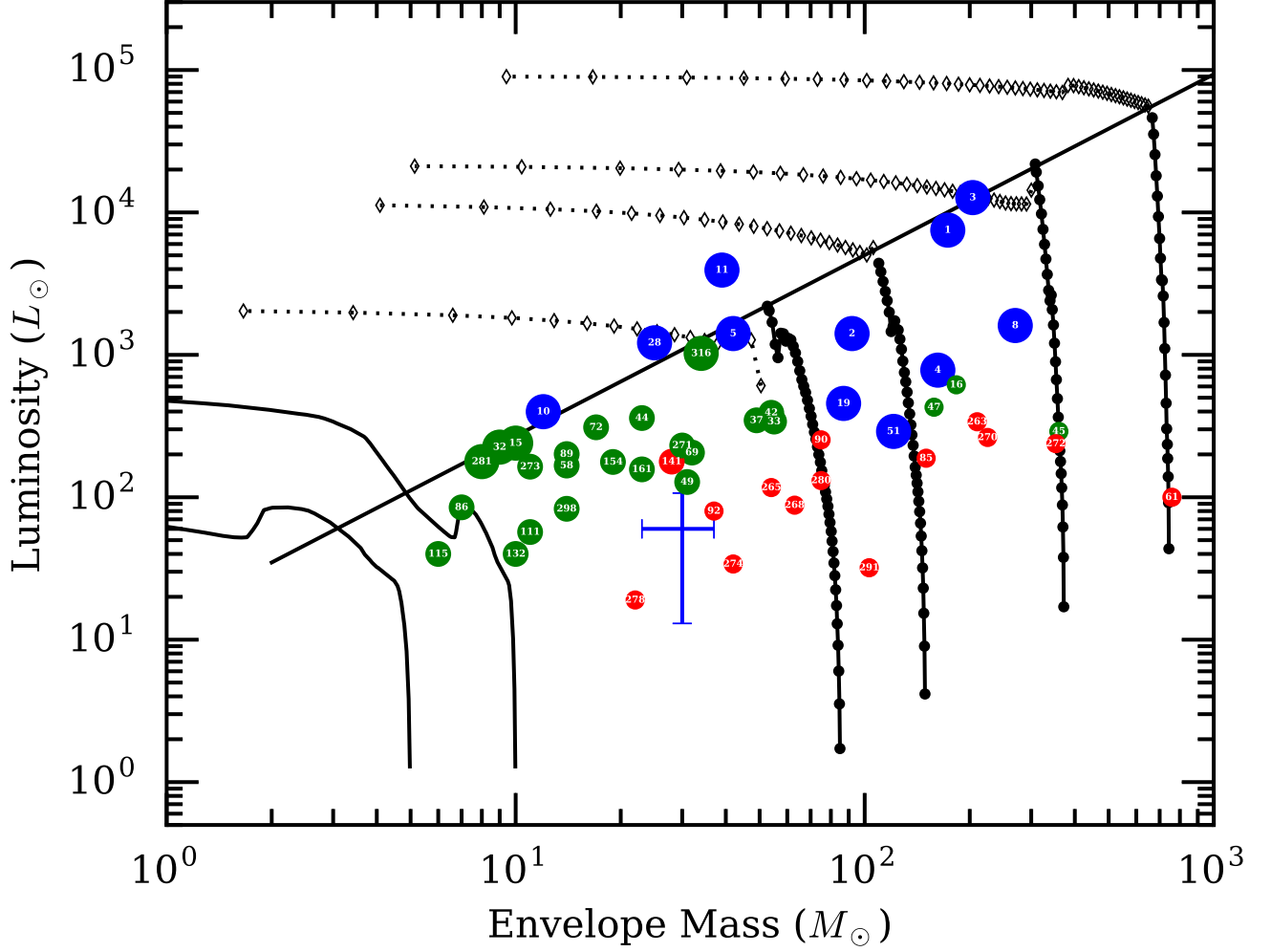


Fig. 6: Bolometric luminosity vs. envelope mass ($L_{\text{Bol}}-M_{\text{Env}}$) diagram. Red circles show the compact sources associated with $8\mu\text{m}$ absorption, green circles indicate sources associated with IR extended emission, and blue circles symbolize sources associated with IR point-like objects. As described in Sect 5.1.2, these compact sources are classified as class 0 (small circles), intermediate objects (medium circles), and class I (large circles). Typical error bars are shown.

Table 5: Statistics of IR features and evolutionary diagnostics of 50 compact sources

Sources associated with IR features	Class 0	Intermediate object	Class I
Absorption at $8\mu\text{m}$ (14) [<i>Group 0</i>]	13	1	0
Extended IR emission (25) [<i>Group IM</i>]	3	18	4
Point-like IR objects (11) [<i>Group I</i>]	0	0	11
Total (50) [<i>Groups 0, IM, I</i>]	16	19	15

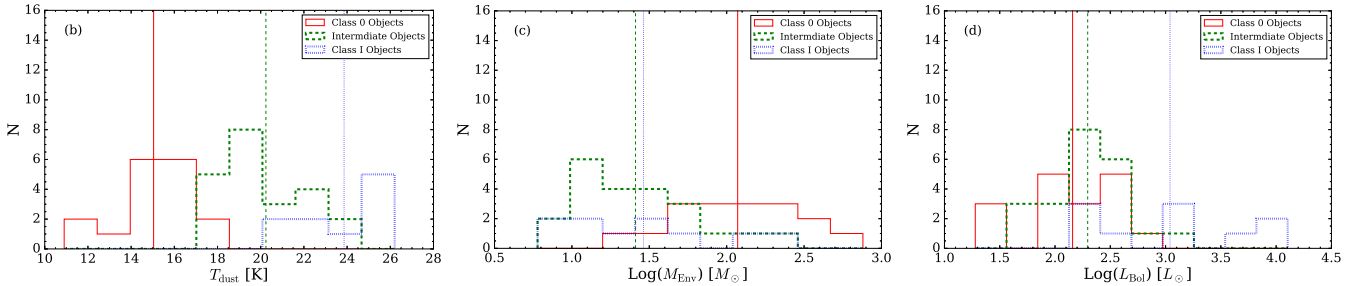


Fig. 7: Histograms of the dust temperature (a), envelope mass (b), and bolometric luminosity (c) for the 50 compact sources. Average values are marked with the solid, dashed, and dash-dotted lines for class 0, IM, and class I objects, respectively.

tionary stage is also in agreement with the evolutionary tracks shown in Fig. 6 (see Sect. 5.1.1).

From the mass and luminosity distributions, their consistencies with the evolutionary tracks in Fig. 6 demonstrate that the 50 compact sources in RCW 79 are indeed in the early stages of star formation. The nature of these compact sources needs to be explored in more detail with observations of higher angular resolution since their typical size (~ 0.2 pc) is not the minimum scale of the final fragmentation (i.e., $\sim 0.01 - 0.04$ pc) leading to individual collapsing protostars (e.g., Bontemps et al. 2010b; Palau et al. 2013; Wang et al. 2014, Motte et al. in prep.). A possible way of addressing this is either to look at the number of IR protostars within the protostellar cores (~ 0.2 pc), or to identify cold dense substructures within them using millimeter interferometric observations.

5.2. High-mass star-forming candidates

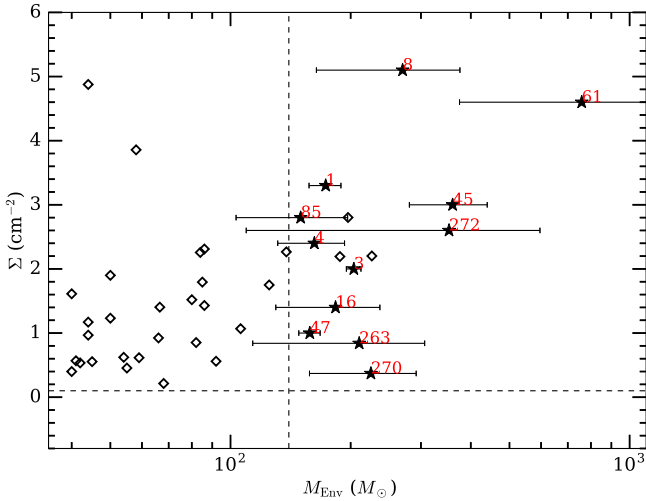


Fig. 8: Surface density versus envelope mass for the massive dense cores (MDCs) in RCW 79 (filled stars) and those in Cygnus X (open diamonds, Motte et al. 2007). The vertical dashed line is the mass threshold $> 140 M_{\odot}$ for MDCs in this work. The horizontal dashed line represents a surface density threshold of $\Sigma = 0.1 \text{ g cm}^{-2}$ as suggested in the literature (e.g., Butler & Tan 2012; Tan et al. 2013, 2014; Traficante et al. 2015).

Triggered star formation around H II regions may be an important process, especially for high-mass star formation (e.g., Deharveng et al. 2010; Thompson et al. 2012; Kendrew et al. 2012, 2016, Palmeirim et al. submitted). It is therefore worthwhile to search for massive dense cores (MDCs) that may form high-mass stars in RCW 79.

We use the L - M_{env} diagram to determine the mass threshold of MDCs. Based on Eq. 10 of Molinari et al. (2008), a dense core with $M_{\text{env}} > 140 M_{\odot}$ may form a massive star of $> 8 M_{\odot}$. This corresponds to the last three tracks from left to right in Fig. 6. An alternative way of determining the mass threshold of MDCs is to match the compact sources with the known signposts of ongoing high-mass star formation, such as class II methanol maser, bright SiO emission, and ultracompact H II regions (e.g., Motte

et al. 2007; Russeil et al. 2010, Tigé et al. 2016, submitted), leading to a lower mass limit for the sources associated with the signposts, which can be adopted as the minimum mass for MDCs. Table 6 gives a statistics of massive dense cores classified by searching for signs of high-mass star formation in two nearby high-mass star-forming regions. The mass threshold of the MDCs in NGC 6334 is about twice higher than that in Cygnus X. This difference could be caused by different environments (e.g., different number densities in Table 6, see below), given the same typical scale of the MDCs and similar mass sensitivities between observations by Motte et al. (2007) and Tigé et al., (2016). In RCW 79, we do not have enough signposts of ongoing star formation (only source 1 with maser emission) to do a statistic, therefore we adopted the $140 M_{\odot}$ determined from the L - M_{env} diagram as the mass threshold for candidate MDCs in RCW 79. When we assume that the compact sources have a density gradient of $\rho \propto r^{-2}$, the minimum mass of MDCs with a typical size of ~ 0.2 pc (see Table 6) needs to be twice higher than that in NGC 6334. The mass threshold of $140 M_{\odot}$ is about 2 and 3.5 times higher than those in NGC 6334 and Cygnus X, respectively, therefore $140 M_{\odot}$ may not be the actual minimum mass for the MDCs in RCW 79, but is a conservative value. There are 12 MDC candidates in RCW 79 according to these criteria. They have densities ranging from 0.9 to $4.6 \times 10^6 \text{ cm}^{-3}$ with an average value of $1.6 \times 10^6 \text{ cm}^{-3}$. In comparison, the MDCs in RCW 79 are found on average to be not as dense as those in NGC 6334, but about 5 times denser than those in Cygnus X (see Table 6). This is suggestive of the dense properties of the MDCs in RCW 79.

The mass surface density Σ is believed to be a potential measure to investigate the environment of massive star formation (e.g., Krumholz & McKee 2008; Tan et al. 2014; Traficante et al. 2015). The models of Krumholz & McKee (2008) suggested $\Sigma \geq 1 \text{ g cm}^{-2}$ as a threshold to avoid the fragmentation of clouds into low-mass cores, thus allowing high-mass star formation. However, this threshold has been found to be variable in observations (Tan et al. 2014; Traficante et al. 2015). The surface densities of the 12 candidate MDCs are shown in Fig. 8, in which the 33 MDCs of $> 40 M_{\odot}$ in Cygnus X are included for comparison. The surface densities of the MDC candidates in RCW 79 range from $\sim 0.4 - 5.1 \text{ g cm}^{-2}$. This range is in agreement with that of the MDCs in Cygnus X, indicating that the 12 candidate MDCs are probably the precursors of high-mass star formation. Ten out of 12 MDCs in RCW 79 have surface densities $\geq 1 \text{ g cm}^{-2}$. For the other two MDCs 263 and 270, their large sizes (0.26 pc for MDC 263, and 0.4 pc for MDC 270) among the 12 MDCs may lead to their lowest surface densities with $\Sigma < 1 \text{ g cm}^{-2}$ as shown in Fig. 8. However, their surface densities are still within $0.1 \leq \Sigma \leq 1 \text{ g cm}^{-2}$ observed in several high-mass cores (e.g., Butler & Tan 2012; Tan et al. 2013, 2014).

Triggering may be an important mechanism for high-mass star formation (e.g., Deharveng et al. 2010; Thompson et al. 2012; Kendrew et al. 2012, 2016). In the Red MSX MYSOs catalog (see Sect. 1), only one MYSO object associated with MDC 1 is included, showing that 11 out of 12 MDCs are new additional MYSO candidates with respect to the existing MYSOs catalog. This can be attributed to the advantages of *Herschel* observations, which are more sensitive to embedded YSOs than those at shorter wavelengths. If the increase of the MYSOs number in RCW 79

Table 6: Statistics of massive dense cores

Region	Dist [kpc]	M_{th} [M_{\odot}]	Size [pc]	$n_{\text{MDC}} [\text{cm}^{-3}]$			Ref.
				Min ^a	Mean ^a	Max ^a	
Cygnus X	1.7	40	0.1	1.2×10^5	3.3×10^5	1.9×10^6	Motte+2007
NGC 6334	1.75	75	0.1	1.0×10^5	6.0×10^6	$> 7.0 \times 10^7$	Tigé+2016
RCW 79	4.3	140	0.2	9.4×10^5	1.6×10^6	4.4×10^6	This paper

Notes. ^a The range of the volume-averaged density: minimum (Min), mean (Mean), and maximum (Max) densities.

due to *Herschel* observations can be extrapolated to other H II regions or bubbles, then the fraction of high-mass stars observed toward the edges of H II regions or bubbles would be higher than than 14–30% suggested by Deharveng et al. (2010); Thompson et al. (2012); Kendrew et al. (2012). This shows that it is worthwhile to carry out a more complete statistic to the MYSOs around H II regions or bubbles in the light of *Herschel* observations to understand the interplay between H II regions and high-mass star formation (Palmeirim et al. 2016, submitted).

5.3. Star formation in massive condensations

5.3.1. Young stellar contents

Stellar contents of the three most massive condensations have partly been discussed in the light of near- and mid-IR data (ZA06), with 19 luminous class I YSOs revealed. In this section, we continue to discuss the stellar contents of these three condensations and the other five condensations to explore the early stages of star formation in them.

Condensation 2

This is the most massive condensation in RCW 79 with a mass of $\sim 3200 - 5300 M_{\odot}$. It is located in the southeastern edge, facing bright $\text{H}\alpha$ emission (see Fig. 2(c)) and is associated with the luminous PDRs seen in $8 \mu\text{m}$ emission (Fig. 9(b)), indicating the influence of ionized gas on cond. 2. This suggests that star formation in early stages might have been affected by the H II region. The high-resolution density map reveals several density peaks toward cond. 2. They are almost spatially coincident with the $870 \mu\text{m}$ continuum emission peaks (see Fig. 9(a)), which demonstrates the cold and dense characteristics of cond. 2. Additionally, this condensation overlaps most part of the CH II region (see Fig. 9). In the northwest of the CH II region is more diffuse gas, which could be attributed either to the gas dispersal by the twofold influences from the CH II region and the H II region RCW 79 or to the inhomogeneity of initial medium in which the CH II region forms and evolves.

Seven compact sources are found within cond. 2, including two class 0 (sources 47 and 85), three IM (sources 37, 49, and 141), and two class I (sources 1 and 316) objects classified by the ratio of their $L_{\lambda > 350} / L_{\text{bol}}$. Another nine class I YSOs (see Fig. 1) are rather luminous in the near IR bands (ZA06). As shown in Fig. 9, three of them are located around source 1, which is indicative of a small cluster of star formation around source 1. Another two of the nine class I YSOs are centered on the CH II region. The remaining four are located on its southern edge, close to source 141. Three of the seven compact sources are MDCs 1, 47, and 85 (see Sect. 5.2). Source 1 is situated at the center of the CH II region and close to its ionizing stars. According to Eq. 10

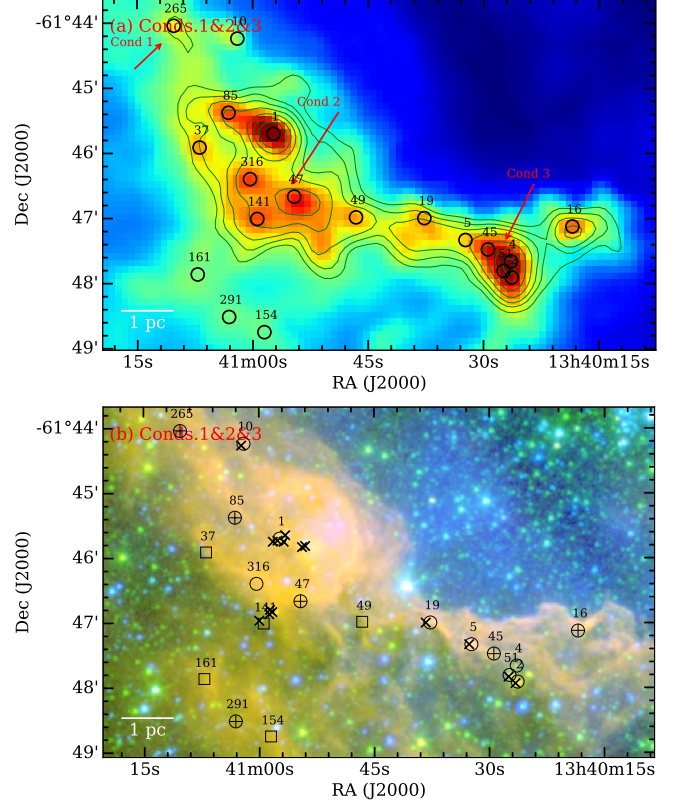


Fig. 9: (a): Compact sources (circles) overlaid on high-resolution ($18''/2$) column density map. Contours represent $870 \mu\text{m}$ continuum emission, showing levels of $[0.55, 0.65, 0.75, 0.9, 1.1, 1.3, 1.5] \text{Jy beam}^{-1}$ ($\sigma = 0.05 - 0.06 \text{Jy beam}^{-1}$). (b): Compact sources overlaid on a three-color image. The $\text{H}\alpha$, $3.6 \mu\text{m}$, and $8.0 \mu\text{m}$ emission are coded in blue, green, and red, respectively. The compact sources are symbolized in plus circles for class 0, in squares for IM, and in circles for class I objects. Crosses denote the class I YSOs identified by ZA06.

of Molinari et al. (2008), source 1 may form a high-mass star with a final stellar mass of $\sim 9 M_{\odot}$. We note that the final stellar mass is very uncertain at least since the compact source with a typical scale of $\sim 0.1 \text{pc}$ can probably fragment into smaller fragments with smaller scales (e.g., Bontemps et al. 2010b). Moreover, source 1 is surrounded by another three class I YSOs, which suggests that massive stars form in clusters (e.g., Lada & Lada 2003). The other two massive sources 47 and 85 are located at the edge of the CH II region, which most likely will lead to a high-mass star of $\sim 8 M_{\odot}$ for each of them.

Condensation 3

This is a massive condensation with a mass of $\sim 2600 - 4300 M_{\odot}$, situated in the southern part of RCW 79. It is extended along the ionized gas (see Fig. 2(c)) and is associated with PDR (see Fig. 9(b)), suggesting the interaction between the H II region and the condensation. It is composed of three density peaks as seen in both the column density map and in $870 \mu\text{m}$ continuum emission (see Fig. 9(a)). The density peaks revealed by the column density map and $870 \mu\text{m}$ emission are well consistent in the densest region, but shifted about $5''$ in the two lower-density regions. The other density peaks in the rest of the map seem to be well consistent between the column density map and $870 \mu\text{m}$ emission, therefore, the density peaks shifted in cond. 2 may be caused by physical environments instead of the astrometry problem. The temperature distribution of this condensation shows that the two lower density regions are warmer than the densest region (see Fig. 2(b)). Therefore, the peak shifts between the column density map and $870 \mu\text{m}$ emission could be interpreted as that the temperatures probed by *Herschel* observations are higher than by $870 \mu\text{m}$ observations.

with the other lower-density peak. It is a class 0 candidate and may form a massive star of $\sim 9 M_{\odot}$. The densest region in cond. 3 contains five compact sources (sources 2, 4, 5, 45, and 51). This region has the highest number of embedded YSOs compared with the other regions in RCW 79. There are two high-mass YSO candidates (i.e., sources 4 and 45). Source 4 is classified as a class I object in Fig. 6, associated with a bright star in the near- and mid-IR bands. Source 45 is regarded as class 0 in Fig. 6. In the densest region, the other three sources 2, 5, and 51 probably form intermediate-mass stars. Source 2 is a class I object with IR counterparts in near- and mid-IR bands. Source 5 is luminous at near- and mid-IR wavelengths and appears as a class I object in Fig. 6, which agrees with the result of ZA06. Source 51 is categorized as class 0 by the ratio of $L_{\text{submm}}^{\lambda > 350} / L_{\text{bol}}$, which is inconsistent with the classification as a class I by the color-color diagram (ZA06). This inconsistency may be because the class I objects detected in the near- and mid-IR bands are only overlapping with the compact source in the line of sight, but are not centered inside this compact source, which needs to be further confirmed.

Condensation 4

This is a massive condensation, with a mass of $\sim 1800 - 3100 M_{\odot}$, in the western edge of RCW 79. The bright edge of this condensation is adjacent to the ionized gas (see Figs. 2(c) and 10(b)). This suggests this condensation is under the influence of the ionized gas. Condensation 4 consists of two density peaks as shown in Fig. 10(a). Four compact sources are situated in this condensation. Sources 3, 8, 263, and 272 are associated with the densest peaks and probably form high-mass stars of $8 - 13.5 M_{\odot}$. Source 3 is detected at mid-IR wavelengths. It is classified as a class I object in Fig. 6, which is in good agreement with the result of ZA06. Source 8 is also a class I object associated with a point-like source in mid-IR bands. Coupled with its high luminosity of $\sim 1600 L_{\odot}$, source 8 is a young massive class I object (B2-3V). Sources 263 and 272 are classified as massive class 0 objects in Fig. 6 and are associated with $8 \mu\text{m}$ absorption.

Around the condensation are six sources (sources 58, 89, 273, 274, 278, and 298). They are centered on the local density peaks of more diffuse gas relative to the condensation. Sources 58, 89, 273, and 298 are classified as IM candidates according to their luminosities. They all are associated with IR extended features. In addition to the IM candidates, there are two class 0 candidates 274 and 278, which are both characterized with $8 \mu\text{m}$ absorption.

Five other condensations

Condensation 1 is located in the southeastern edge of RCW 79 and next to cond. 2, with a mass of $\sim 270 - 420 M_{\odot}$. In this condensation, there is one embedded class 0 protostar (source 265, see Fig. 9).

Condensations 6 and 7 have a mass of $\sim 70 - 100 M_{\odot}$ and $\sim 100 - 160 M_{\odot}$, respectively. They are located in the direction of the H II region, indicating that they may be fully exposed to the ionized gas. Of interest are their appearances as cometary globules (see Fig. 10(b)). One class I object (source 11, see Fig. 6) in cond. 6 and one class 0 object (source 90) in cond. 7 are located at the head of the two cometary globules, respectively. These two youngest protostars indicate that cond. 6 is more evolved than cond. 7. Furthermore, the appearance of the cometary globules with protostellar cores forming at their heads is reminiscent of the scenario of the radiation-driven implosion (RDI) process (e.g. Bertoldi 1989; Lefloch & Lazareff 1994). This pro-

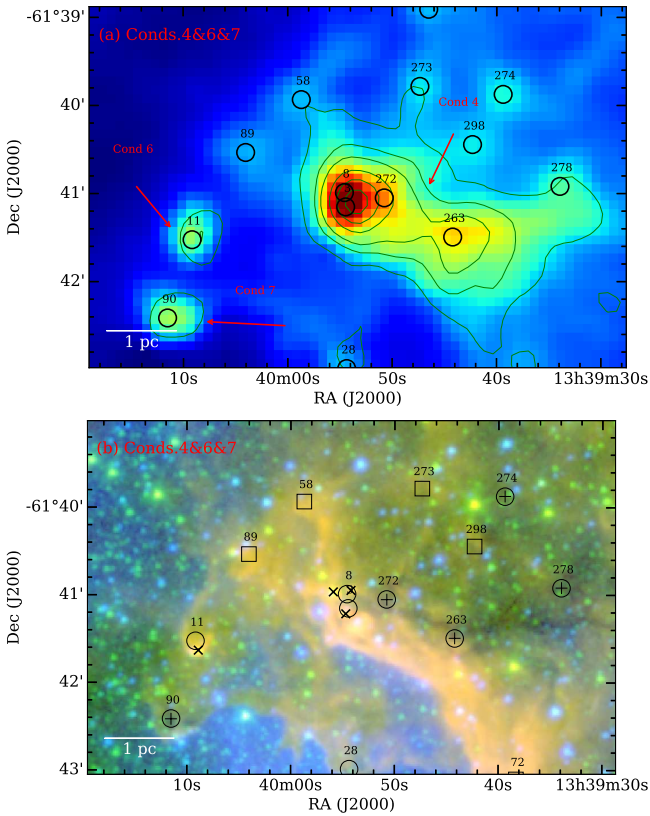


Fig. 10: As Fig. 9, but for condensations 4, 6, and 7. The contours represent levels of $[0.4, 0.6, 0.8, 1.2, 1.6, 2.0] \text{ Jy beam}^{-1}$.

Seven compact sources (sources 2, 4, 5, 16, 19, 45, and 51) are detected in this condensation. Source 19 is located in one of the two lower-density peaks (see Fig. 9(a)). This source contains a bright mid-IR point-like object. It is classified as a class I object (see Fig. 6), which is in good agreement with the classification by ZA06 (see Fig. 9(b) and Table B.3). As indicated in Fig. 6, this source may form an intermediate-mass star of $6 - 8 M_{\odot}$. Source 16 is associated

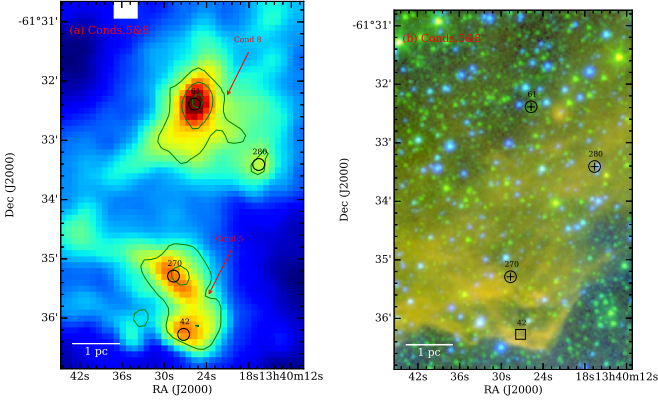


Fig. 11: As Fig. 9, but for condensations 5 and 8. The contours show levels of $[0.4, 0.6, 0.8]$ Jy beam $^{-1}$.

cess models the scenario that the pressure exerted by ionized gas on the surface of a compact source can lead to its implosion, to the formation of a cometary globule with a dense head and a tail extending away from the ionizing source, and finally to the collapse of the dense head to form a new generation of stars.

Figure 11 displays conds. 5 and 8 located in the northern part of RCW 79. They have a mass of $\sim 470 - 670 M_{\odot}$, and $\sim 560 - 1000 M_{\odot}$, respectively. Condensation 5 is on the northern edge of RCW 79 and is associated with bright PDRs as seen in $8 \mu\text{m}$ emission (see Fig. 11(b)), but cond. 8 is about 5 pc away from the edge and may not be very tightly associated with the PDR, as seen in the relatively dark $8 \mu\text{m}$ emission. This implies that cond. 5 is more affected by ionized gas from the H II region than cond. 8. There are one IM (source 42) and one class 0 (source 270) protostellar core in cond. 5, and one class 0 protostellar core (source 61) in cond. 8. Of these protostellar cores, two class 0 (sources 270 and 61) would form high-mass stars, as seen in Fig. 6. We note that the mass of source 61 should be treated with caution because of its large uncertainty of 50%. This uncertainty may be caused by the flux measurements, which are not good enough at $160 \mu\text{m}$.

Eight massive condensations are observed around RCW 79. Five of them (conds. 1, 2, 3, 4, and 5) are distributed on its edge, associated with bright PDRs, and exposed to ionized gas. These observed characteristics demonstrate that these condensations must have been inevitably affected by the H II region, which is in agreement with the existence of the ionization compression (see Sect. 4.2). According to ZA06 and Walch et al. (2011), the formation of these five condensations may be a result of the “collect and collapse” (C & C) process¹¹. The two other condensations, conds. 4, and 5, may form under the RDI process because they appear as cometary globules with young protostar cores at their heads. Condensation 8 may be a pre-existing compact source because it is located about 5 pc away from the edge of RCW 79. All this suggests that multiple physical processes (e.g., C & C and RDI) may be responsi-

¹¹ The ‘collect and collapse process models a scenario in which a shell of compressed gas can be accumulated and become denser between the ionization front and the shocked front during the expansion of an H II region, likely leading to a gravitational collapse to form the next generation of stars in due time (Elmegreen & Lada 1977).

ble for the formation of the condensations around RCW 79 and even for the star formation therein, which is consistent with the conclusion of ZA06.

A total of 22 young protostar candidates are detected in the 8 massive condensations. Class 0/I YSOs can be regarded as a new generation of stars since they are much younger than the H II regions. Evans et al. (2009) and Enoch et al. (2009) suggested that the entire embedded phase for a protostar ($\tau_{\text{Class 0}} + \tau_{\text{Class I}}$) lasts about 5.4×10^5 yr. Martins et al. (2010) estimated a photometric age of 2.3 ± 0.5 Myr for the ionizing cluster of RCW 79, which is in good agreement with a dynamical age of 2.2 ± 0.1 Myr derived by Tremblin et al. (2014a). This means that the age of RCW 79 is about one order of magnitude older than that of the class 0 and/or I YSOs. Given this timescale difference, the youngest protostars in these condensations can be affected by the H II region in RCW 79 during its expansion, which is demonstrated by the association of the condensations with bright PDR emission (see Figs. 9 and 10). Further to the influences from the H II region, additional influence for cond. 2 from the associated CH II region might have affected its nearby youngest protostars. The lifetime of the CH II region was estimated to be in the range of 0.5 to 2.0 Myr (Martins et al. 2010). It is assumed to be 0.5 Myr in this paper since the statistical lifetime of CH II regions has been estimated to be $\sim 6 \times 10^5$ yr in Cygnus X (Motte et al. 2007). Therefore, the CH II region may be as young as the class 0 and/or I YSOs and has had enough time to affect its nearby youngest protostars.

5.3.2. Core formation efficiency

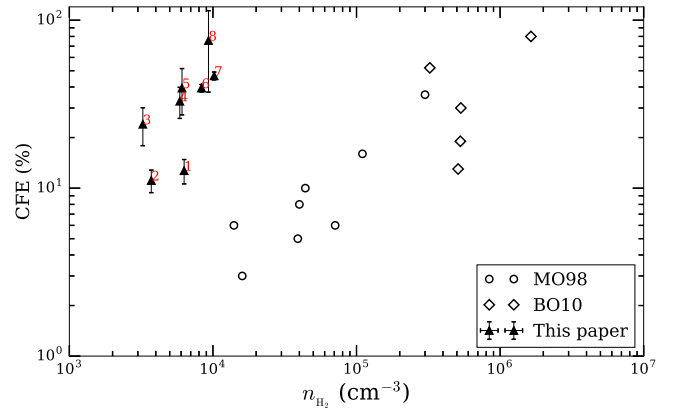


Fig. 13: Core formation efficiency as a function of the density. The filled triangles represent the condensations of pc-scale sizes in RCW 79. The dense cores of ~ 0.1 pc scales in the ρ Ophiuchus (Motte et al. 1998) and Cygnus X (Bontemps et al. 2010b) clouds are denoted as open circles and diamonds, respectively.

The association of the 50 compact sources with $8 \mu\text{m}$ emission (see Fig. 12) demonstrates the interplay between the H II region with star formation. We observed that 22 out of 50 compact sources may form a new generation of stars since they are located in the 8 coldest, densest and most massive condensations that are gravitationally bound (see Fig. 4). Therefore, we tentatively investigated the core formation efficiency (CFE) for the 8 condensations. The CFE

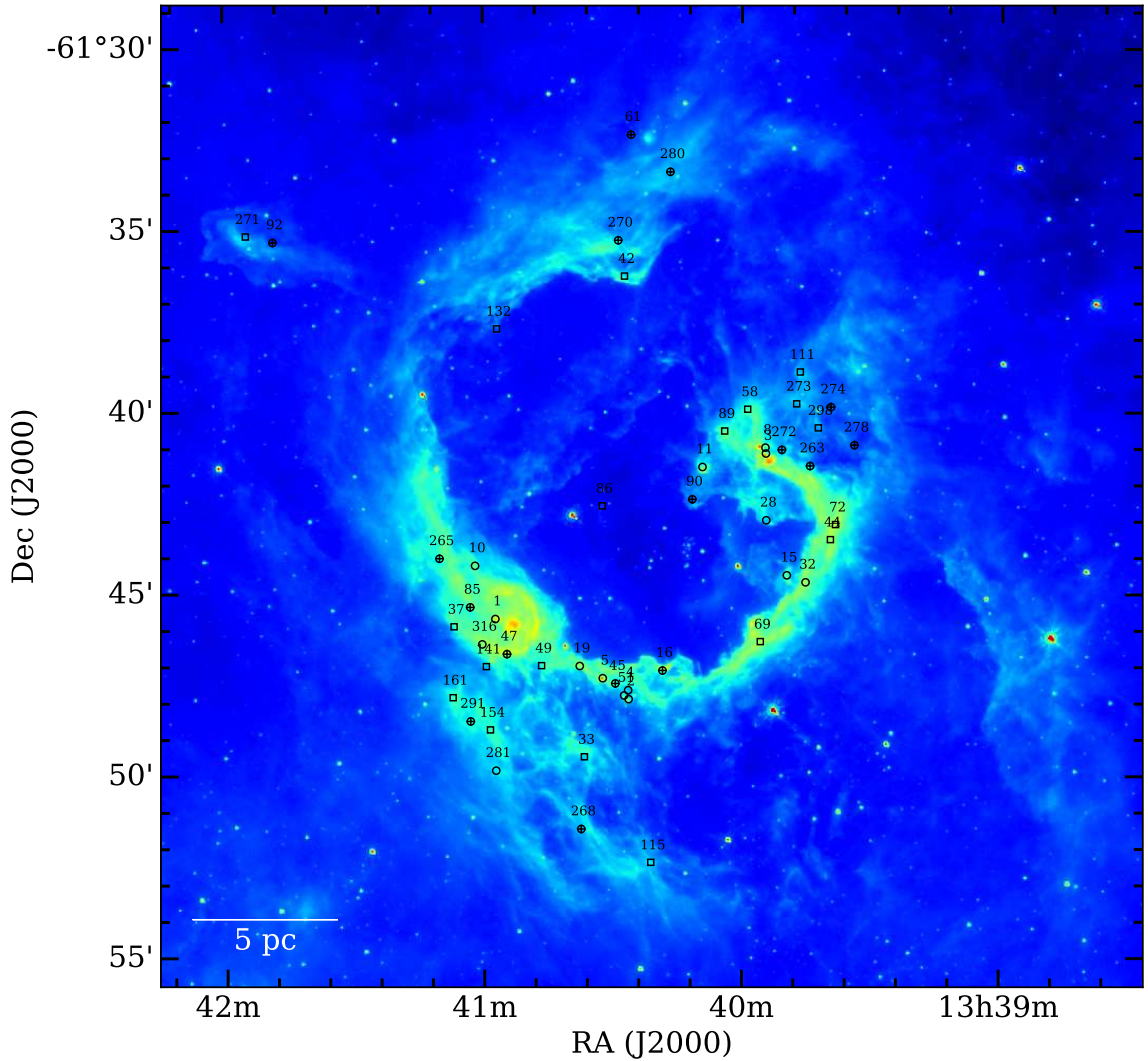


Fig. 12: Fifty compact sources superimposed on the *Spitzer* 8 μm image. Class 0, IM, and I objects (see Sect. 5.1.2) are plotted as plus circles, squares, and circles, respectively.

is a measure of which fraction of molecular gas has been transferred into dense clumps. This quantity is analogous to the SFE and must be treated as an upper limit to the SFE (e.g., Motte et al. 2007; Bontemps et al. 2010b; Eden et al. 2012).

We estimated the CFE as the ratio of the total mass in compact sources to the mass of their hosting condensation. To be consistent with the mass of compact sources derived from *Herschel* data, M_{HOBYS} was adopted as the mass of the condensations. The derived CFEs are given in Table 4 and range from 11 to 76%. The CFE errors mainly arise from the mass uncertainties of the compact sources. Compared with the existing results (5 – 80%, e.g., Motte et al. 1998; Moore et al. 2007; Bontemps et al. 2010b; Eden et al. 2012; Palau et al. 2013; Louvet et al. 2014), the range of 11 to 76% is acceptable.

A trend for an increase in CFE with density has been found in the ρ Ophiuchus (Motte et al. 1998) and Cygnus X clouds (Bontemps et al. 2010b) and has also been confirmed in other star-forming regions (Palau et al. 2013; Louvet et al. 2014). To explore if there is a similar trend in RCW 79, the number densities were approximated as

$n_{\text{H}_2} = M_{\text{HOBYS}} / (4\pi/3 \times R_{\text{min}} \times R_{\text{min}} \times R_{\text{maj}} \times \mu \times m_{\text{H}})$ by assuming a 3D geometry for the condensations, where R_{min} , and R_{maj} are their respective minor and major axes (see Table 4), the mean molecular weight μ is assumed to be 2.8 (Kauffmann et al. 2008), and m_{H} is the mass of a hydrogen atom. The derived densities are listed in Table 4. The relation between the CFE and the density for the condensations is shown in Fig. 13, where the samples from Motte et al. (1998); Bontemps et al. (2010b) are included for comparison. The CFEs of conds. 1 and 2 are the lowest of all the condensations. The low CFE of cond. 1 may be interpreted in terms of its lowest central concentration. According to Johnstone et al. (2000); Könyves et al. (2010), the degree of the central concentration can be simplified by the internal column density contrast of a core, which is defined as the peak over mean column densities of the core. As a result, the internal density contrast of cond. 1 demonstrates that it is least centrally concentrated of the eight condensations. For cond. 2, the lowest CFE could be in part attributed to strong external pressures imposed by the associated CH II region, which may restrain the mass trans-

formation of the condensation into dense cores by the gas dispersal.

Furthermore, an increasing trend of the CFE with density is present for the other six condensations (conds. 3, 4, 5, 6, 7, and 8). This trend is similar to that suggested by Motte et al. (1998) and Bontemps et al. (2010b), demonstrating that the denser the condensation, the higher the fraction of its mass transformation into dense cores. However, the trend in RCW 79 is discontinuous with that found in the ρ Ophiuchus and Cygnus X clouds. It is worth noting that Motte et al. (1998) and Bontemps et al. (2010b) studied the fragmentation of a few 0.1 pc dense cores into ~ 0.01 pc protostellar cores, but we extend the fragmentation on the scale of a few pc condensations into ~ 0.2 pc dense cores due to the limited angular resolution in this paper. These different scales can illustrate the density difference between our condensations and the dense cores studied in Motte et al. (1998) and Bontemps et al. (2010b) (see Fig. 13). Therefore the above discontinuous appearance could be credited to the different physical scales. Despite this discontinuity, the slope of the trend is very similar to that demonstrated in other work (e.g., Motte et al. 1998; Bontemps et al. 2010b; Palau et al. 2013, see Fig. 13). Higher-resolution millimeter observations are clearly needed to study the CFE at smaller scales in the condensations observed around RCW 79 to see how the ionization affects the CFE.

6. Conclusions

Using *Herschel* observations complemented with *Spitzer*, WISE, and 2MASS data, we have explored the early stages of star formation in the Galactic H II region RCW 79. The main results can be summarized as follows:

1. The dust temperature is found to be higher in the direction of the H II region than in the regions away from this region, demonstrating a heating and influence of ionized gas on its vicinity. This influence is further demonstrated by the column density probability distribution function (PDF).
2. The column density PDF consists of two lognormal distributions and a power-law tail. The second lognormal distribution reveals the compression from ionized gas. The slope of the power-law tail indicates the existence of gravitationally bound regions in RCW 79.
3. The most complete sample of 50 reliable compact sources around RCW 79 has been assembled for the first time. They have sizes from 0.1 to 0.4 pc with a typical scale of ~ 0.2 pc, temperatures of $\sim 11 - 26$ K, masses of $\sim 6 - 760 M_{\odot}$, densities of $\sim 0.1 - 44 \times 10^5 \text{ cm}^{-3}$, and bolometric luminosities of $\sim 19 - 12712 L_{\odot}$. The majority (96%) of them are located in the ionization-compressed layer, suggesting that they are exposed to the influence of the H II region. In addition, 44% of the 50 compact sources that are situated in the gravitationally bound regions have a high probability of forming stars.
4. The 50 compact sources have been classified into three classes of objects: 16 class 0, 19 IM, and 15 class I, by a combination of the ratio of $L_{\text{submm}}^{\lambda > 350} / L_{\text{bol}}$ (Bontemps et al. 2010a) with the color classification scheme of Allen et al. (2004). Their distributions in the L-M diagram (Molinari et al. 2008) almost follow the evolutionary

tracks well, indicating that the 50 compact sources are indeed in the early stages of star formation.

5. Twelve massive dense cores (MDCs), candidates of high-mass star precursors, have been tentatively identified by a mass threshold of $140 M_{\odot}$ derived from the L- M_{env} diagram. Their mass surface densities of $\Sigma = \sim 0.4 - 5.1 \text{ g cm}^{-2}$ agree with the existing values observed in several high-mass dense core that may form high-mass stars.
6. The eight massive condensations contain a total of 22 young protostar cores, which is suggestive of active star formation. Their lifetimes, which are much younger than the main H II region, the spatial coincidence of the condensations with the bright PDR emission and the spatial distribution of compact sources located in the ionized-compression layer together indicate that the young protostars are influenced by the H II region in the course of its dynamical evolution. For cond. 2, additional influence from its associated CH II region might have affected its nearby young protostars.
7. An increasing trend of the CFE with density has been found in the condensations of RCW 79, demonstrating that a denser condensation has a higher fraction of gas transformation into dense cores.

Acknowledgements. This work was carried out under the framework of a joint doctoral promotion program between the Chinese Academy of Sciences (CAS) and Centre National de la Recherche Scientifique (CNRS), and has been supported in part by the Center National d'Etudes Spatiales (CNES) and the National Natural Science Foundation of China through the grant 11573036. N.S acknowledges support from the DFG (0s 177/2-1 and 177/2-2), and central funds of the DFG-priority program 1573 (ISM-SPP). We thank P. Tremblin for helpful discussions of the column density probability distribution function, and P. Palmeirim for the discussion of the dynamical age of the compact H II region. SPIRE has been developed by a consortium of institutes led by Cardiff Univ. (UK) with Univ. Lethbridge (Canada); NAOC (China); CEA, LAM (France); IFSI, Univ. Padua (Italy); IAC (Spain); Stockholm Observatory (Sweden); Imperial College London, RAL, UCL-MSSL, UKATC, Univ. Sussex (UK); Caltech, JPL, NHSC, Univ. Colorado (USA). This development has been supported by national funding agencies: CSA (Canada); NAOC (China); CEA, CNES, CNRS (France); ASI (Italy); MCINN (Spain); SNSB (Sweden); STFC (UK); and NASA (USA). PACS has been developed by a consortium of institutes led by MPE (Germany) with UVIE (Austria); KU Leuven, CSL, IMEC (Belgium); CEA, LAM (France); MPIA (Germany); INAF/IFSI/OAA/OAP/OAT, LENS, SISSA (Italy); IAC (Spain). This development has been supported by the funding agencies BMVIT (Austria), ESA-PRODEX (Belgium), CEA/CNES (France), DLR (Germany), ASI/INAF (Italy), and CICYT/MCYT (Spain). We have used the NASA/IPAC Infrared Science Archive to obtain data products from the UKIDSS, *Spitzer*-GLIMPSE, and *Spitzer*-MIPSGAL surveys.

References

- Abergel, A., Arab, H., Compiègne, M., et al. 2010, *A&A*, 518, L96
 Allen, L. E., Calvet, N., D'Alessio, P., et al. 2004, *ApJS*, 154, 363
 Anderson, L. D., Bania, T. M., Balser, D. S., et al. 2014, *ApJS*, 212, 1
 Anderson, L. D., Bania, T. M., Balser, D. S., & Rood, R. T. 2011, *ApJS*, 194, 32
 Anderson, L. D., Deharveng, L., Zavagno, A., et al. 2015, *ApJ*, 800, 101
 André, P., Ward-Thompson, D., & Barsony, M. 1993, *ApJ*, 406, 122
 André, P., Ward-Thompson, D., & Barsony, M. 2000, *Protostars and Planets IV*, 59
 Bally, J., Anderson, L. D., Battersby, C., et al. 2010, *A&A*, 518, L90
 Bania, T. M., Anderson, L. D., Balser, D. S., & Rood, R. T. 2010, *ApJ*, 718, L106
 Beckwith, S. V. W., Sargent, A. I., Chini, R. S., & Guesten, R. 1990, *AJ*, 99, 924

- Benjamin, R. A., Churchwell, E., Babler, B. L., et al. 2003, *PASP*, 115, 953
- Bertoldi, F. 1989, *ApJ*, 346, 735
- Bohlin, R. C., Savage, B. D., & Drake, J. F. 1978, *ApJ*, 224, 132
- Bontemps, S., André, P., Könyves, V., et al. 2010a, *A&A*, 518, L85
- Bontemps, S., Motte, F., Csengeri, T., & Schneider, N. 2010b, *A&A*, 524, A18
- Butler, M. J. & Tan, J. C. 2012, *ApJ*, 754, 5
- Capriotti, E. R. & Kozminski, J. F. 2001, *PASP*, 113, 677
- Carey, S. J., Noriega-Crespo, A., Price, S. D., et al. 2005, in *Bulletin of the American Astronomical Society*, Vol. 37, American Astronomical Society Meeting Abstracts, 1252
- Churchwell, E., Povich, M. S., Allen, D., et al. 2006, *ApJ*, 649, 759
- Churchwell, E., Watson, D. F., Povich, M. S., et al. 2007, *ApJ*, 670, 428
- Csengeri, T., Weiss, A., Wyrowski, F., et al. 2016, *A&A*, 585, A104
- Dale, J. E., Clark, P. C., & Bonnell, I. A. 2007, *MNRAS*, 377, 535
- Dale, J. E., Ercolano, B., & Bonnell, I. A. 2013, *MNRAS*, 431, 1062
- Dale, J. E., Haworth, T. J., & Bressert, E. 2015, *MNRAS*, 450, 1199
- Deharvang, L., Schuller, F., Anderson, L. D., et al. 2010, *A&A*, 523, A6
- Deharvang, L., Zavagno, A., Anderson, L. D., et al. 2012, *A&A*, 546, A74
- Deharvang, L., Zavagno, A., Samal, M. R., et al. 2015, *A&A*, 582, A1
- Deharvang, L., Zavagno, A., Schuller, F., et al. 2009, *A&A*, 496, 177
- Dunham, M. M., Crapsi, A., Evans, II, N. J., et al. 2008, *ApJS*, 179, 249
- Eden, D. J., Moore, T. J. T., Plume, R., & Morgan, L. K. 2012, *MNRAS*, 422, 3178
- Elmegreen, B. G. 2011, in *EAS Publications Series*, Vol. 51, *EAS Publications Series*, ed. C. Charbonnel & T. Montmerle, 45–58
- Elmegreen, B. G. & Lada, C. J. 1977, *ApJ*, 214, 725
- Enoch, M. L., Evans, II, N. J., Sargent, A. I., & Glenn, J. 2009, *ApJ*, 692, 973
- Evans, II, N. J., Dunham, M. M., Jørgensen, J. K., et al. 2009, *ApJS*, 181, 321
- Federrath, C. & Klessen, R. S. 2012, *ApJ*, 761, 156
- Figueira, M., Zavagno, A., Deharvang, L., et al. 2016, *ArXiv e-prints*
- Freyer, T., Hensler, G., & Yorke, H. W. 2003, *ApJ*, 594, 888
- Freyer, T., Hensler, G., & Yorke, H. W. 2006, *ApJ*, 638, 262
- Giannini, T., Elia, D., Lorenzetti, D., et al. 2012, *A&A*, 539, A156
- Girichidis, P., Konstandin, L., Whitworth, A. P., & Klessen, R. S. 2014, *ApJ*, 781, 91
- Griffin, M. J., Abergel, A., Abreu, A., et al. 2010, *A&A*, 518, L3
- Gutermuth, R. A. & Heyer, M. 2015, *AJ*, 149, 64
- Hennemann, M., Motte, F., Bontemps, S., et al. 2010, *A&A*, 518, L84
- Hill, T., André, P., Arzoumanian, D., et al. 2012a, *A&A*, 548, L6
- Hill, T., Motte, F., Didelon, P., et al. 2011, *A&A*, 533, A94
- Hill, T., Motte, F., Didelon, P., et al. 2012b, *A&A*, 542, A114
- Inoue, A. K. 2002, *ApJ*, 570, 688
- Johnstone, D., Wilson, C. D., Moriarty-Schieven, G., et al. 2000, *ApJ*, 545, 327
- Kainulainen, J., Beuther, H., Henning, T., & Plume, R. 2009, *A&A*, 508, L35
- Kauffmann, J., Bertoldi, F., Bourke, T. L., Evans, II, N. J., & Lee, C. W. 2008, *A&A*, 487, 993
- Kendrew, S., Beuther, H., Simpson, R., et al. 2016, *ApJ*, 825, 142
- Kendrew, S., Simpson, R., Bressert, E., et al. 2012, *ApJ*, 755, 71
- Könyves, V., André, P., Men'shchikov, A., et al. 2015, *A&A*, 584, A91
- Könyves, V., André, P., Men'shchikov, A., et al. 2010, *A&A*, 518, L106
- Krumholz, M. R. & Matzner, C. D. 2009, *ApJ*, 703, 1352
- Krumholz, M. R. & McKee, C. F. 2008, *Nature*, 451, 1082
- Lada, C. J. & Lada, E. A. 2003, *ARA&A*, 41, 57
- Lefloch, B. & Lazareff, B. 1994, *A&A*, 289, 559
- Liu, H.-L., Li, J.-Z., Wu, Y., et al. 2016, *ApJ*, 818, 95
- Liu, H.-L., Wu, Y., Li, J., et al. 2015, *ApJ*, 798, 30
- Louvet, F., Motte, F., Hennebelle, P., et al. 2014, *A&A*, 570, A15
- Markwardt, C. B. 2009, in *Astronomical Society of the Pacific Conference Series*, Vol. 411, *Astronomical Data Analysis Software and Systems XVIII*, ed. D. A. Bohlender, D. Durand, & P. Dowler, 251
- Martins, F., Pomarès, M., Deharvang, L., Zavagno, A., & Bouret, J. C. 2010, *A&A*, 510, A32
- McKee, C. F. & Tan, J. C. 2003, *ApJ*, 585, 850
- Men'shchikov, A. 2013, *A&A*, 560, A63
- Men'shchikov, A. 2016, *A&A*, 593, A71
- Men'shchikov, A., André, P., Didelon, P., et al. 2010, *A&A*, 518, L103
- Men'shchikov, A., André, P., Didelon, P., et al. 2012, *A&A*, 542, A81
- Molinari, S., Merello, M., Elia, D., et al. 2016, *ApJ*, 826, L8
- Molinari, S., Pezzuto, S., Cesaroni, R., et al. 2008, *A&A*, 481, 345
- Molinari, S., Swinyard, B., Bally, J., et al. 2010, *A&A*, 518, L100
- Moore, T. J. T., Bretherton, D. E., Fujiyoshi, T., et al. 2007, *MNRAS*, 379, 663
- Motte, F., Andre, P., & Neri, R. 1998, *A&A*, 336, 150
- Motte, F., Bontemps, S., Schilke, P., et al. 2007, *A&A*, 476, 1243
- Motte, F., Zavagno, A., Bontemps, S., et al. 2010, *A&A*, 518, L77
- Mottram, J. C., Hoare, M. G., Lumsden, S. L., et al. 2007, *A&A*, 476, 1019
- Nandakumar, G., Veena, V. S., Vig, S., et al. 2016, *ArXiv e-prints*
- Nguyen Luong, Q., Motte, F., Hennemann, M., et al. 2011, *A&A*, 535, A76
- Ossenkopf-Okada, V., Csengeri, T., Schneider, N., Federrath, C., & Klessen, R. S. 2016, *A&A*, 590, A104
- Paladini, R., Burigana, C., Davies, R. D., et al. 2003, *A&A*, 397, 213
- Palau, A., Fuente, A., Girart, J. M., et al. 2013, *ApJ*, 762, 120
- Parker, Q. A. & Phillipps, S. 1998, *PASA*, 15, 28
- Pavlyuchenkov, Y. N., Kirsanova, M. S., & Wiebe, D. S. 2013, *Astronomy Reports*, 57, 573
- Pilbratt, G. L., Riedinger, J. R., Passvogel, T., et al. 2010, *A&A*, 518, L1
- Poglitsch, A., Waelkens, C., Geis, N., et al. 2010, *A&A*, 518, L2
- Price, S. D., Egan, M. P., Carey, S. J., Mizuno, D. R., & Kuchar, T. A. 2001, *AJ*, 121, 2819
- Rodgers, A. W., Campbell, C. T., & Whiteoak, J. B. 1960, *MNRAS*, 121, 103
- Russel, H. 2012, *Scanamorphos: Maps from scan observations made with bolometer arrays*, *Astrophysics Source Code Library*
- Russeil, D., Schneider, N., Anderson, L. D., et al. 2013, *A&A*, 554, A42
- Russeil, D., Zavagno, A., Motte, F., et al. 2010, *A&A*, 515, A55
- Saito, H., Mizuno, N., Moriguchi, Y., et al. 2001, *PASJ*, 53, 1037
- Samal, M. R., Zavagno, A., Deharvang, L., et al. 2014, *A&A*, 566, A122
- Saraceno, P., Andre, P., Ceccarelli, C., Griffin, M., & Molinari, S. 1996, *A&A*, 309, 827
- Schneider, N., André, P., Könyves, V., et al. 2013, *ApJ*, 766, L17
- Schneider, N., Csengeri, T., Hennemann, M., et al. 2012, *A&A*, 540, L11
- Schneider, N., Csengeri, T., Klessen, R. S., et al. 2015a, *A&A*, 578, A29
- Schneider, N., Ossenkopf, V., Csengeri, T., et al. 2015b, *A&A*, 575, A79
- Schuller, F., Menten, K. M., Contreras, Y., et al. 2009, *A&A*, 504, 415
- Shu, F. H. 1977, *ApJ*, 214, 488
- Simpson, R. J., Povich, M. S., Kendrew, S., et al. 2012, *MNRAS*, 424, 2442
- Skrutskie, M. F., Cutri, R. M., Stiening, R., et al. 2006, *AJ*, 131, 1163
- Tan, J. C., Beltrán, M. T., Caselli, P., et al. 2014, *Protostars and Planets VI*, 149
- Tan, J. C., Kong, S., Butler, M. J., Caselli, P., & Fontani, F. 2013, *ApJ*, 779, 96
- Thompson, M. A., Urquhart, J. S., Moore, T. J. T., & Morgan, L. K. 2012, *MNRAS*, 421, 408
- Traficante, A., Calzoletti, L., Veneziani, M., et al. 2011, *MNRAS*, 416, 2932
- Traficante, A., Fuller, G. A., Peretto, N., Pineda, J. E., & Molinari, S. 2015, *MNRAS*, 451, 3089
- Tremblin, P., Anderson, L. D., Didelon, P., et al. 2014a, *A&A*, 568, A4
- Tremblin, P., Schneider, N., Minier, V., et al. 2014b, *A&A*, 564, A106
- Urquhart, J. S., Busfield, A. L., Hoare, M. G., et al. 2007, *A&A*, 474, 891
- Walch, S., Whitworth, A., Bisbas, T., Wünsch, R., & Hubber, D. 2011, in *IAU Symposium*, Vol. 270, *Computational Star Formation*, ed. J. Alves, B. G. Elmegreen, J. M. Girart, & V. Trimble, 323–326
- Wang, K., Zhang, Q., Testi, L., et al. 2014, *MNRAS*, 439, 3275
- Watson, C., Povich, M. S., Churchwell, E. B., et al. 2008, *ApJ*, 681, 1341
- Whitworth, A. & Summers, D. 1985, *MNRAS*, 214, 1
- Whitworth, A. P., Bhattal, A. S., Chapman, S. J., Disney, M. J., & Turner, J. A. 1994, *MNRAS*, 268, 291
- Wright, E. L., Eisenhardt, P. R. M., Mainzer, A. K., et al. 2010, *AJ*, 140, 1868
- Yadav, R. K., Pandey, A. K., Sharma, S., et al. 2016, *MNRAS*, 461, 2502

- Zavagno, A., Deharveng, L., Comerón, F., et al. 2006, *A&A*, 446, 171
Zavagno, A., Pomarès, M., Deharveng, L., et al. 2007, *A&A*, 472, 835
Zavagno, A., Russeil, D., Motte, F., et al. 2010, *A&A*, 518, L81

Appendix A: Compact sources

A.1. Source extraction

Compact sources were extracted using the algorithm *get-sources* V. 1.140127, a multiscale and multiwavelength source extraction method (Men'shchikov et al. 2010, 2012; Men'shchikov 2013). It works by analyzing decompositions of original images over a broad spectrum of spatial scales and across all wavebands. The wavelength-dependent single-scale detection images are created after subtracting noise and background emission of the corresponding single-scale images. The algorithm then starts to detect compact sources in the combined detection images by tracking the evolution of their segmentation masks across all spatial scales. Photometry of the compact sources is measured in the original background-subtracted image at each wavelength, and the blended sources are deblended in an iterative procedure. The main advantage of this algorithm is that it improves the detection ability for the compact sources, especially in crowded regions, by means of the fine spatial decompositions of original images. Another advantage is that the algorithm designed to automatically combine data over all wavebands successfully averts the difficulty of cross matching independent extraction catalogs at different wavelengths.

In the process of the detection of compact sources, the color-corrected brightness images at 160 and 250 μm were particularly considered to help *getsources* focus on real density peaks instead of those only locally illuminated by external heating, which is an important consideration especially around H II regions. More details can be found in the forthcoming HOBYS consortium paper (Tigé et al. 2016, submitted). Additionally, a column density map with high angular resolution was used to validate the detection of actual density peaks.

A.2. SED fittings

To estimate the dust temperature T_d and envelope mass M_{env} of our sample of 100 candidate compact sources, we have performed SED fittings. Assuming dust emission to be optically thin, we adopted the graybody function for a single temperature to carry out the SED fitting as below.

$$F_\nu = \frac{\kappa_\nu B_\nu(T_d) M_{\text{env}}}{D^2}, \quad (\text{A.1})$$

where F_ν is the observed flux, $B_\nu(T_d)$ is the blackbody function and D is the distance. With T_d and M_{env} treated as free parameters, the SED fitting was performed by invoking the IDL program MPFITFUN (Markwardt 2009).

Before the SED fitting, we scaled the fluxes at different wavelengths as below (Nguyen Luong et al. 2011):

$$F_\lambda^{\text{scaled}} = F_\lambda^{\text{original}} \left(\frac{FWHM_{ref}^{dec}}{FWHM_\lambda^{dec}} \right), \quad (\text{A.2})$$

where $F_\lambda^{\text{scaled}}$ and $F_\lambda^{\text{original}}$ are representatives of respective scaled and original fluxes, and $FWHM_{ref}^{dec}$ and $FWHM_\lambda^{dec}$ represent the deconvolved sizes (see Equation A.3) at the reference wavelength (160 or 250 μm), and other wavelengths, respectively. This flux scaling method works under the assumptions that the source size measured at the reference wavelength is accurate enough, that emission at

all wavelengths is optically thin, and that the flux nearly varies linearly with the source size. More descriptions of the principle of this scaling relation are given in Nguyen Luong et al. (2011). Regarding the reference wavelength, 160 or 250 μm instead of 100 μm were chosen since emission at 100 μm may be more severely affected by external heating especially in H II regions than 160 or 250 μm . For the majority of our samples, the 160 μm is regarded as the reference waveband. However, the 250 μm was also considered for sources whose deconvolved size at 160 μm exceeds that at 250 μm , which is indicative of more extended emission at 160 μm . This extended emission may result from contaminations of small grains heated in PDR regions (Tigé et al. 2016, submitted).

The deconvolved sizes ($FWHM_\lambda^{dec}$) at different wavelengths were approximated as follows:

$$FWHM_\lambda^{dec} = \sqrt{FWHM_\lambda^{obs^2} - HPBW_\lambda^2}, \quad (\text{A.3})$$

where $FWHM_\lambda^{obs}$ is the observed size at each wavelength, and $HPBW_\lambda$ is the beam size. This approximation was not applied when the deconvolved size of a source at a special wavelength was smaller than half the corresponding beam size, which indicates that the source cannot be resolved at this wavelength. We simply assigned to the unresolved source a minimum physical deconvolved size of $FWHM_\lambda^{dec} = 0.5 \times HPBW_\lambda$.

In the SED fitting, photometric color corrections were applied to all *Herschel* bands. The colour correction factors for the PACS wavelengths vary with the dust temperature (Poglitsch et al. 2010). Therefore, we gradually refined the colour correction factors by an iterative SED fitting procedure until a variation of a dust temperature of ≤ 0.01 K. For the SPIRE wavelength bands, their colour correction factors only depend on the dust emissivity spectral index β , fixed to 2 in the fitting. They are 4%, 4%, 5% at 250, 350, and 500 μm (see SPIRE observers' manual), respectively. The scaled and color-corrected fluxes are shown in Table B.2.

Appendix B: Parameters and figures of compact sources

Table B.1: Original fluxes in the *Herschel* bands for the 50 compact sources

ID	$S_{p,70}$ Jy beam ⁻¹	S_{70} Jy	$S_{p,100}$ Jy beam ⁻¹	S_{100} Jy	$S_{p,160}$ Jy beam ⁻¹	S_{160} Jy	$S_{p,250}$ Jy beam ⁻¹	S_{250} Jy	$S_{p,350}$ Jy beam ⁻¹	S_{350} Jy	$S_{p,500}$ Jy beam ⁻¹	S_{500} Jy
1	79.7 ± 1.6	149.6 ± 2.2	98.4 ± 2.2	227.8 ± 5.5	118.7 ± 3.0	188.1 ± 4.0	94.5 ± 4.4	92.3 ± 3.9	39.6 ± 2.4	38.3 ± 2.2	15.8 ± 1.0	19.4 ± 1.6
2	13.0 ± 0.3	23.2 ± 0.4	24.2 ± 0.3	32.7 ± 0.5	28.8 ± 1.2	42.0 ± 2.0	20.9 ± 0.6	25.2 ± 0.6	14.3 ± 1.0	14.6 ± 0.9	5.2 ± 0.6	5.8 ± 0.5
3	26.4 ± 0.9	95.8 ± 1.5	50.7 ± 0.3	303.2 ± 1.3	87.3 ± 2.6	199.9 ± 4.0	89.8 ± 1.1	96.6 ± 0.9	39.6 ± 1.4	40.0 ± 1.2	8.5 ± 1.0	8.2 ± 1.0
4	7.1 ± 0.6	10.4 ± 0.6	15.0 ± 0.5	17.9 ± 0.6	22.3 ± 1.3	32.6 ± 1.3	24.8 ± 0.6	28.3 ± 0.5	11.9 ± 1.0	12.0 ± 1.0	8.9 ± 0.6	9.3 ± 0.5
5	11.2 ± 0.5	20.6 ± 0.7	12.6 ± 0.6	20.7 ± 0.7	14.9 ± 1.1	29.8 ± 2.2	10.7 ± 0.9	10.4 ± 0.8	4.7 ± 1.2	6.1 ± 1.1	3.6 ± 0.8	3.6 ± 0.7
8	0.0 ± 1.2	0.4 ± 1.4	11.5 ± 2.2	47.8 ± 3.2	43.6 ± 2.9	58.1 ± 2.9	50.0 ± 0.9	55.1 ± 0.8	33.9 ± 1.3	35.4 ± 1.2	17.9 ± 1.1	18.3 ± 1.0
10	3.2 ± 0.2	5.6 ± 0.2	5.5 ± 0.3	9.3 ± 0.4	8.6 ± 0.9	10.1 ± 0.9	5.8 ± 1.2	4.2 ± 1.4	2.4 ± 1.2	2.1 ± 1.2	0.0 ± 0.4	0.0 ± 0.4
11	5.0 ± 0.1	32.3 ± 0.2	7.0 ± 0.2	50.2 ± 0.5	17.1 ± 0.4	42.8 ± 0.6	16.5 ± 0.6	19.3 ± 0.6	8.9 ± 1.1	9.3 ± 1.2	3.1 ± 0.5	3.3 ± 1.3
15	3.4 ± 0.2	7.9 ± 0.2	5.8 ± 0.2	13.3 ± 0.3	8.6 ± 0.4	10.4 ± 0.4	6.8 ± 0.3	5.8 ± 0.3	2.9 ± 0.3	2.2 ± 0.3	1.4 ± 0.5	1.6 ± 0.4
16	3.4 ± 0.4	16.4 ± 0.7	4.3 ± 0.4	24.8 ± 0.8	16.3 ± 1.0	37.5 ± 1.2	25.6 ± 0.5	31.4 ± 0.4	14.7 ± 0.6	21.8 ± 1.3	7.5 ± 0.5	10.4 ± 0.7
19	2.7 ± 0.3	10.7 ± 0.4	4.3 ± 0.3	17.6 ± 0.5	12.2 ± 1.5	26.1 ± 1.9	14.6 ± 1.8	15.7 ± 1.6	10.1 ± 1.2	11.0 ± 1.1	5.2 ± 0.9	5.1 ± 0.8
28	1.1 ± 0.1	5.7 ± 0.1	2.1 ± 0.1	9.9 ± 0.2	5.6 ± 0.9	12.9 ± 1.1	6.8 ± 0.6	7.5 ± 0.6	2.9 ± 0.8	2.9 ± 0.7	1.9 ± 0.7	2.1 ± 0.6
32	2.1 ± 0.2	8.0 ± 0.3	3.4 ± 0.2	16.6 ± 0.4	5.5 ± 0.4	10.9 ± 0.4	3.8 ± 0.5	3.9 ± 0.4	1.8 ± 0.3	2.4 ± 0.4	1.7 ± 0.5	3.2 ± 0.6
33	0.8 ± 0.1	17.5 ± 0.4	1.5 ± 0.1	28.0 ± 0.5	6.2 ± 0.5	32.9 ± 1.1	7.9 ± 0.7	13.1 ± 0.8	5.2 ± 0.8	7.1 ± 0.8	2.6 ± 0.7	2.9 ± 0.6
37	0.6 ± 0.3	1.8 ± 0.4	1.3 ± 0.4	7.7 ± 0.9	5.5 ± 2.0	10.1 ± 2.9	8.3 ± 2.8	7.2 ± 2.4	3.0 ± 1.5	2.9 ± 1.6	1.0 ± 0.4	0.8 ± 0.3
42	1.6 ± 0.1	14.1 ± 0.2	3.1 ± 0.2	26.2 ± 0.6	10.1 ± 0.4	30.0 ± 1.1	9.6 ± 0.8	12.3 ± 0.8	7.3 ± 0.7	7.9 ± 0.6	3.2 ± 0.6	4.2 ± 1.0
44	2.0 ± 0.2	10.8 ± 0.4	2.9 ± 0.2	18.2 ± 0.7	6.6 ± 0.6	21.7 ± 1.0	4.8 ± 0.7	5.3 ± 0.7	3.3 ± 0.9	3.4 ± 0.9	1.5 ± 0.7	2.0 ± 0.6
45	0.6 ± 0.5	1.3 ± 0.6	1.6 ± 0.4	2.8 ± 0.5	11.3 ± 1.3	21.5 ± 1.3	22.4 ± 0.7	27.6 ± 0.6	15.4 ± 1.2	19.5 ± 1.1	9.2 ± 0.6	9.2 ± 0.6
47	2.6 ± 1.7	11.4 ± 2.8	5.4 ± 2.0	34.2 ± 3.8	12.7 ± 3.4	39.3 ± 4.7	18.6 ± 3.7	23.9 ± 3.4	11.1 ± 2.2	12.5 ± 2.0	9.6 ± 1.0	14.6 ± 0.9
49	0.0 ± 0.2	0.8 ± 0.3	0.5 ± 0.3	3.3 ± 0.5	5.2 ± 1.5	8.8 ± 1.8	7.1 ± 2.8	5.1 ± 2.5	4.8 ± 1.4	5.1 ± 1.3	4.7 ± 1.0	6.0 ± 0.9
51	0.8 ± 0.2	0.4 ± 0.2	5.0 ± 0.4	5.5 ± 0.4	11.8 ± 1.2	15.2 ± 1.2	14.1 ± 0.6	14.8 ± 0.6	7.3 ± 1.1	7.0 ± 1.0	3.9 ± 0.6	3.9 ± 0.5
58	1.4 ± 0.1	8.0 ± 0.1	2.1 ± 0.2	8.4 ± 0.4	4.0 ± 0.4	9.6 ± 0.6	3.9 ± 0.5	5.1 ± 0.4	1.4 ± 0.4	1.4 ± 0.7	1.5 ± 0.8	2.3 ± 0.7
61	0.1 ± 0.0	0.3 ± 0.1	0.3 ± 0.1	0.9 ± 0.1	2.9 ± 0.5	5.7 ± 0.6	10.3 ± 0.8	21.0 ± 1.6	9.3 ± 0.7	11.9 ± 0.7	6.9 ± 0.7	8.1 ± 0.7
69	1.4 ± 0.4	9.9 ± 0.9	1.9 ± 0.5	17.4 ± 1.1	5.3 ± 0.6	20.6 ± 0.8	6.3 ± 0.5	9.4 ± 0.5	3.8 ± 0.4	5.3 ± 0.4	1.9 ± 0.3	2.7 ± 0.3
72	1.7 ± 0.2	9.3 ± 0.3	2.0 ± 0.2	16.6 ± 0.5	5.5 ± 0.8	16.6 ± 1.1	4.5 ± 1.0	6.3 ± 0.9	2.5 ± 0.9	3.1 ± 0.8	0.8 ± 0.7	1.0 ± 0.6
85	0.1 ± 0.3	0.6 ± 0.4	0.9 ± 0.4	5.8 ± 0.9	7.3 ± 1.9	12.4 ± 2.7	14.2 ± 3.2	14.1 ± 2.8	8.5 ± 1.8	8.0 ± 1.6	5.0 ± 0.9	6.5 ± 1.0
86	0.4 ± 0.0	1.5 ± 0.1	0.6 ± 0.1	2.4 ± 0.1	2.7 ± 0.1	4.8 ± 0.1	2.5 ± 0.2	2.4 ± 0.1	1.3 ± 0.1	1.1 ± 0.1	0.5 ± 0.1	0.4 ± 0.1
89	1.3 ± 0.2	5.2 ± 0.5	1.7 ± 0.2	11.8 ± 0.5	4.1 ± 0.4	12.5 ± 0.6	3.6 ± 0.6	5.5 ± 0.6	2.5 ± 0.5	6.3 ± 0.9	2.5 ± 0.8	3.1 ± 0.7
90	0.2 ± 0.1	1.9 ± 0.1	1.0 ± 0.2	8.2 ± 0.5	5.7 ± 0.3	17.5 ± 0.5	10.9 ± 0.5	12.6 ± 0.6	6.6 ± 0.5	6.6 ± 0.5	2.9 ± 0.4	2.4 ± 0.7
92	0.1 ± 0.1	0.3 ± 0.1	0.2 ± 0.1	1.3 ± 0.2	2.1 ± 0.3	5.5 ± 0.5	3.6 ± 0.5	4.6 ± 0.4	2.2 ± 0.3	2.7 ± 0.3	1.5 ± 0.2	1.6 ± 0.2
111	0.4 ± 0.0	2.2 ± 0.1	0.8 ± 0.1	2.7 ± 0.1	2.3 ± 0.2	3.9 ± 0.3	2.2 ± 0.4	2.4 ± 0.3	1.4 ± 0.4	1.4 ± 0.4	0.6 ± 0.5	0.6 ± 0.4
115	0.3 ± 0.1	0.9 ± 0.1	0.6 ± 0.2	1.5 ± 0.3	1.6 ± 0.6	2.7 ± 0.6	1.9 ± 0.6	2.3 ± 0.5	0.8 ± 0.4	0.8 ± 0.4	0.3 ± 0.3	0.0 ± 0.3
132	0.1 ± 0.0	0.4 ± 0.0	0.6 ± 0.1	1.8 ± 0.1	1.8 ± 0.2	2.6 ± 0.2	2.1 ± 0.4	2.2 ± 0.4	1.3 ± 0.5	1.4 ± 0.4	0.5 ± 0.3	0.6 ± 0.2
141	0.3 ± 0.1	3.5 ± 0.2	8.0 ± 0.8	8.0 ± 0.8	11.1 ± 2.2	0.2 ± 0.3	7.6 ± 0.8	0.2 ± 0.2	2.0 ± 0.2	2.0 ± 0.2	0.0 ± 0.3	1.5 ± 0.2
154	0.9 ± 0.2	8.1 ± 0.4	1.3 ± 0.2	11.5 ± 0.5	3.5 ± 0.5	14.1 ± 0.9	3.9 ± 0.6	5.9 ± 0.6	2.1 ± 0.9	2.4 ± 0.8	1.0 ± 0.4	1.1 ± 0.4
161	0.5 ± 0.1	6.9 ± 0.3	0.8 ± 0.1	9.9 ± 0.3	2.6 ± 0.4	12.6 ± 0.8	3.2 ± 1.0	6.1 ± 1.0	1.6 ± 1.0	2.8 ± 0.9	0.8 ± 0.4	1.1 ± 0.3
263	0.3 ± 0.2	3.9 ± 0.7	0.5 ± 0.2	13.9 ± 1.0	3.3 ± 1.6	9.7 ± 2.8	15.6 ± 1.0	23.6 ± 1.4	9.9 ± 0.9	12.1 ± 1.1	7.7 ± 0.8	9.7 ± 0.7
265	0.0 ± 0.1	0.4 ± 0.1	0.1 ± 0.1	1.7 ± 0.4	3.5 ± 0.6	8.7 ± 0.9	5.9 ± 1.0	6.8 ± 0.9	4.5 ± 1.2	4.4 ± 1.1	2.5 ± 0.4	3.8 ± 0.4
268		2.0 ± 0.1	0.2 ± 0.1	3.0 ± 0.2	2.3 ± 0.4	6.1 ± 0.6	4.6 ± 0.5	6.8 ± 0.7	3.1 ± 0.5	3.4 ± 0.4	1.6 ± 0.4	1.3 ± 0.4
270	0.1 ± 0.0		0.3 ± 0.1	5.4 ± 0.3	2.9 ± 0.2	27.4 ± 0.6	7.6 ± 0.9	20.6 ± 1.5	6.0 ± 0.8	10.6 ± 1.0	4.5 ± 0.8	5.9 ± 0.8
271	0.6 ± 0.0	7.6 ± 0.2	0.9 ± 0.1	10.9 ± 0.2	2.8 ± 0.2	14.5 ± 0.5	3.2 ± 0.4	9.0 ± 0.5	2.0 ± 0.3	2.8 ± 0.3	1.2 ± 0.2	1.4 ± 0.2
272				4.4 ± 0.5	0.0 ± 1.2	0.0 ± 1.2	22.2 ± 1.2	23.3 ± 1.0	12.3 ± 1.2	12.9 ± 1.1	9.2 ± 0.9	8.9 ± 0.9
273	0.3 ± 0.2	3.9 ± 0.6	0.6 ± 0.2	8.8 ± 0.5	2.3 ± 0.4	8.6 ± 0.8	3.3 ± 0.4	4.9 ± 0.6	1.7 ± 0.7	1.8 ± 0.7	0.7 ± 0.4	0.7 ± 0.4
274	0.0 ± 0.0	1.4 ± 0.1	0.1 ± 0.0	1.3 ± 0.1	0.9 ± 0.2	2.3 ± 0.3	2.5 ± 0.4	3.3 ± 0.4	1.7 ± 0.4	1.6 ± 0.4	0.6 ± 0.4	0.2 ± 0.3
278	0.0 ± 0.1	0.0 ± 0.1	0.3 ± 0.1	0.5 ± 0.1	1.2 ± 0.4	1.3 ± 0.4	1.7 ± 0.6	1.7 ± 0.5	1.2 ± 0.6	2.1 ± 0.5	1.1 ± 0.4	1.1 ± 0.3
280	0.1 ± 0.0	4.3 ± 0.1	0.3 ± 0.1	6.7 ± 0.2	1.8 ± 0.6	17.4 ± 1.6	3.4 ± 0.7	8.8 ± 1.4	2.6 ± 0.7	4.4 ± 1.1	2.4 ± 0.6	4.7 ± 0.8
281	0.2 ± 0.1	0.4 ± 0.1	0.3 ± 0.1	0.7 ± 0.1	1.8 ± 0.5	4.8 ± 0.9	2.1 ± 0.4	2.5 ± 0.3	1.5 ± 0.5	1.7 ± 0.5	1.0 ± 0.3	1.0 ± 0.3
291	0.0 ± 0.1	0.1 ± 0.1	0.3 ± 0.0	2.5 ± 0.1	1.3 ± 0.5	3.1 ± 0.6	2.7 ± 0.7	4.1 ± 0.6	2.2 ± 1.0	3.2 ± 0.9	1.2 ± 0.4	1.2 ± 0.4
298	0.3 ± 0.1	1.9 ± 0.3	0.4 ± 0.1	3.1 ± 0.4	1.4 ± 0.4	5.8 ± 0.7	1.9 ± 0.6	2.8 ± 0.7	1.0 ± 0.6	1.0 ± 0.5	0.2 ± 0.3	0.1 ± 0.3
316	0.3 ± 0.1	3.5 ± 0.2		57.1 ± 5.7		44.1 ± 8.8	0.2 ± 0.3	17.8 ± 1.8	0.2 ± 0.2	6.3 ± 0.6	0.0 ± 0.3	2.2 ± 0.2

Table B.2: Size-scaled and color-corrected fluxes in the *Herschel* bands

ID	S_{100} Jy	S_{160} Jy	S_{250} Jy	S_{350} Jy	S_{500} Jy
1	233.9 ± 9.0	187.5 ± 10.2	86.8 ± 5.7	36.1 ± 3.2	18.5 ± 2.0
2	33.5 ± 1.1	43.1 ± 3.0	23.7 ± 1.3	13.7 ± 1.3	5.5 ± 0.6
3	227.0 ± 6.9	199.3 ± 10.7	90.8 ± 4.6	37.7 ± 2.9	7.8 ± 1.1
4	17.9 ± 0.8	34.0 ± 2.2	26.6 ± 1.4	11.3 ± 1.2	8.9 ± 0.8
5	21.2 ± 1.0	30.0 ± 2.7	9.8 ± 0.9	2.4 ± 1.1	3.5 ± 0.7
8	47.7 ± 3.5	60.5 ± 4.3	51.8 ± 2.7	33.4 ± 2.6	17.4 ± 1.5
10	9.5 ± 0.5	10.1 ± 1.0	4.0 ± 1.3		
11	51.5 ± 1.6	42.5 ± 2.2	18.1 ± 1.1	8.7 ± 1.2	3.1 ± 1.2
15	13.7 ± 0.5	10.4 ± 0.6	5.5 ± 0.4	2.1 ± 0.3	1.6 ± 0.4
16	25.0 ± 1.1	38.9 ± 2.3	29.5 ± 1.5	20.6 ± 1.9	9.9 ± 1.0
19		27.2 ± 2.4	14.8 ± 1.7	10.4 ± 1.3	4.9 ± 0.9
28	10.1 ± 0.4	13.1 ± 1.3	7.1 ± 0.7	2.7 ± 0.7	2.0 ± 0.6
32	12.5 ± 0.6	10.7 ± 0.7	3.7 ± 0.4	1.2 ± 0.3	0.8 ± 0.6
33	14.6 ± 0.7	22.4 ± 1.6	12.3 ± 1.0	6.2 ± 0.9	2.8 ± 0.6
37	4.0 ± 0.9	10.5 ± 3.1	6.8 ± 2.3		
42	17.6 ± 0.8	26.0 ± 1.7	11.5 ± 0.9	7.5 ± 0.8	4.0 ± 1.0
44	18.7 ± 0.9	21.8 ± 1.5	5.0 ± 0.7	3.2 ± 0.8	1.9 ± 0.6
45	3.4 ± 0.5	22.4 ± 1.7	25.9 ± 1.4	12.2 ± 1.3	8.8 ± 0.8
47		30.6 ± 5.1	22.5 ± 3.4	11.8 ± 2.1	5.3 ± 0.9
49		9.1 ± 0.9	4.8 ± 0.5	2.0 ± 0.2	5.7 ± 0.6
51	5.5 ± 0.4	16.0 ± 1.5	13.9 ± 0.9	6.6 ± 1.1	3.8 ± 0.6
58	8.7 ± 0.5	9.7 ± 0.8	4.8 ± 0.5	1.4 ± 0.7	
61		5.6 ± 0.7	19.8 ± 1.8	11.3 ± 1.0	7.7 ± 0.9
69	9.6 ± 1.1	12.4 ± 1.1	8.8 ± 0.6	3.2 ± 0.4	1.1 ± 0.3
72	17.0 ± 0.8	16.5 ± 1.4	6.0 ± 0.9	2.9 ± 0.8	
85	5.7 ± 0.9	13.1 ± 2.9	13.3 ± 2.7	7.5 ± 1.6	6.2 ± 1.0
86		4.8 ± 0.3	2.3 ± 0.2	1.1 ± 0.1	
89	10.8 ± 0.6	10.9 ± 0.8	5.1 ± 0.6	2.4 ± 0.8	1.9 ± 0.7
90	8.3 ± 0.5	18.1 ± 1.0	11.8 ± 0.8	6.2 ± 0.6	2.3 ± 0.7
92		5.8 ± 0.6	4.3 ± 0.5	2.5 ± 0.3	1.6 ± 0.2
111	2.1 ± 0.1	4.1 ± 0.4	2.3 ± 0.3	0.7 ± 0.3	
115	1.6 ± 0.3	2.8 ± 0.7	1.3 ± 0.5	0.7 ± 0.3	
132		2.7 ± 0.2	2.0 ± 0.4	0.5 ± 0.4	
141	8.0 ± 0.8	11.1 ± 2.2	7.6 ± 0.8	2.0 ± 0.2	1.5 ± 0.2
154	8.5 ± 0.6	11.1 ± 1.1	5.6 ± 0.6	1.9 ± 0.8	1.0 ± 0.4
161	7.0 ± 0.4	10.2 ± 0.9	5.7 ± 1.0		0.6 ± 0.3
263			22.2 ± 1.7	11.4 ± 1.3	6.3 ± 0.8
265		8.6 ± 1.1	6.4 ± 0.9	4.2 ± 1.0	1.4 ± 0.4
268		6.5 ± 0.7	6.4 ± 0.7	3.2 ± 0.5	1.2 ± 0.4
270			19.4 ± 1.7	10.8 ± 1.2	5.6 ± 0.9
271	10.6 ± 0.4	14.9 ± 0.9	7.5 ± 0.6	3.8 ± 0.4	1.3 ± 0.2
272			21.9 ± 1.5	12.2 ± 1.3	8.5 ± 1.0
273	9.0 ± 0.6	8.6 ± 0.9	4.6 ± 0.6	1.7 ± 0.7	
274		2.5 ± 0.3	3.1 ± 0.4	1.5 ± 0.4	
278	0.5 ± 0.1	1.4 ± 0.4	1.6 ± 0.5		
280			8.3 ± 1.4	4.3 ± 1.1	2.3 ± 0.8
281		4.5 ± 0.9	2.4 ± 0.3	1.0 ± 0.4	
291		2.5 ± 0.6	3.9 ± 0.6	2.8 ± 0.8	
298	3.2 ± 0.4	6.0 ± 0.8	2.6 ± 0.7		
316	57.1 ± 5.7	44.1 ± 8.8	17.8 ± 1.8	6.3 ± 0.6	2.2 ± 0.2

Table B.3: Observed properties of compact sources

ID	Photometries ^a	IR Counterpart ^b	Blended Source	Hosting Condensation ^c	Class ^d	Comments ^e
1	(100,160,250,350,500) μm	(3.6,4.5,5.8,8.0,12,24,70) μm	no	cond-2	I	91C2, class I, high-mass YSO
2	(100,160,250,350,500) μm	(2.17,3.6,4.5,5.8,8.0,12,24,70) μm	51	cond-3	IM	3C3, class I
3	(100,160,250,350,500) μm	(3.6,4.5,5.8,8.0,24,70) μm	8	cond-4	I	2C4, class I
4	(100,160,250,350,500) μm	(1.25,1.65,2.17,3.6,4.5,5.8,8.0,24,70) μm	no	cond-3	IM	class I
5	(100,160,250,350,500) μm	(1.25,1.65,2.17,3.6,4.5,5.8,8.0,12,24,70) μm	2,51	cond-3	I	2C3, class I
8	(100,160,250,350,500) μm	(3.6,4.5,5.8,8.0) μm	3	cond-4	IM	3C4, class I
10	(100,160,250) μm	(3.6,4.5,5.8,8.0,12,24,70) μm	no	cond-1	I	237C2, class I, high-mass YSO
11	(100,160,250,350,500) μm	(1.25,1.65,2.17,3.6,4.5,5.8,8.0,70) μm	no	cond-9	I	class I
15	(100,160,250,350,500) μm	Filaments at [3.6,4.5,5.8,8.0,12,24,70] μm	no	SW	I	I
16	[100](160,250,350,500) μm	Filaments at [3.6,4.5,5.8,8.0,12,24,70] μm	no	cond-3	0	class 0
19	(160,250,350,500) μm	(3.6,4.5,5.8,8.0,24) μm	no	cond-3	IM	1C3, class I
28	(100,160,250,350,500) μm	(1.65,2.17,3.6,4.5) μm	no	cond4below	I	class I
32	(100,160,250,350,500) μm	Filaments at [3.6,4.5,5.8,8.0,12,24,70] μm	no	SW	I	class I
33	[100](160,250,350,500) μm	[8.0,12,24,70] μm	no	cond2below	IM	IM
37	(100,160,250) μm	[5.8,8.0,12,24,70] μm	no	cond-2	IM	IM
42	(100,160,250,350,500) μm	[5.8,8.0,12,24,70] μm	no	cond-5	IM	IM
44	(100,160,250,350,500) μm	Filaments at [3.6,4.5,5.8,8.0,12,24,70] μm	no	SW	IM	IM
45	(100,160,250,350,500) μm	[5.8,8.0] μm	no	cond-3	0	class 0
47	(160,250,350,500) μm	[5.8,8.0,12,24,70] μm	no	cond-2	0	class 0
49	(160,250,350,500) μm	[5.8,8.0,12,24,70] μm	no	cond-2	IM	IM
51	(100,160,250,350,500) μm	(2.17,3.6,4.5,5.8,8.0) μm	2,4	cond-3	0	5C3, class I
58	(100,160,250,350) μm	[5.8,8.0,12,24,70] μm	no	cond-4	IM	IM
61	[160](250,350,500) μm	Absorption at [5.8,8.0,12] μm	no	cond-8	0	class 0
69	(100,160,250,350,500) μm	Filaments at [3.6,4.5,5.8,8.0,12,24,70] μm	no	SW	IM	IM
72	(100,160,250,350) μm	Filaments at [3.6,4.5,5.8,8.0,12,24,70] μm	no	SW	IM	IM
85	(100,160,250,350,500) μm	[3.6,4.5,5.8,8.0,12,24] μm	no	cond-2	0	class 0
86	(100,160,250,350,500) μm	[3.6,4.5,5.8,8.0,70] μm	no	Center	IM	IM
89	(100,160,250,350,500) μm	[5.8,8.0,12,24,70] μm	95	cond-4	IM	IM
90	[100](160,250,350,500) μm	Absorption at [8,12,24] μm	no	cond-7	0	class 0
92	(160,250,350,500) μm	Absorption at [8,12,24] μm	no	NE	0	class 0
111	(100,160,250,350,500) μm	[5.8,8.0,12,24,70] μm	no	cond-4	IM	IM
115	(100,160,250,350) μm	[5.8,8.0,12,24,70] μm	no	cond3below	IM	IM
132	(160,250,350) μm	[12,24,70] μm	no	NE	IM	IM
141	(160,250,350,500) μm	Absorption at [8.0] μm	no	cond-2	IM	AC2, class I
154	(100,160,250,350,500) μm	Filaments at [5.8,8.0,12,24,70] μm	no	cond2below	IM	IM
161	[100](160,250,500) μm	Filaments at [5.8,8.0,12,24,70] μm	no	cond2below	IM	IM
263	(250,350,500) μm	Absorption at [8.0,12,24] μm	no	cond-4	0	class 0
265	(160,250,350,500) μm	Absorption at [8.0,12,24] μm	no	cond-1	0	class 0
268	(160,250,350,500) μm	Absorption at [8.0,12,24] μm	no	cond3below	0	class 0
270	(250,350,500) μm	Absorption at [8.0,12,24,70] μm	no	cond-5	0	class 0
271	(100,160,250,350,500) μm	[8.0,12,24,70] μm	no	NE	IM	IM
272	(250,350,500) μm	Absorption at [8.0,12,24,70] μm	no	cond-4	0	class 0
273	(100,160,250,350) μm	[8.0,12,24,70] μm	no	cond-4	IM	IM
274	(160,250,350) μm	Absorption at [8.0,12,24,70] μm	no	cond-4	0	class 0
278	(100,160,250) μm	Absorption at [8.0,12,24,70] μm	no	cond-4	0	class 0
280	(250,350,500) μm	Absorption at [8.0,12,24,70] μm	no	cond-9	0	class 0
281	(160,250,350) μm	[8.0,12,24,70] μm	no	cond2below	I	class I
291	(160,250,350) μm	[5.8,8.0,12,24,70] μm	no	cond-2	0	class 0
298	(100,160,250) μm	[5.8,8.0,12,24,70] μm	no	cond-4	IM	IM
316	[100](160,250,350,500) μm	[5.8,8.0,12,24,70] μm	no	cond-2	I	class I

Notes.

^a Parenthesis and bracket denote the good and poor photometries at the corresponding wavelength, respectively. The criteria of the good photometry are explained in Sect. 4.3.3.

^b Parenthesis and bracket represent the point-like and extended-structure sources, respectively.

^c Condensations follow the identification number given by ZA06.

^d Class notes the three classes of sources categorized by the ratio between submillimeter and bolometric luminosities.

^e The final classification is determined by a combination of the ratio as mentioned in (b) and their IR colors (see Sect. 5.1.2.)

Table B.4: Photometries in the NIR and MIR bands for 11 compact sources

ID	Designation	J mJy	H mJy	K_s mJy	I_1 mJy	I_2 mJy	I_3 mJy	I_4 mJy	12 μm mJy	24 μm mJy
1	G308.7543+00.5486				20.4 \pm 0.8	107.7 \pm 13.8	156.7 \pm 8.6	210.0 \pm 9.3	353.5 \pm 7.4	6959.4 \pm 57.3
2	G308.6874+00.5240			6.2 \pm 0.3	57.9 \pm 10.0	278.6 \pm 17.7	532.4 \pm 17.1	487.6 \pm 16.6	74.5 \pm 2.5	1272.5 \pm 26.4
3	G308.6467+00.6458				9.7 \pm 3.0	23.2 \pm 3.8	178.6 \pm 19.6	456.8 \pm 67.7		946.0 \pm 23.6
4	G308.6884+00.5279	1.0 \pm 0.5	6.1 \pm 1.9	3.8 \pm 0.3	5.0 \pm 0.7	12.6 \pm 1.6	16.8 \pm 1.0	27.2 \pm 2.6		242.2 \pm 10.0
5	G308.7009+00.5315	3.7 \pm 0.1	7.8 \pm 0.3	12.5 \pm 0.4	43.0 \pm 13.8	43.5 \pm 4.6	259.0 \pm 12.8	668.2 \pm 36.3	680.0 \pm 8.0	6633.2 \pm 56.8
8	G308.6465+00.6503				20.1 \pm 1.6	49.1 \pm 3.6	95.4 \pm 3.9	129.5 \pm 7.5		
10	G308.7681+00.5706				11.0 \pm 0.7	45.0 \pm 2.3	112.7 \pm 4.1	162.3 \pm 9.0	42.2 \pm 1.8	759.4 \pm 14.4
11	G308.6729+00.6335	6.5 \pm 0.8	16.7 \pm 0.8	51.0 \pm 1.6	86.5 \pm 9.2	95.3 \pm 8.1	128.8 \pm 11.8	178.8 \pm 25.8		
19	G308.7129+00.5349				34.5 \pm 2.9	65.5 \pm 3.4	114.2 \pm 7.5	122.0 \pm 27.8		168.9 \pm 6.1
28			1.3 \pm 1.8	3.5 \pm 3.3	1.6 \pm 0.1	1.3 \pm 0.1				
51	G308.6895+00.5253			3.7 \pm 0.3	31.4 \pm 3.5	78.0 \pm 6.4	134.9 \pm 9.0	140.6 \pm 7.2		

Notes. The fluxes for source 28 are obtained by aperture photometry.

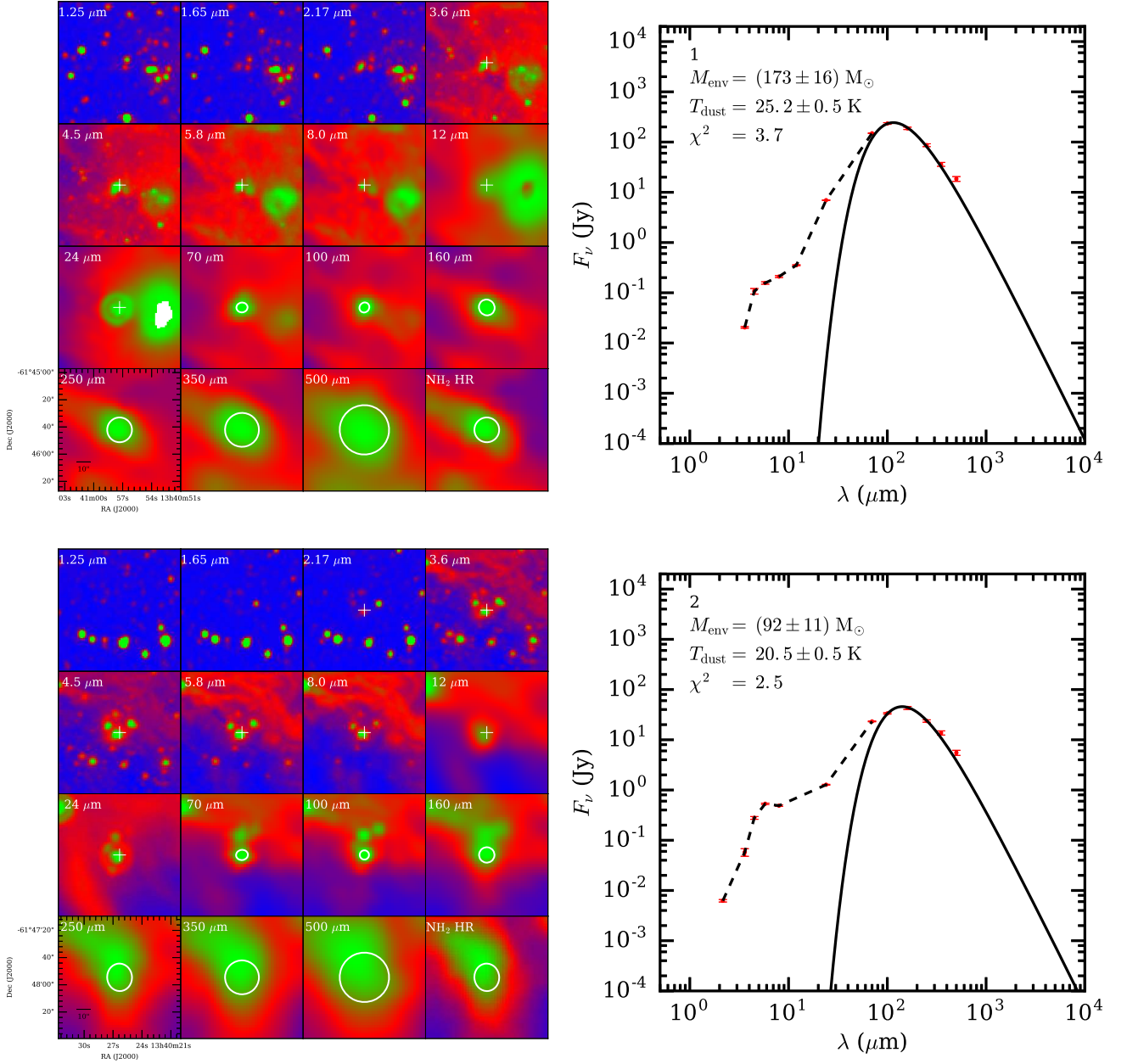


Fig. B.1: (Left) plot consisting of multiwavelength images from 1.25 to 500 μm along with the $18''.2$ resolution column density map. All images are resampled to the same pixel size ($2''$) for a better display effect. The coordinates of compact sources with IR point counterparts are shown in the cross and the photometry apertures in the *Herschel* bands are marked in the ellipse. (Right) SED fitting plot. The filled circle symbolizes the flux at each wavelength available to each source. The solid line indicates the graybody fitting to the available fluxes at 100 to 500 μm and the dashed line is the connecting line among the available IR fluxes at 1.25 to 70 μm .

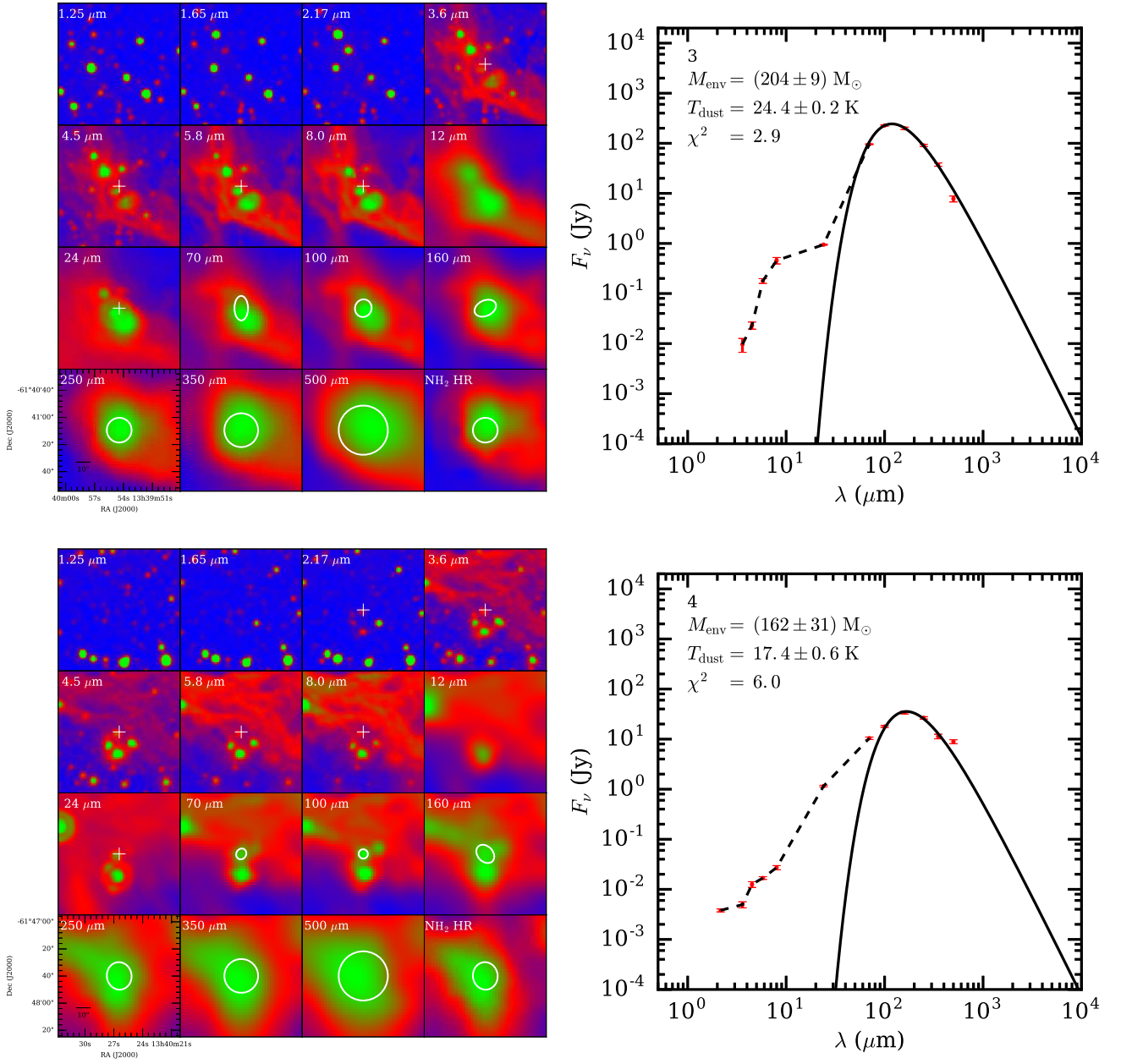


Fig. B.1: – continued.

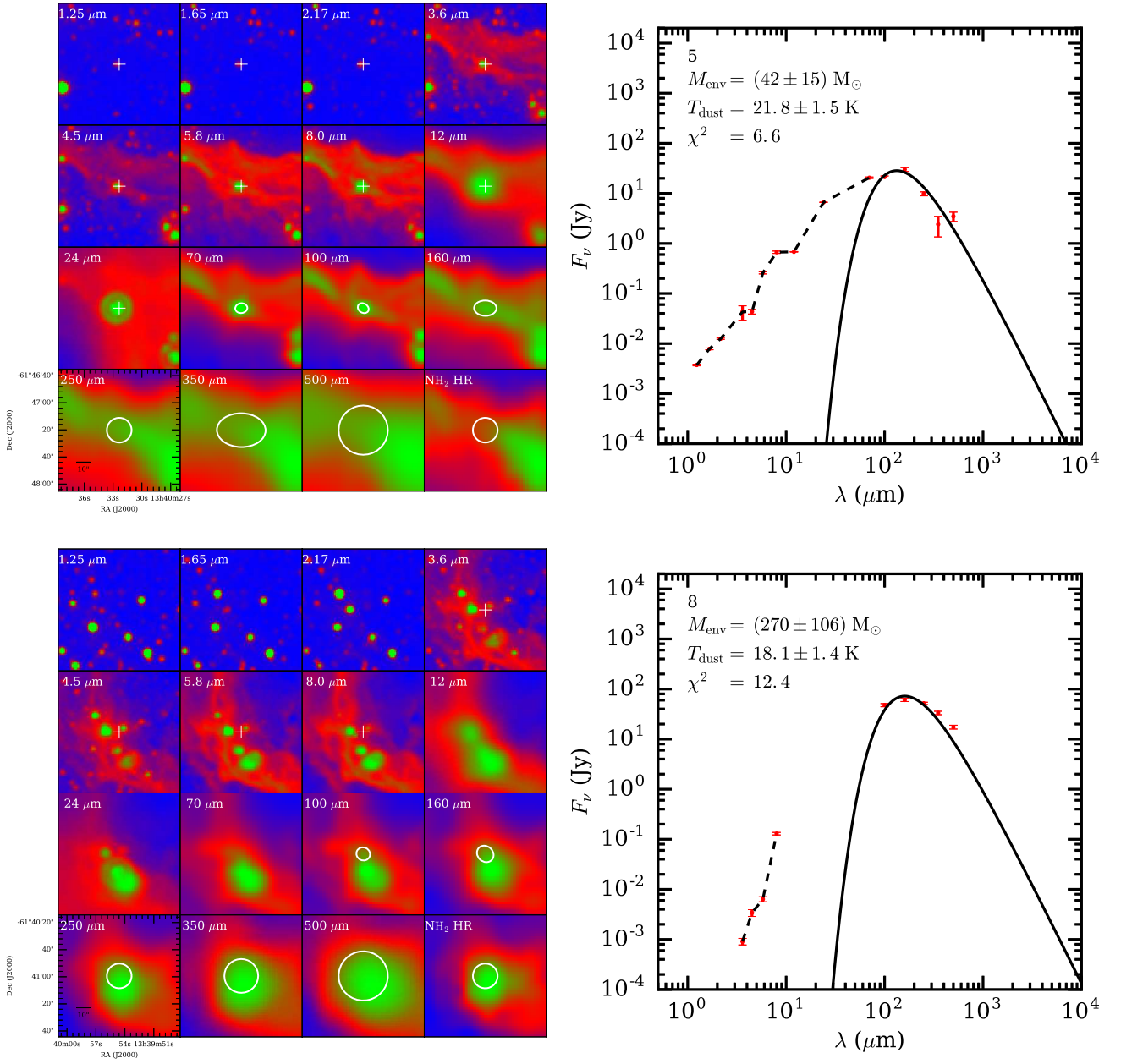


Fig. B.1: – continued.

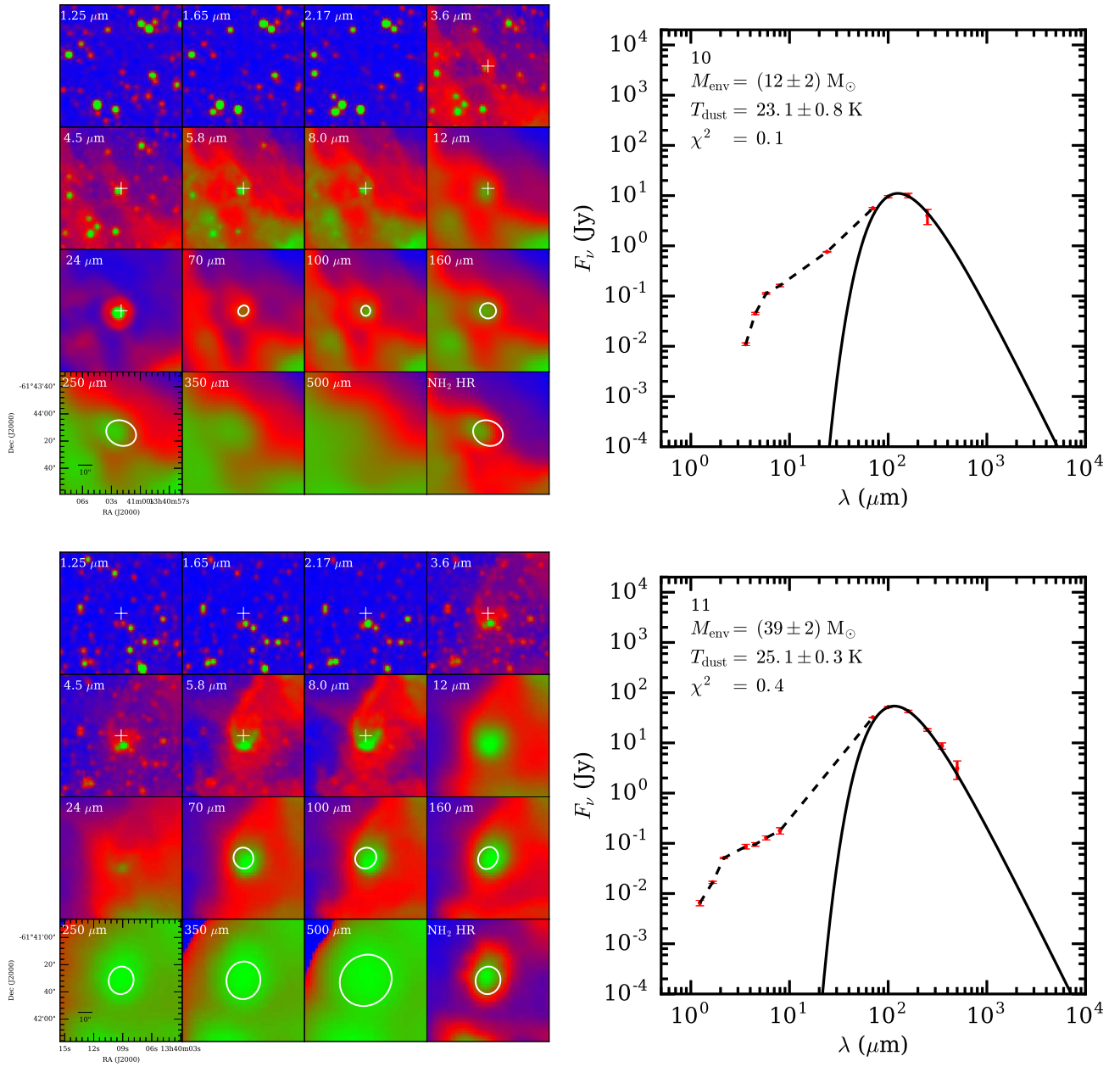


Fig. B.1: – continued.

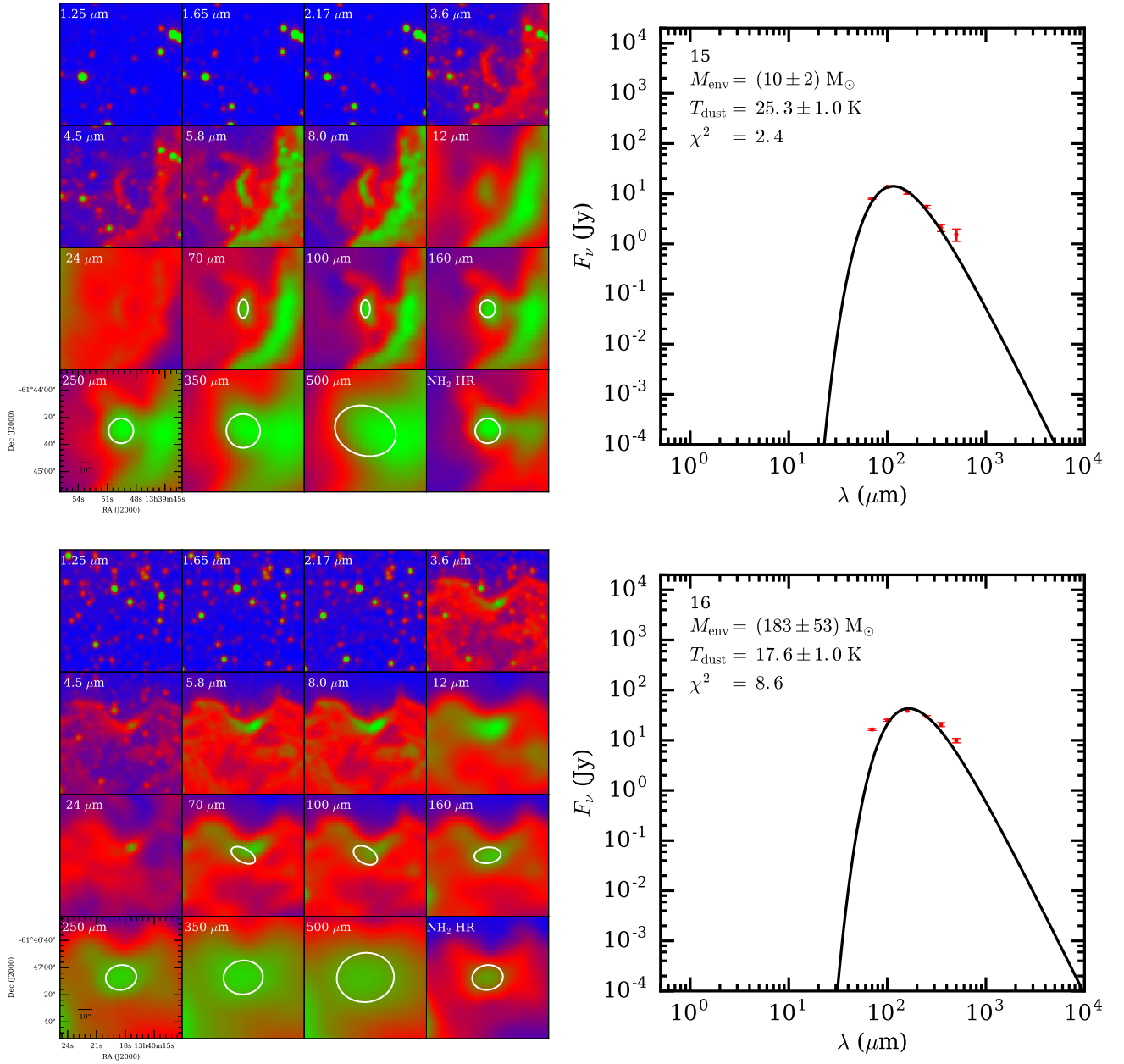


Fig. B.1: – continued.

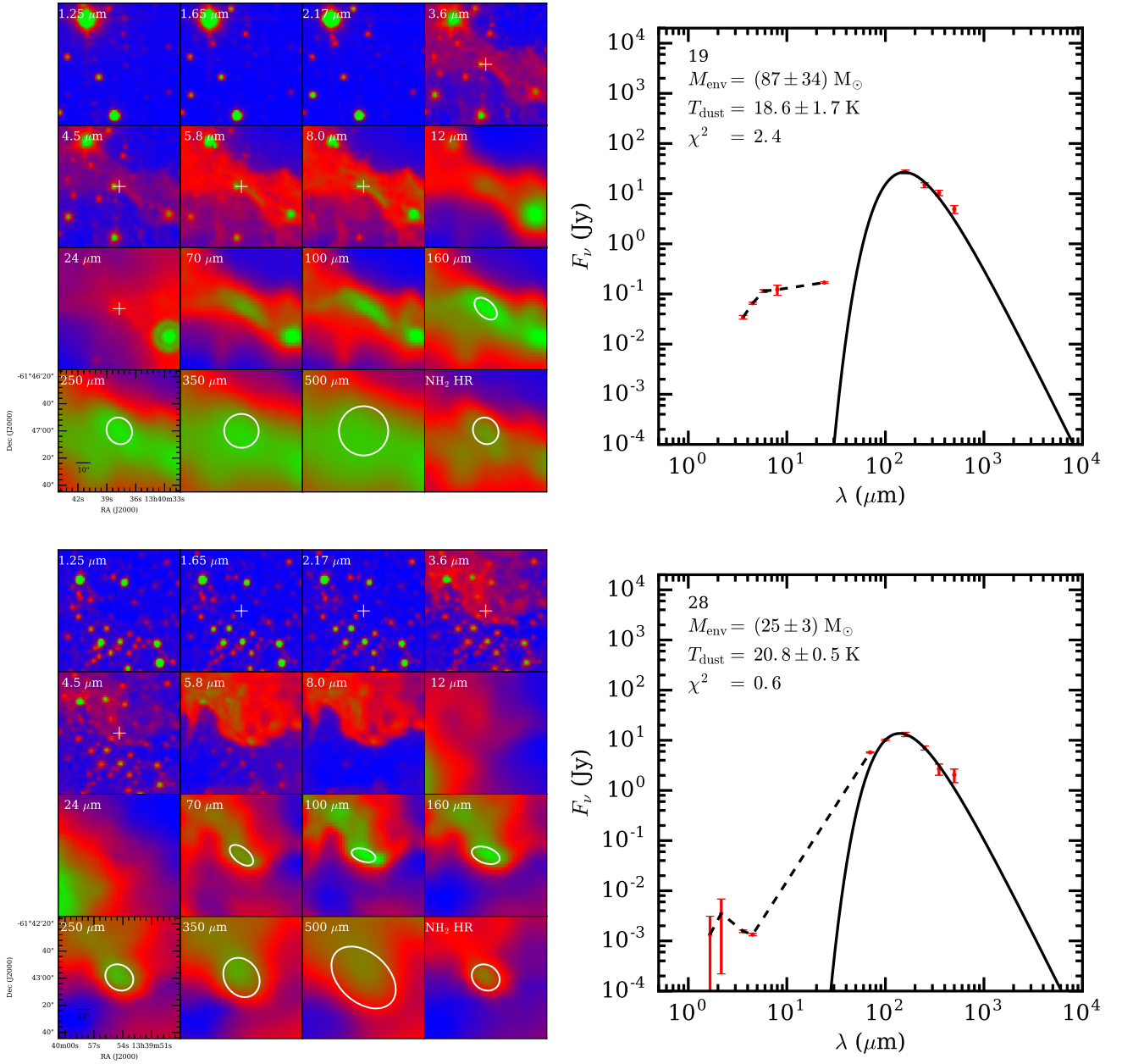


Fig. B.1: – continued.

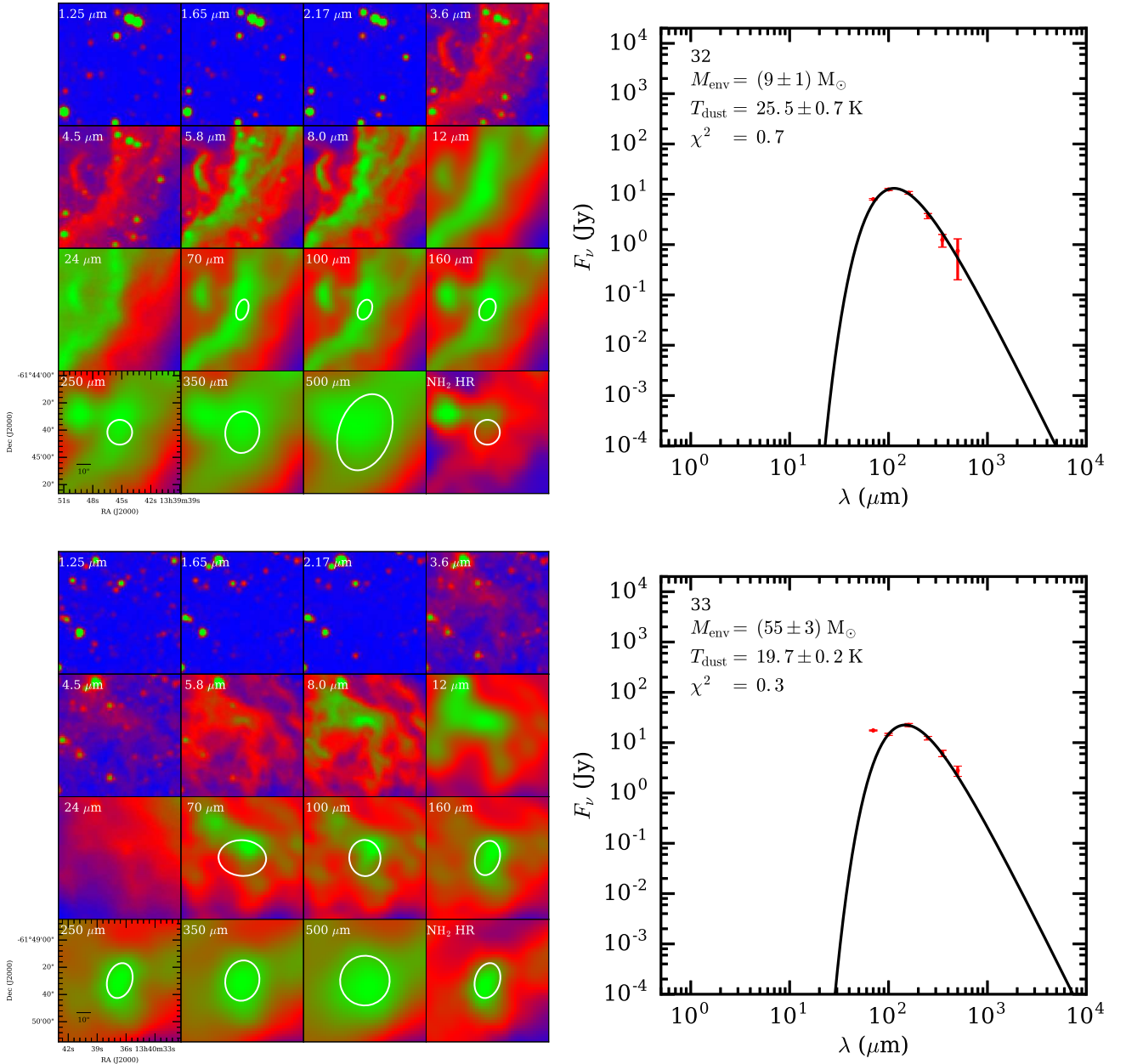


Fig. B.1: – continued.

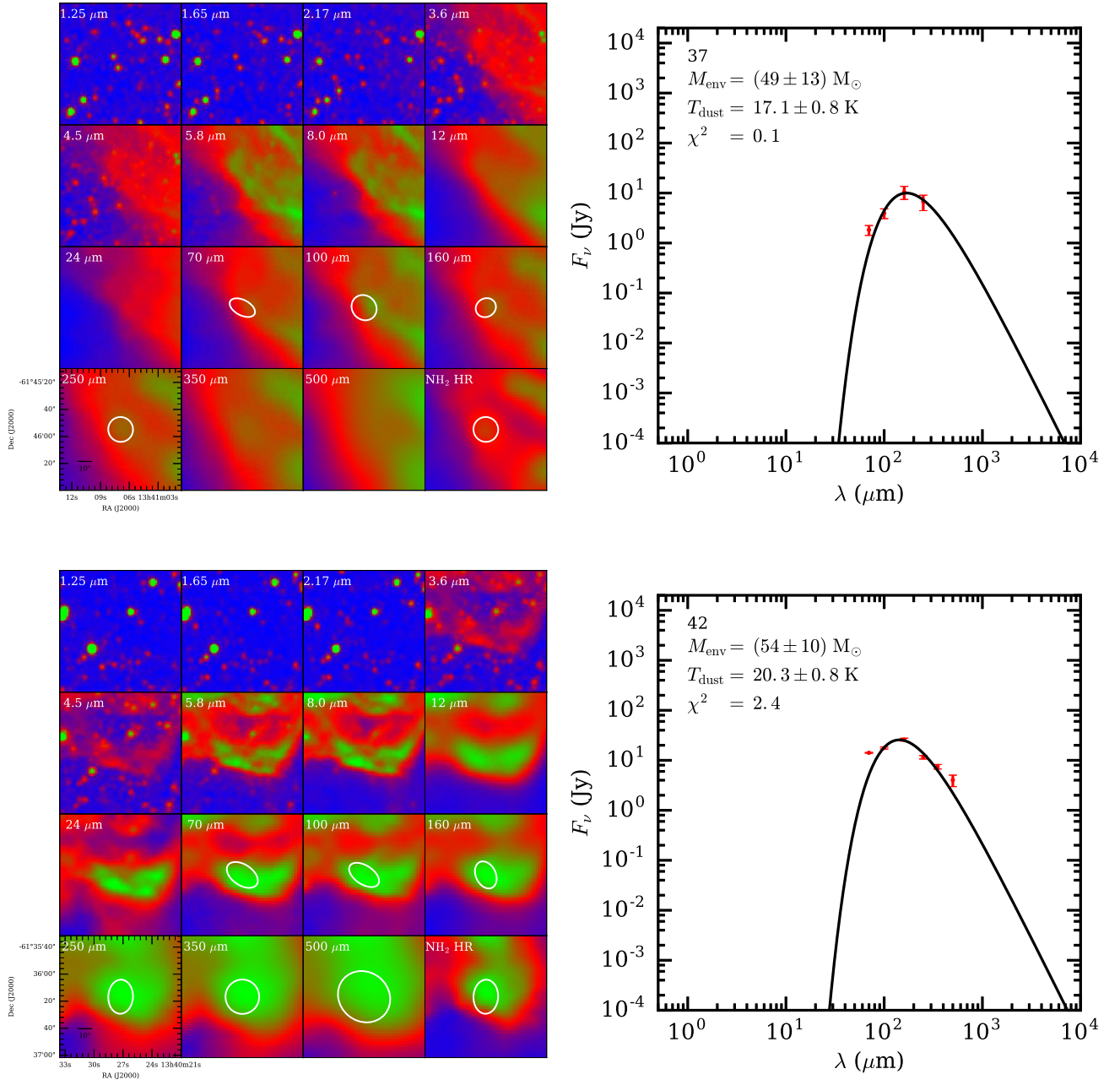


Fig. B.1: – continued.

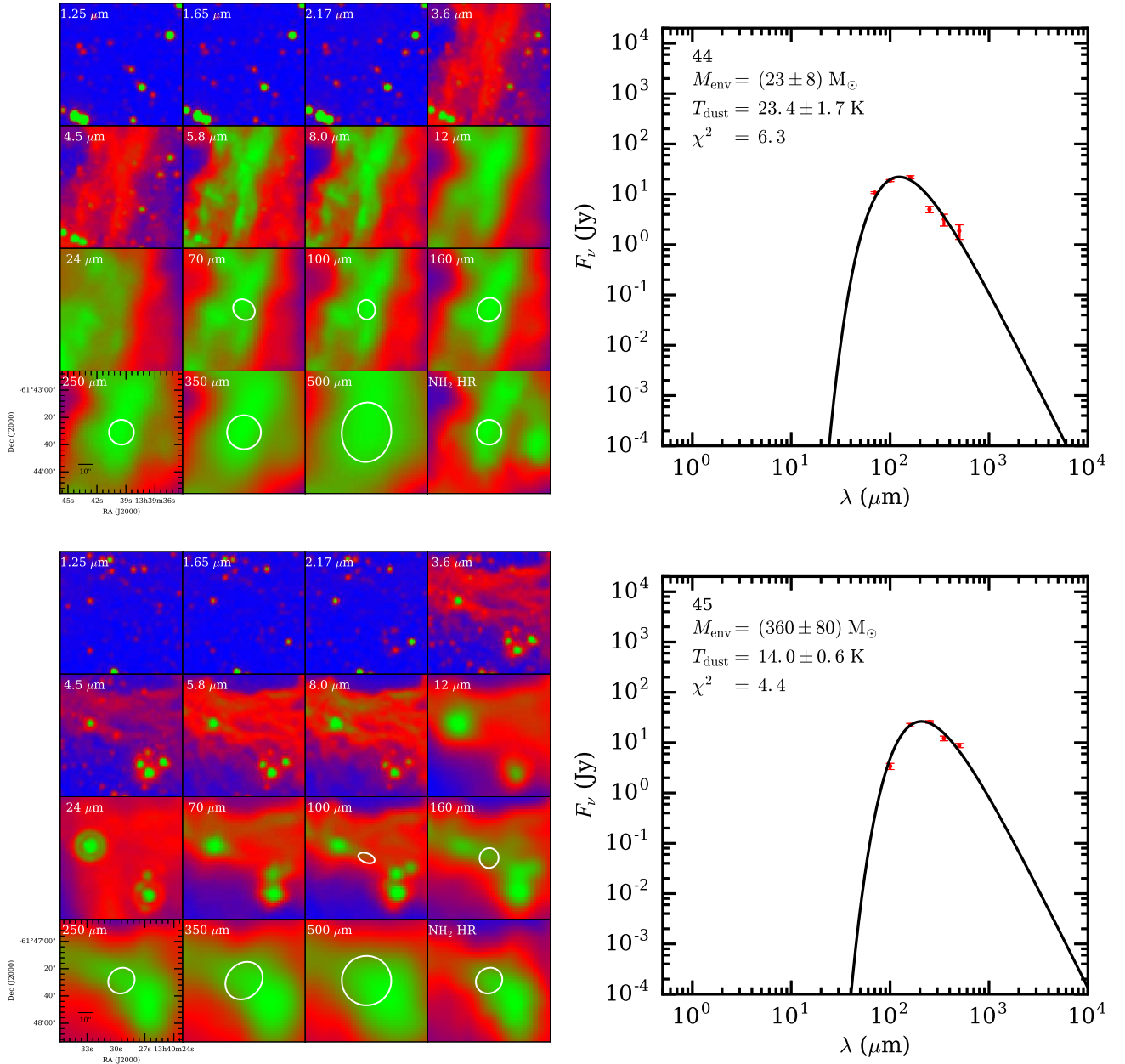


Fig. B.1: – continued.

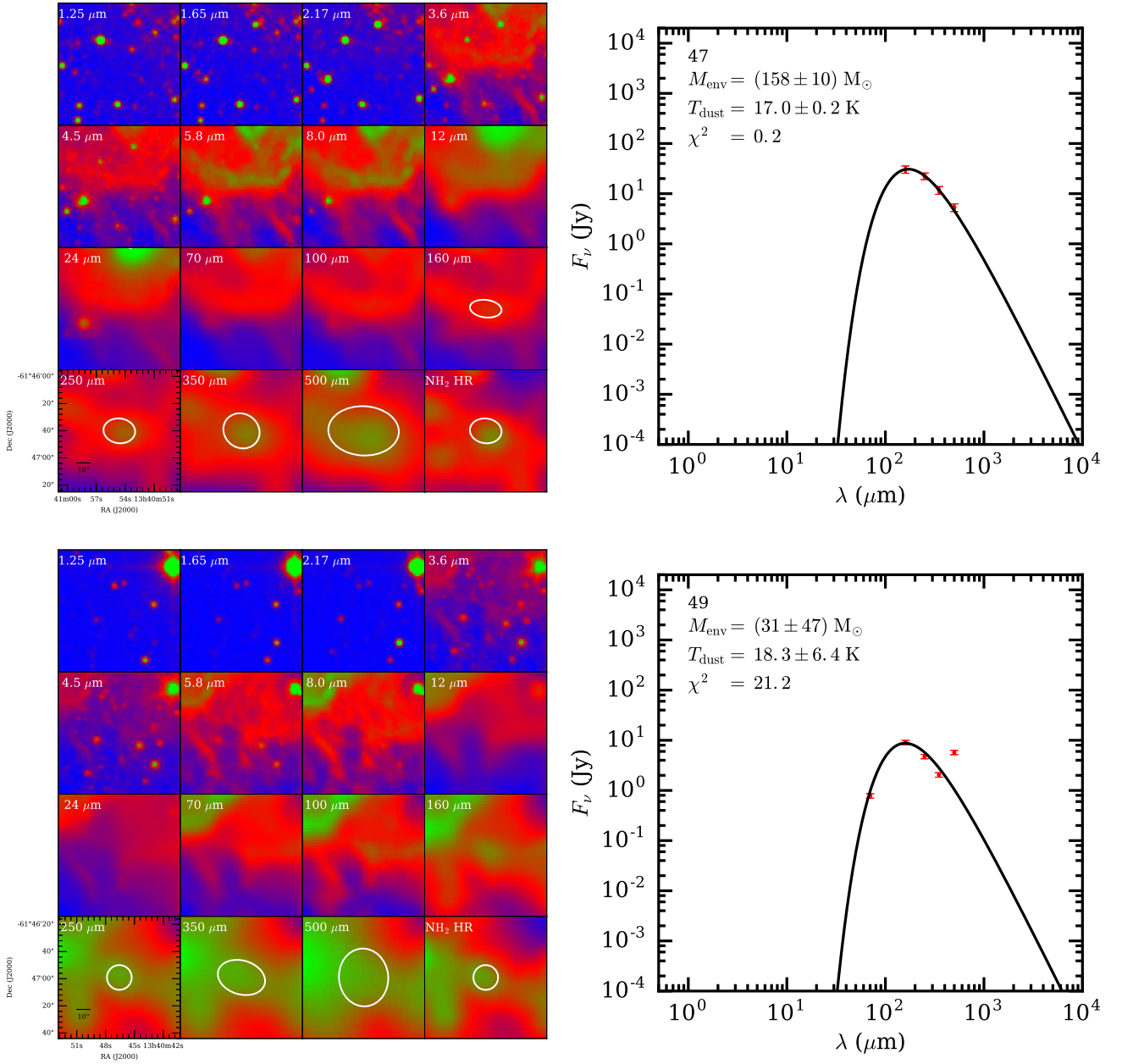


Fig. B.1: – continued.

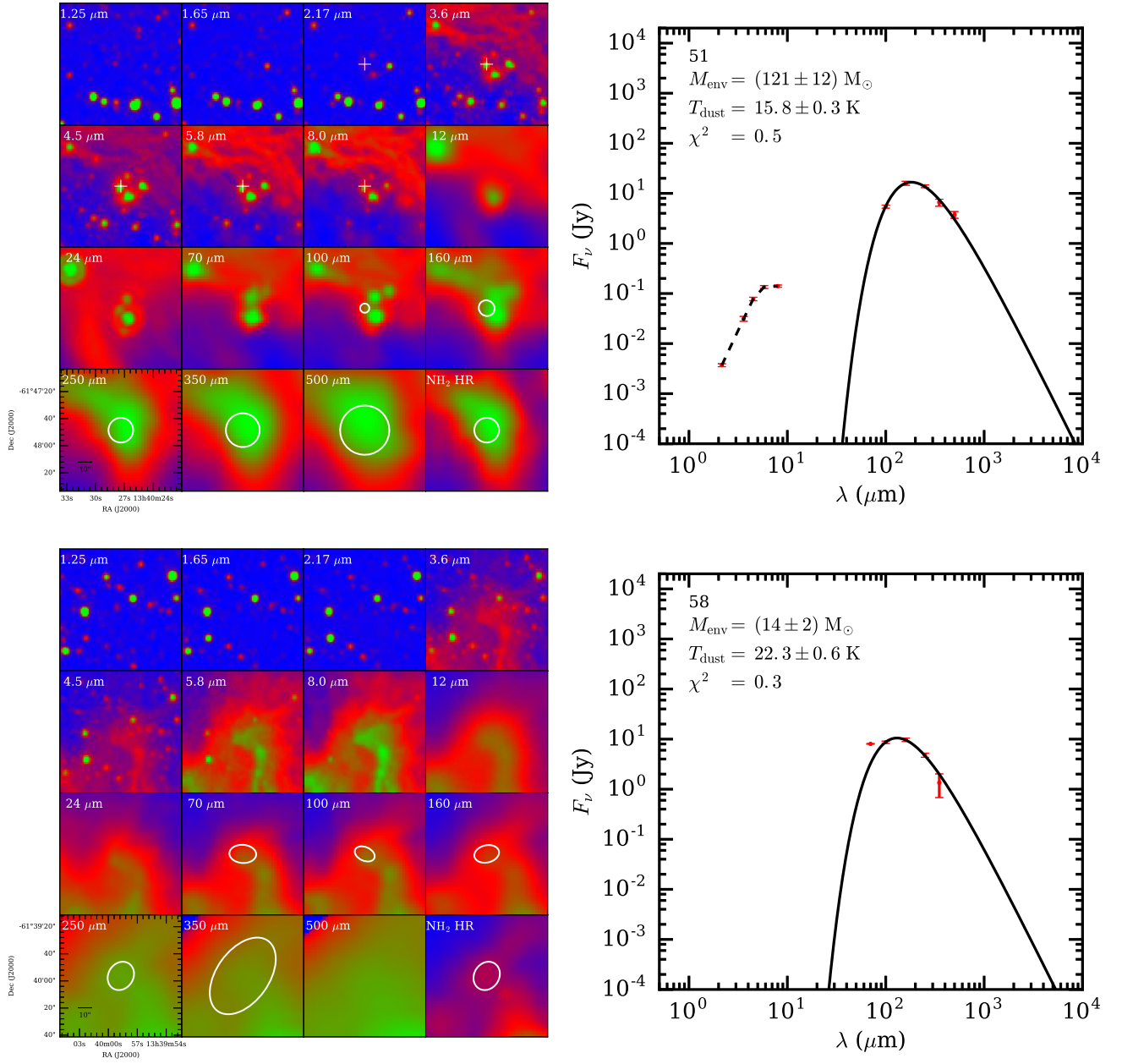


Fig. B.1: – continued.

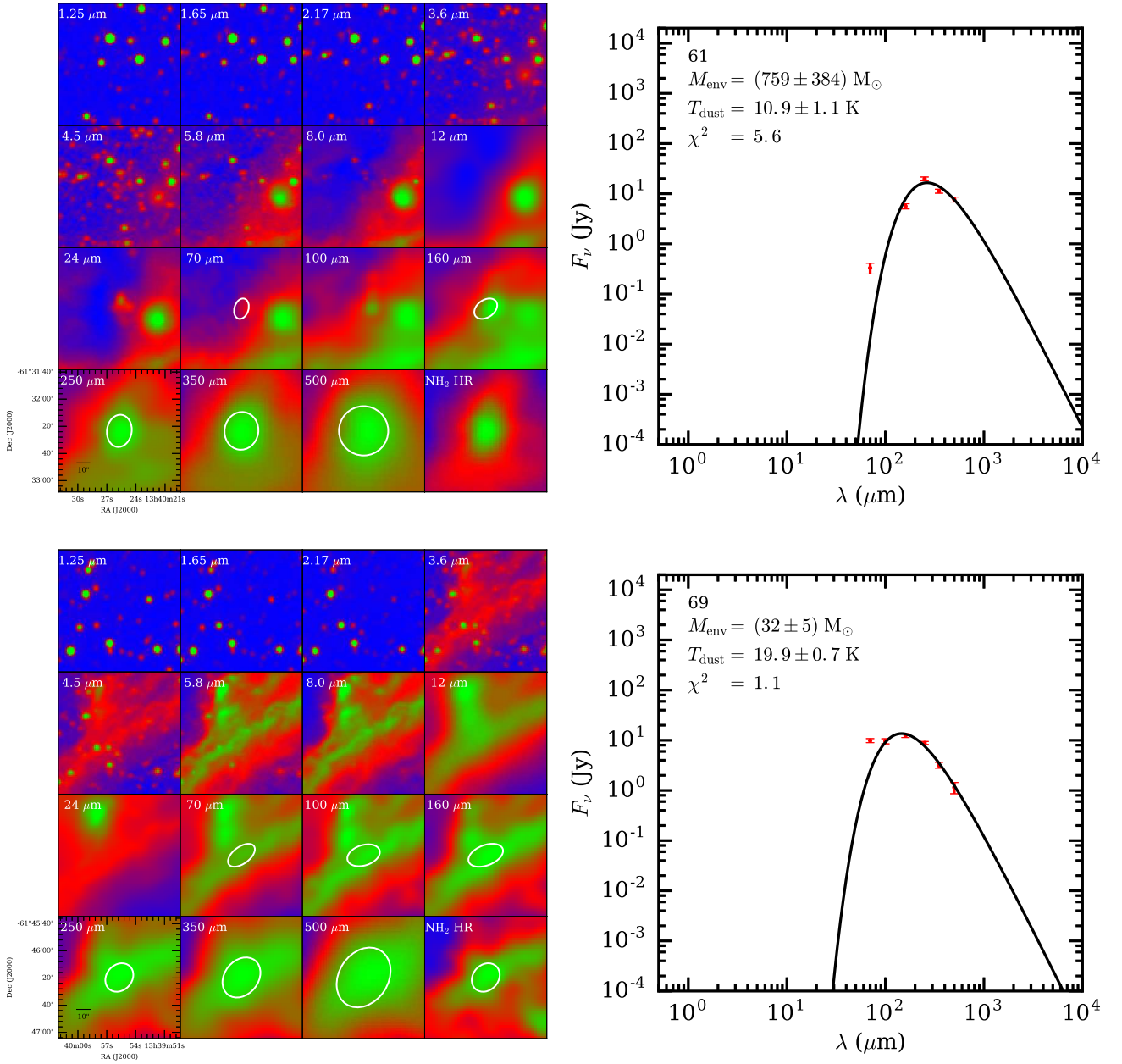


Fig. B.1: – continued.

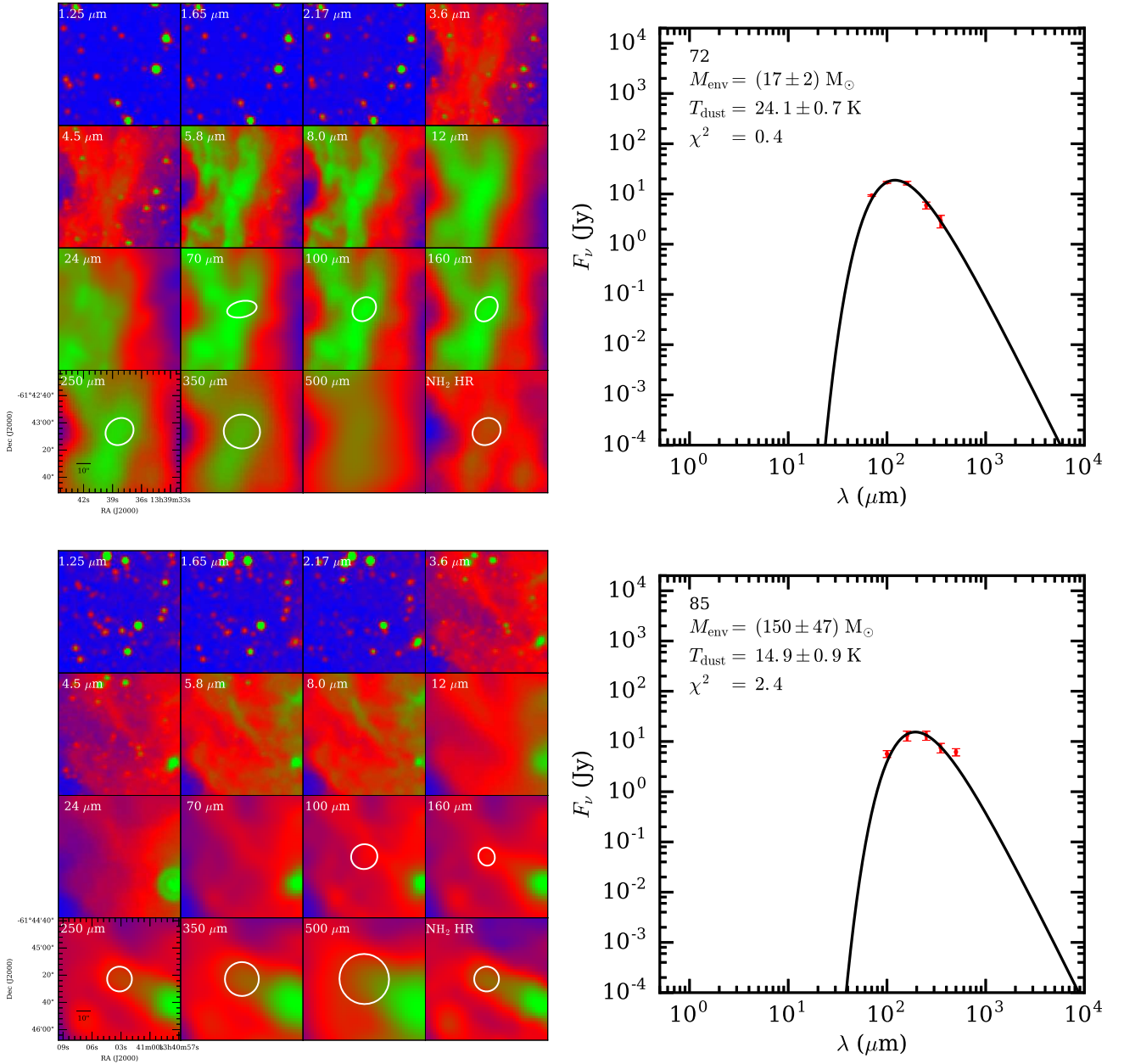


Fig. B.1: – continued.

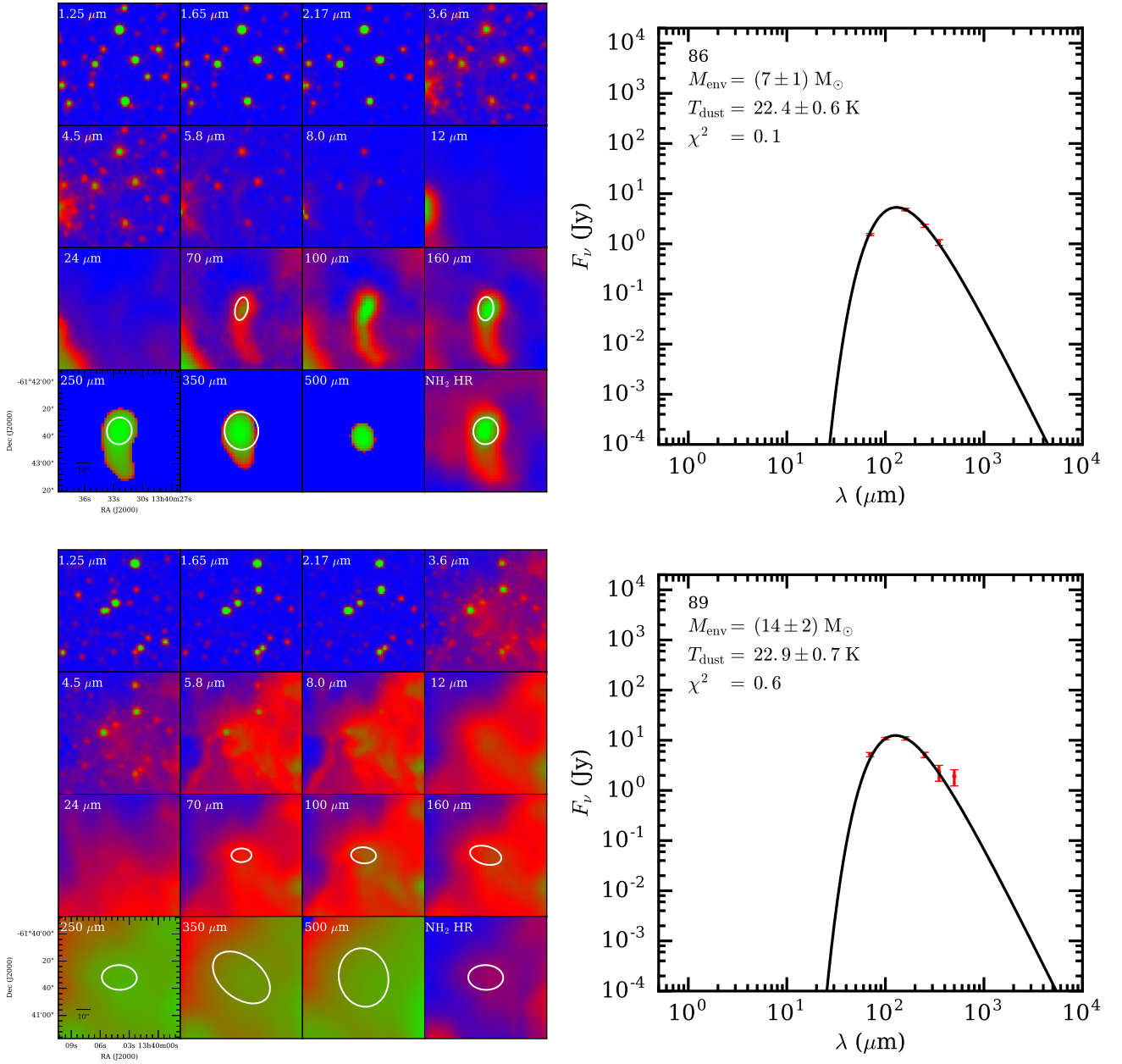


Fig. B.1: – continued.

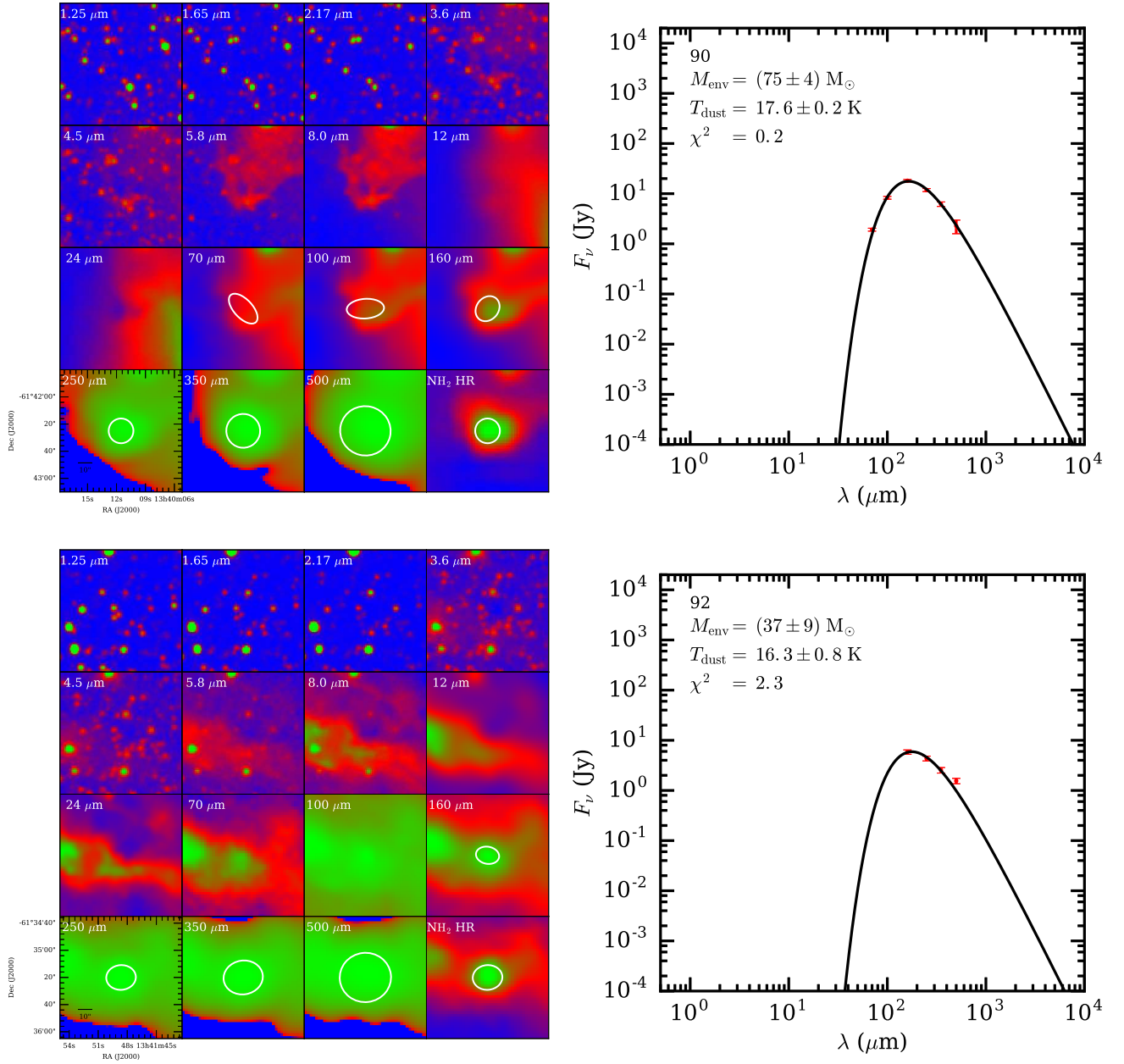


Fig. B.1: – continued.

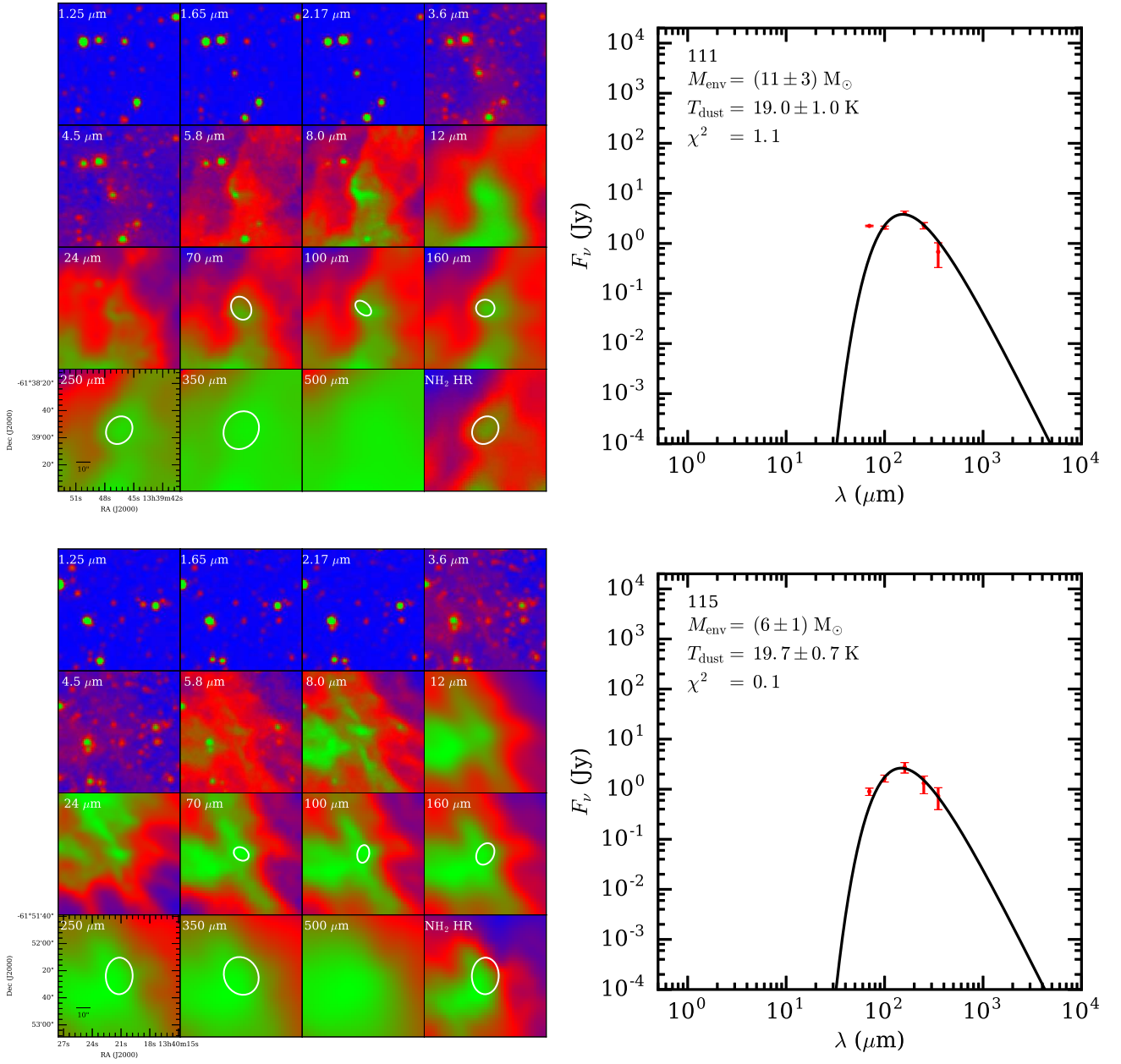


Fig. B.1: – continued.

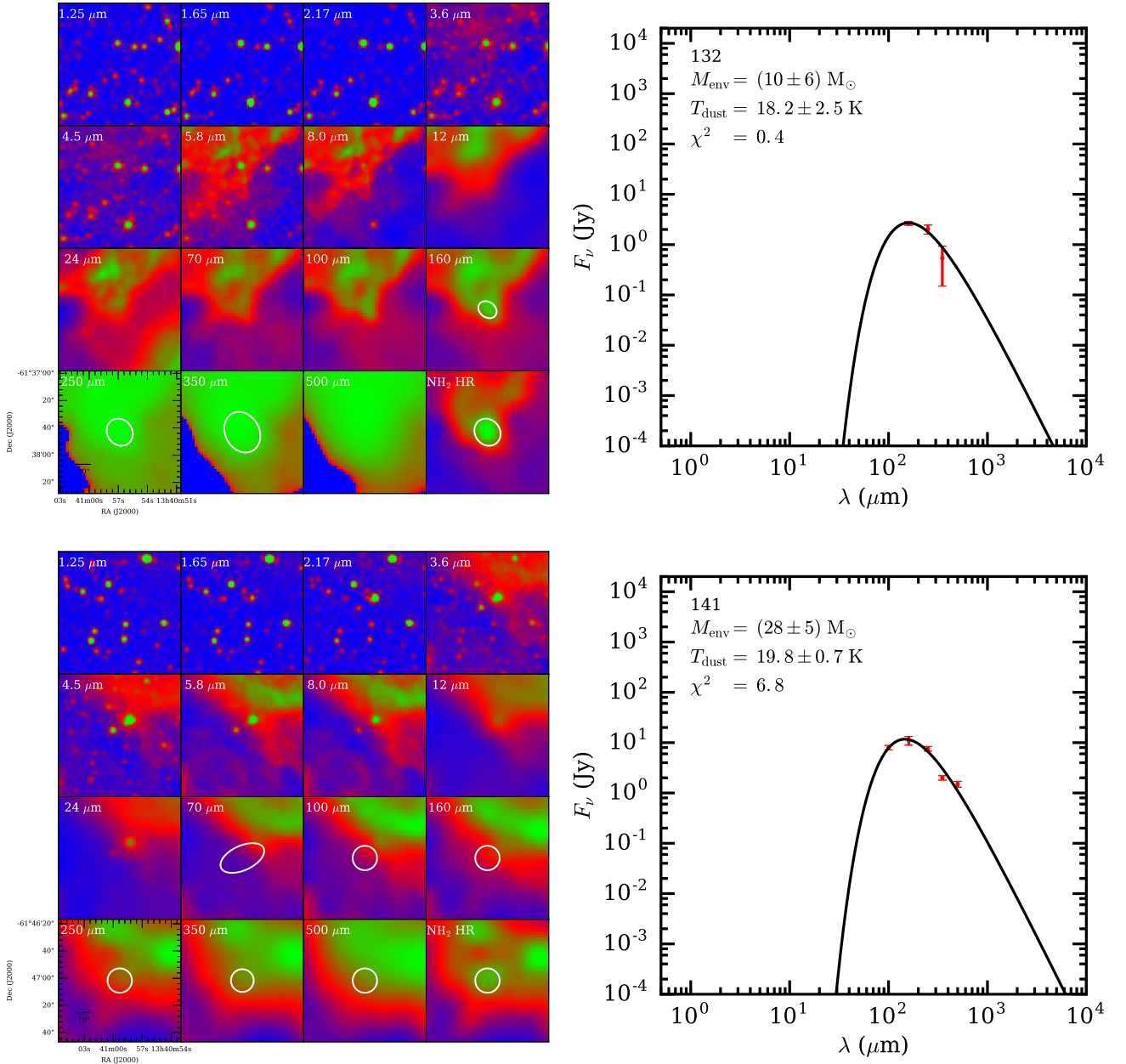


Fig. B.1: – continued.

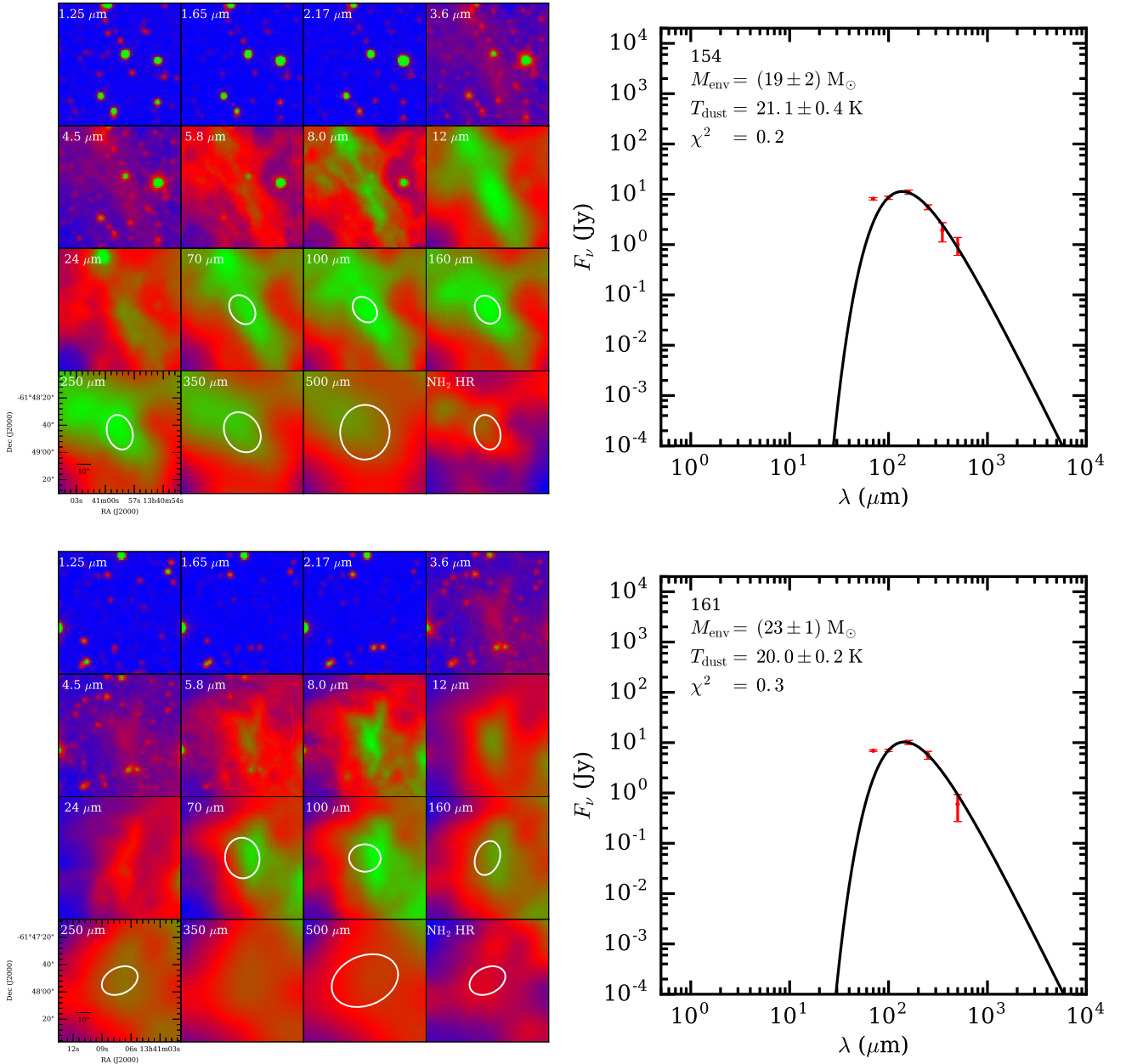


Fig. B.1: – continued.

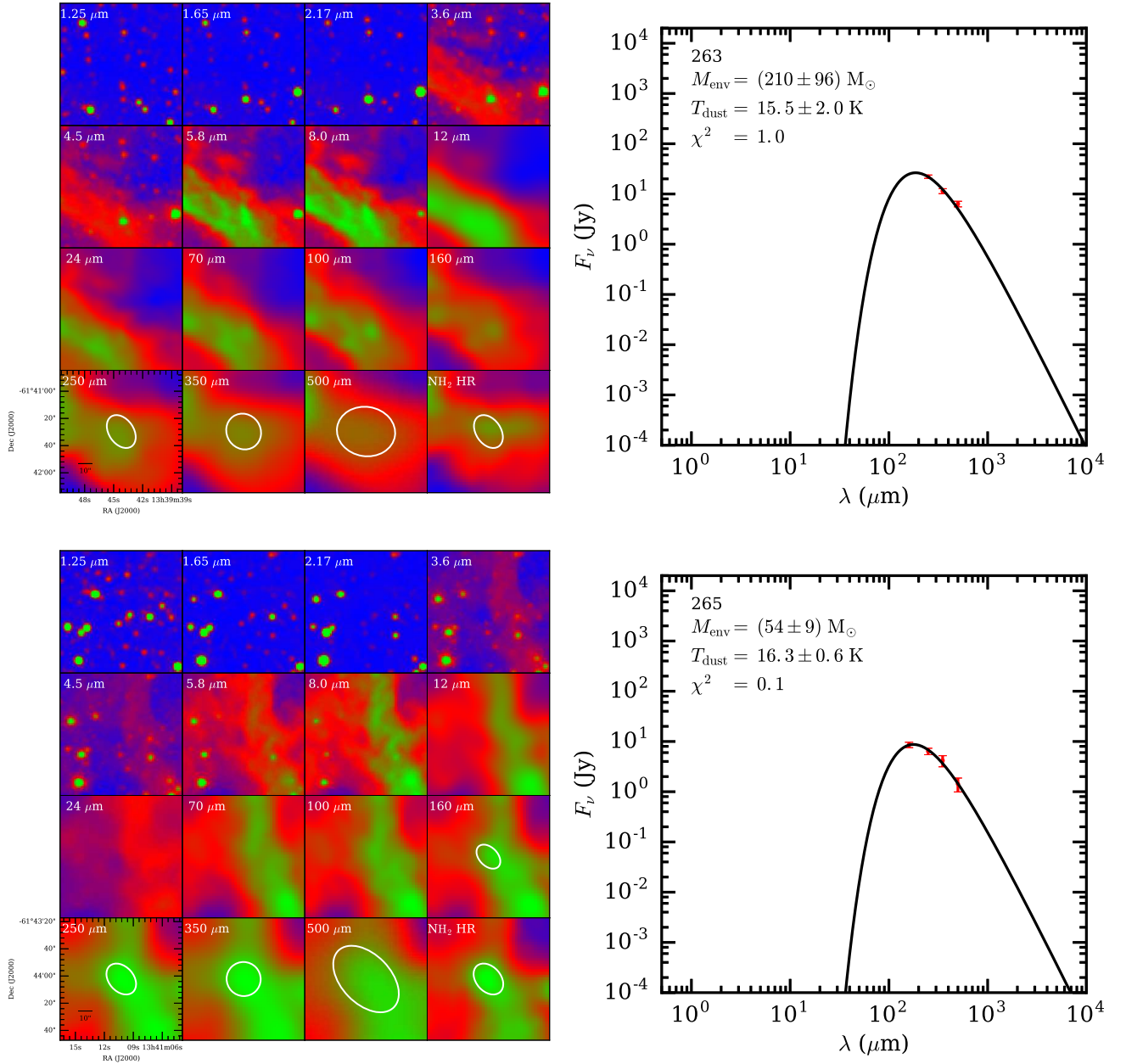


Fig. B.1: – continued.

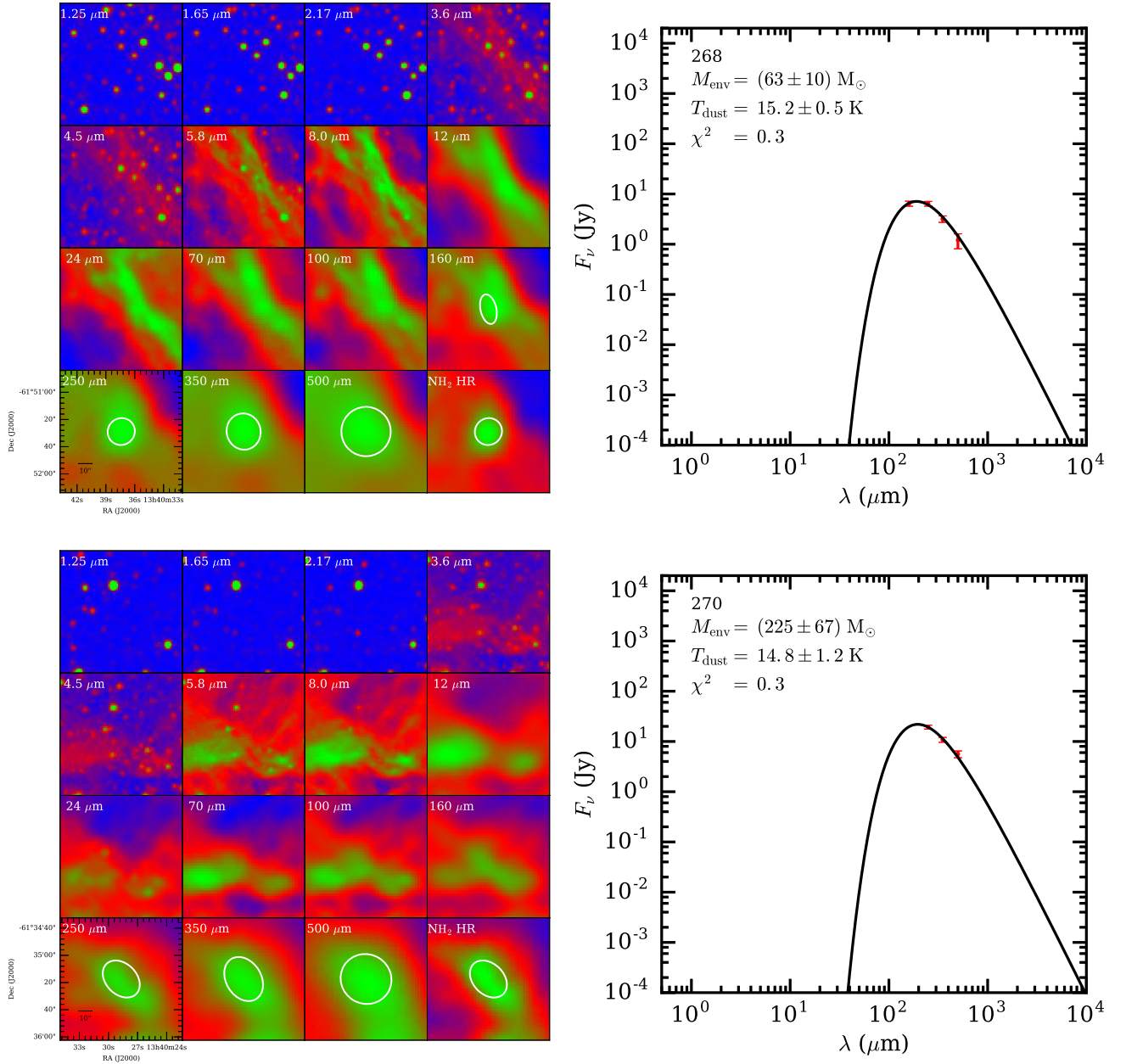


Fig. B.1: – continued.

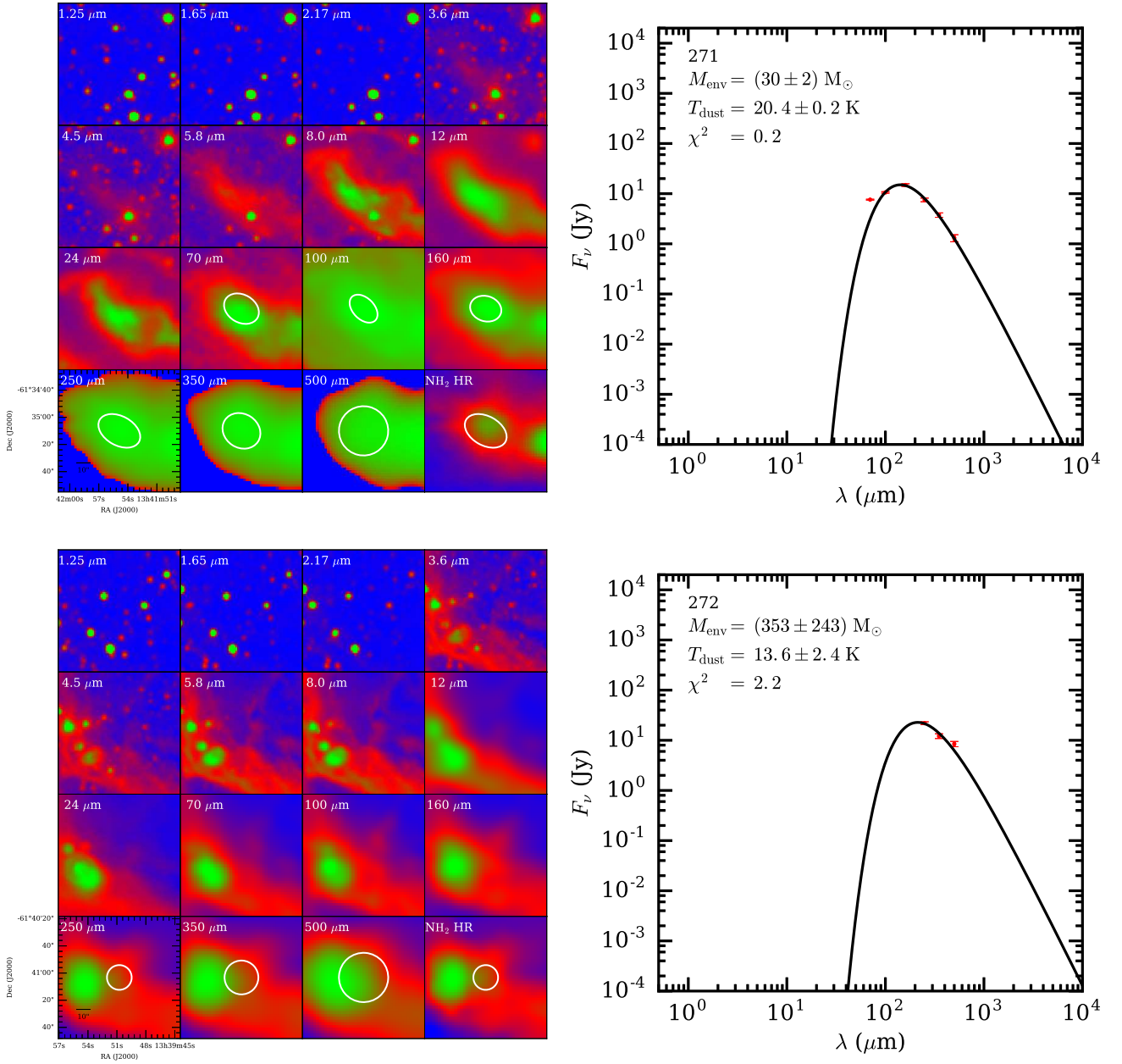


Fig. B.1: – continued.

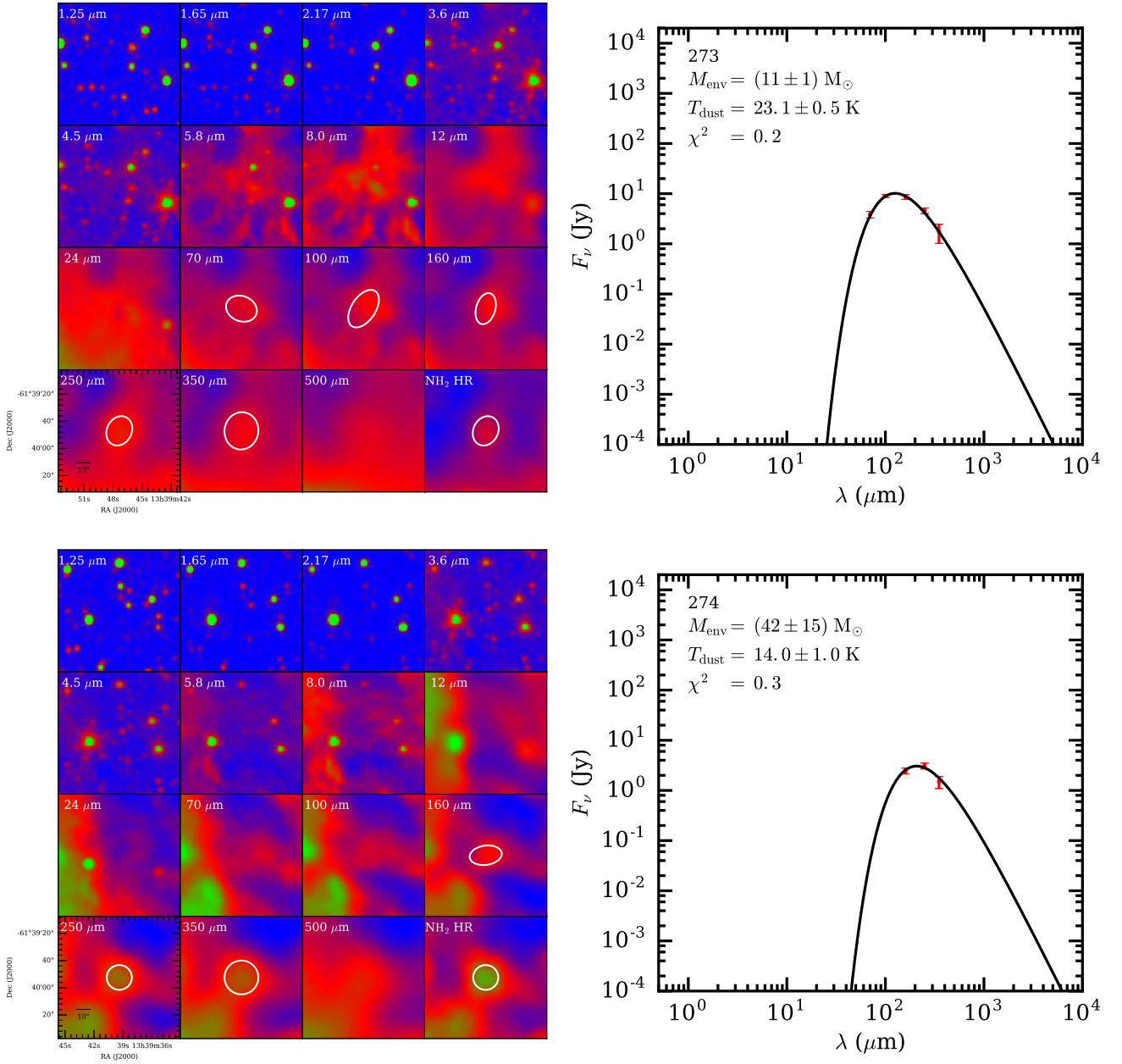


Fig. B.1: – continued.

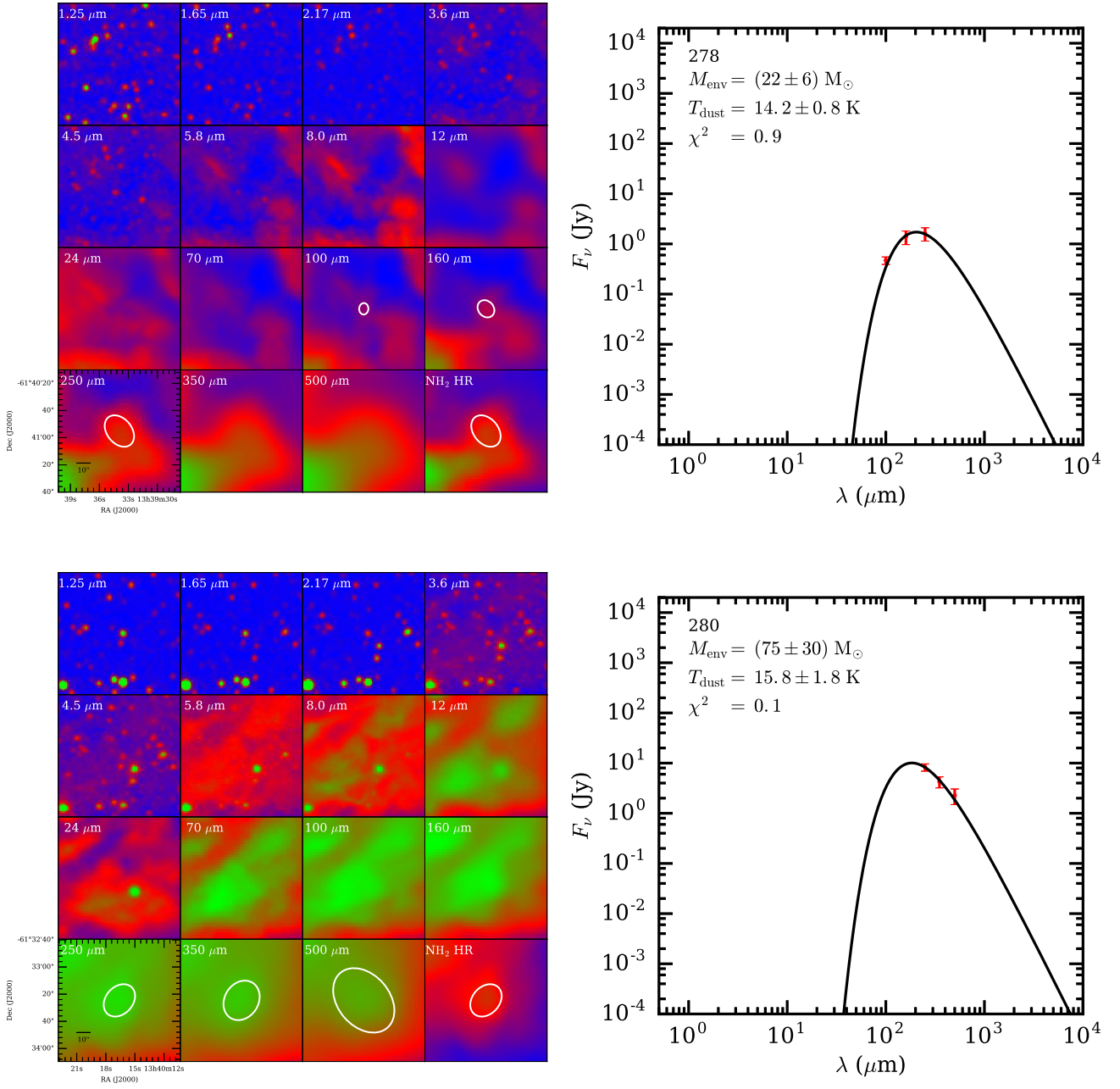


Fig. B.1: – continued.

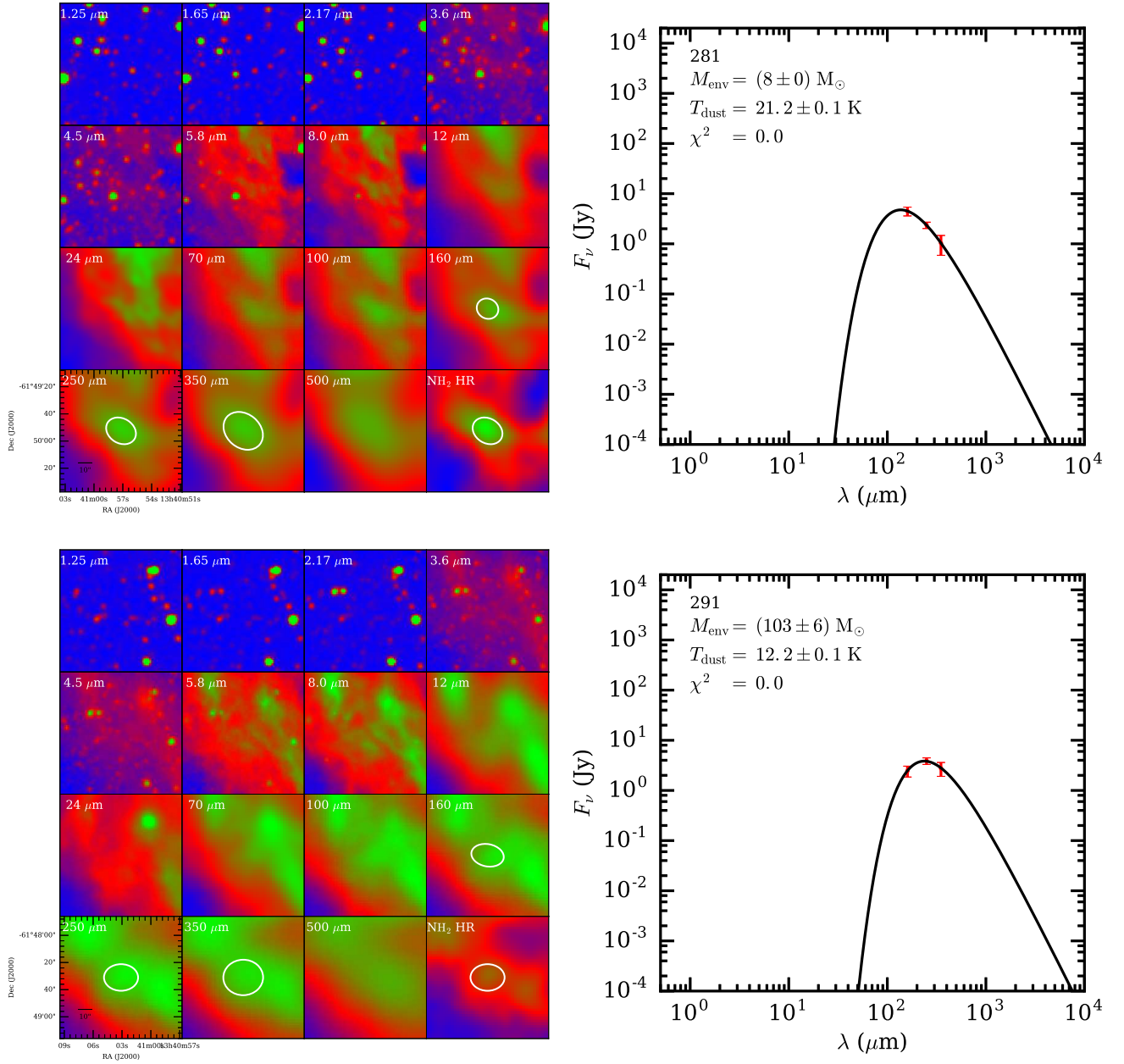


Fig. B.1: – continued.

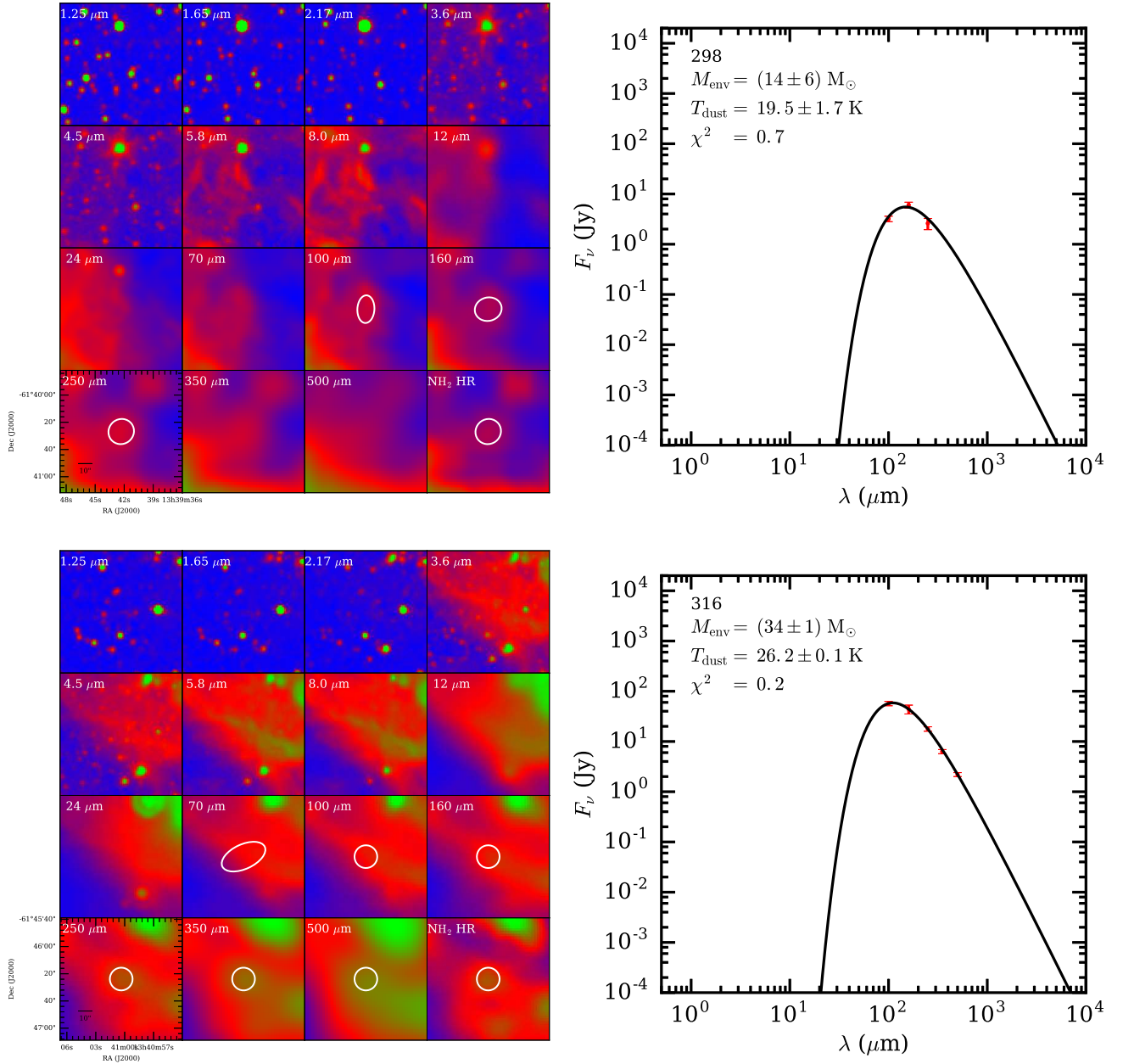


Fig. B.1: – continued.